Winter 12-15-2021

Laser stimulated dynamic thermal imaging system for tumor detection

Hongyu Meng
Washington University in St. Louis

Recommended Citation

Meng, Hongyu, "Laser stimulated dynamic thermal imaging system for tumor detection" (2021). *McKelvey School of Engineering Theses & Dissertations*. 729.
https://openscholarship.wustl.edu/eng_etds/729

WASHINGTON UNIVERSITY IN ST. LOUIS

School of Engineering & Applied Science
Department of Biomedical Engineering

Dissertation Examination Committee:
Samuel Achilefu, Chair
Adam Bauer
Abhinav Jha
Zohar Nussinov
Yuan-Chuan Tai

Laser Stimulated Dynamic Thermal Imaging System for Tumor Detection

by
Hongyu Meng

A dissertation presented to
the Graduate School
of Washington University in
partial fulfillment of the
requirements for the degree
of Doctor of Philosophy

December 2021
St. Louis, Missouri

Table of Contents

List of Figures

List of Tables

Acknowledgments

I would like to thank Dr. Samuel Achilefu, my research advisor. Dr. Achilefu is an excellent tutor and teacher. He is very nice and patient with students. He always works hard and has guided me a lot of knowledge about scientific research and study. Thank him for providing me with the opportunity to participate in this research, and also thank him for his patience with me in this process, as well as his support, guidance and encouragement.

I would like to thank the members of the Optical Radiology Laboratory, who helped me at in many ways. I would specially like to thank Dr. Christine M. O’Brien, Dr. Suman B. Mondal, Dr. Leonid Shmuylovich, Dr. Kalen Dionne, Gail P. Sudlow, Julie Prior, and Hanru Zhang, for their invaluable support, help, and scientific inputs. Especially Christine, Suman and Leo. Christine has given me a lot of help and guidance in the work of laser stimulated thermal imaging, this work could not be completed without her. Suman helped me get acquainted with the goggle project and guided my work. Leo can always put forward constructive opinions in every project and turn them into practice. Working with you is a precious experience in my life.

I would like to thank my collaborators outside the lab, Cheryl Bethea, Clyde Bethea, Kevin Bishop, Julia Carpenter, Praneeth Gogineni, and other collaborators. They laid the foundation for my work, provided supplements, and formed an indispensable part of the project.

Personally, I would like to thank my parents. They did everything they could for me, and have supported me for a long time. They had the greatest impact on my life, and their love for me made me who I am today.

Hongyu Meng

Washington University in St. Louis

December 2021

Dedicated to

Lingchun Meng, my father

Zailing Yu, my mother

ABSTRACT OF THE DISSERTATION

Laser Stimulated Dynamic Thermal Imaging System for Tumor Detection

by

Hongyu Meng

Doctor of Philosophy in Biomedical Engineering

Washington University in St. Louis, 2021

Professor Samuel Achilefu, Chair

Recent advances in infrared sensor technology have enabled the rapid application of thermal imaging in materials science, security and medicine. Relying on the infrared characteristics of living systems, thermal imaging has been used to generate individual heat maps, detect inflammation and tumor. As an imaging system, thermal imaging has the advantages of portability, real-time, non-invasive, and non-contact. But the low specificity of thermal imaging hinders its wide clinical application.

Unfortunately, label-free DTI is less able to fully capture thermal tissue heterogeneity in high resolution due partly to how thermal stimulation is applied. Current DTI methods apply thermal stimulation to a large area of tissue, which obscures the detection of the unique thermal characteristics of a small area in the thermally disturbed area. Super-resolution DTI grating can improve the spatial resolution, but the system setup is complex. For biological samples, the use of exogenous contrast agents can enhance contrast, but contrast agents increase regulatory hurdles in clinical trials.

In this work, we have developed a focused dynamic laser stimulation imaging (FDTI) system to overcome these limitations. The system, which has high resolution, high speed and large field of view uses a short wavelength laser to stimulate small tissue area and a thermal camera to acquire data. We captured thermal images and videos, extracted features, and built classifiers to distinguish tumors from normal tissues. Data analysis showed that FDTI method achieved high accuracy (classifier surpassed 90%) with spatial resolution attaining 1 mm, which surpasses conventional thermal imaging and DTI.

We next explored the ability of FDTI to detect early-stage tumors by scanning multiple areas that exhibited normal thermal images with conventional thermal imaging. A bioluminescence imaging (BLI) system was then used to locate the tumor, which was co-registered to the FDTI images to determine the position of the laser spot. By extracting features from the collected thermal images and videos and constructing the classifier, the FDTI system achieved an accuracy greater than 80% in detecting early tumors in different mouse tumor models.

Subsequently, the FDTI system was optimized to improve its acquisition speed, automation and robustness. First, we analyzed the influencing factors of imaging and proposed new system hardware designs to improve the data acquisition speed. Then, to shorten the acquisition time from the software level, we tested and analyzed the performance of features at different stages during the acquisition process. We also designed and tested registration markers, including registration results of different features, feature robustness under interference, marker detection from the background, and marker performance in motion correction to improve the degree of automation of the system. Furthermore, we tested the performance of thermal imaging applications in other research fields, including brain tumor detection, nerve damage assessment, and whether temperature changes correlate with stroke.

These results show that FDTI is a promising technique for enhancing contrast, improving spatial resolution, determining underlying tumor heterogeneity, and detecting tumors at stages when conventional thermal imaging is ineffective. This work lays a strong foundation for diverse applications and clinical translation of FDTI to address unmet needs of current thermal imaging technologies.

Chapter 1: Focal dynamic thermal imaging for label-free high-resolution characterization of materials and tissue heterogeneity

This chapter is based on a published article. Christine M. O'Brien, Hongyu Meng, Leonid Shmuylovich, Julia Carpenter, Praneeth Gogineni, Haini Zhang, Kevin Bishop, Suman B. Mondal, Gail P. Sudlow, Cheryl Bethea, Clyde Bethea & Samuel Achilefu. (2020). Focal dynamic thermal imaging for label-free high-resolution characterization of materials and tissue heterogeneity. Scientific reports, 10(1), 1-12. I helped in writing the manuscript in collaboration with the co-authors, participated in experimental design and execution, analyzed the data, made some illustrations and edited the manuscript.

1.1 Abstract

Evolution from static to dynamic label-free thermal imaging has improved bulk tissue characterization, but fails to capture subtle thermal properties in heterogeneous systems. Here, we report a label-free, high speed, and high-resolution platform technology, focal dynamic thermal imaging (FDTI), for delineating material patterns and tissue heterogeneity. Stimulation of focal regions of thermally responsive systems with a narrow beam, low power, and low cost 405 nm laser perturbs the thermal equilibrium. Capturing the dynamic response of 3D printed phantoms, ex vivo biological tissue, and in vivo mouse and rat models of cancer with a thermal camera reveals finite structures of materials and delineates diseased from healthy tissue. The intuitive and non-contact FDTI method allows for rapid interrogation of suspicious lesions and longitudinal changes in tissue heterogeneity with high-resolution and large field of view. Portable FDTI holds promise as a clinical tool for capturing subtle differences in heterogeneity between malignant, benign, and inflamed tissue.

1.2 Introduction

Applications of thermal imaging in materials science, security, and medicine have surged in recent years, due in part to advances in infrared sensor technology [1-3]. Relying on the emissive properties of living systems, thermal imaging has been used to generate heat maps of individuals and detect inflammation. Despite its advantages of being a handheld, real-time, and non-contact measurement technique, the poor specificity of thermal imaging has prevented widespread adoption in the clinic [4]. To overcome this limitation, techniques that probe thermal tissue properties, rather than equilibrium temperature, have been developed. These dynamic thermal imaging (DTI) techniques apply a hot or cold thermal stimulus to tissue and observe its rate of recovery. Leveraging the different rates of thermal recovery in healthy versus diseased tissue following the application of thermal stimulus [5], DTI has demonstrated improved tumor detection accuracy [5-8]. However, label-free DTI fails to fully capture high-resolution thermal tissue heterogeneity, which can highlight subtle differences for distinguishing malignant, benign, or inflamed tissue [9, 10]. This resolution limit is due to how a thermal stimulus is applied. In existing implementations of DTI, a thermal stimulus is applied over a large area of tissue, which blurs the detection of unique thermal properties of small areas within the thermally perturbed region. Super-resolution DTI rasters focal excitation of visible light across the sample, followed by image reconstruction that determines the centroid of absorptive agents well beyond the diffraction limit to improve spatial resolution[11]. For biological samples, exogenous contrast agents such as dyes or nanoparticles are used to generate sufficient contrast. While this technique is an exciting advancement for microscopy applications, in vivo or point-of-care applications would be complicated by long imaging time (minutes rather than seconds), complex system setup, and reliance upon exogenous contrast agents. While exogenous agents are particularly useful in an ex-vivo setting, for in-vivo applications, they add regulatory hurdles for product approval that may limit their clinical applicability. As such, a gap exists between low-resolution but high field of view wide-field DTI that has seen multiple in vivo applications, and super-resolution DTI, which holds great promise ex vivo.

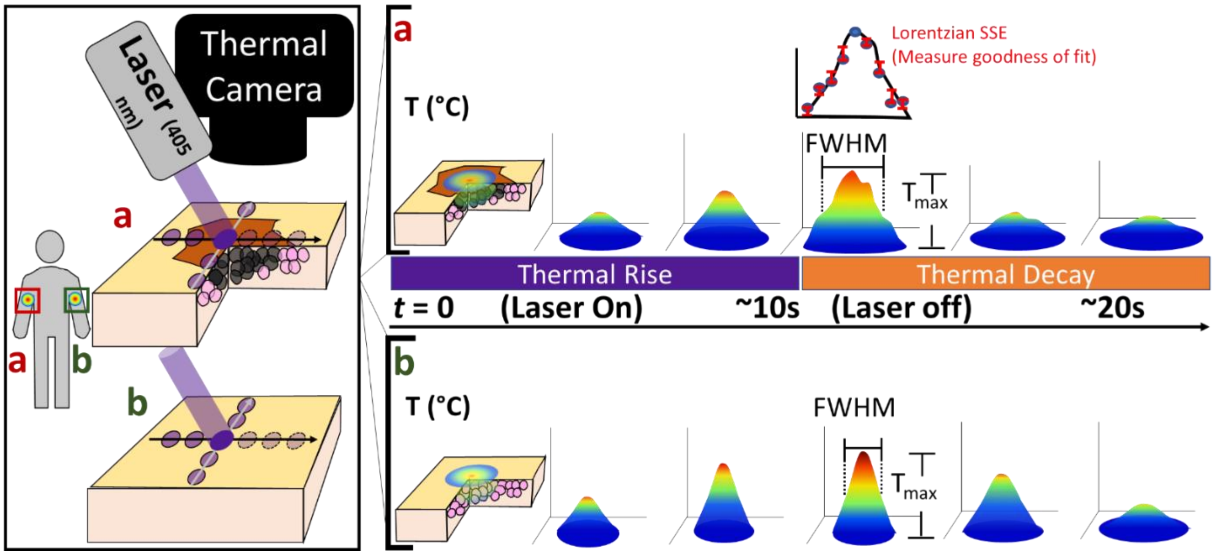

Figure 1. 1 FDTI of one rat throughout tumor progression. Thermal image (left) and corresponding FWHM from FDTI analysis (left center) on tumor. Thermal image (right center) and corresponding FWHM from FDTI analysis (right) from normal tissue over time

Here, we report the development of a new label-free dynamic photothermal imaging technique, focal dynamic thermal imaging (FDTI), which overcomes the spatial limitations of current DTI strategies while using simple hardware and analysis methods compared to super resolution DTI. Abundance of light-absorbing chromophores creates heat upon exposure to radiation. Leveraging this phenomenon, we postulated that the skin would efficiently absorb a narrow beam 405 nm light to generate a focal thermal source that propagates radially from the heat source through the tissue along a temperature gradient. The use of focused 405 nm light allows for thermal contrast generation through endogenous chromophores rather than exogenous dyes. However, care must be taken to ensure laser irradiation does exceed doses where that may be associated with DNA damage[12]. A thermal camera detects the ensuing perturbation and recovery of the thermal equilibrium. While tissue-specific optical properties define the degree and distribution of light absorption and subsequent heat generation, tissue properties such as thermal conductivity, specific heat, density, perfusion, metabolic rate, and the baseline temperature dictate heat propagation (Figure 1. 1). Assessment of this new technique using custom 3D printed thermal resolution targets showed higher spatial resolution and contrast than conventional DTI. In vivo, FDTI was able to distinguish healthy and cancerous tissue in animal models of cancer with over 90% accuracy. The label-free, non-contact, intuitive, and portable FDTI system provides high-resolution and high contrast images in real-time for use in diverse applications, including materials characterization and disease diagnosis.

1.3 Results

1.3.1 Computational modeling

A 3D model of the FDTI phenomenon was developed in COMSOL to demonstrate the feasibility of using this technique to measure unique signals from different materials and tissue types. The impact of each variable specified in the Pennes' bioheat equation[13] on heat generation and transfer was evaluated using a parameter sweep across high and low biological values. The simulations were analyzed by plotting cross-sections of the thermal peak along the diameter of the laser spot and extracting the amplitude and full width at half maximum (FWHM).

Simulations depicted in Figure 1. 2 **错误!未找到引用源。**a illustrate the expected radial heat propagation away from the initial thermal source initiated by light absorption. As expected, the parameter sweep of thermal and optical properties show that thermal conductivity and optical absorption coefficient greatly affect the resulting FDTI signals (Figure 1. 2 b,c).

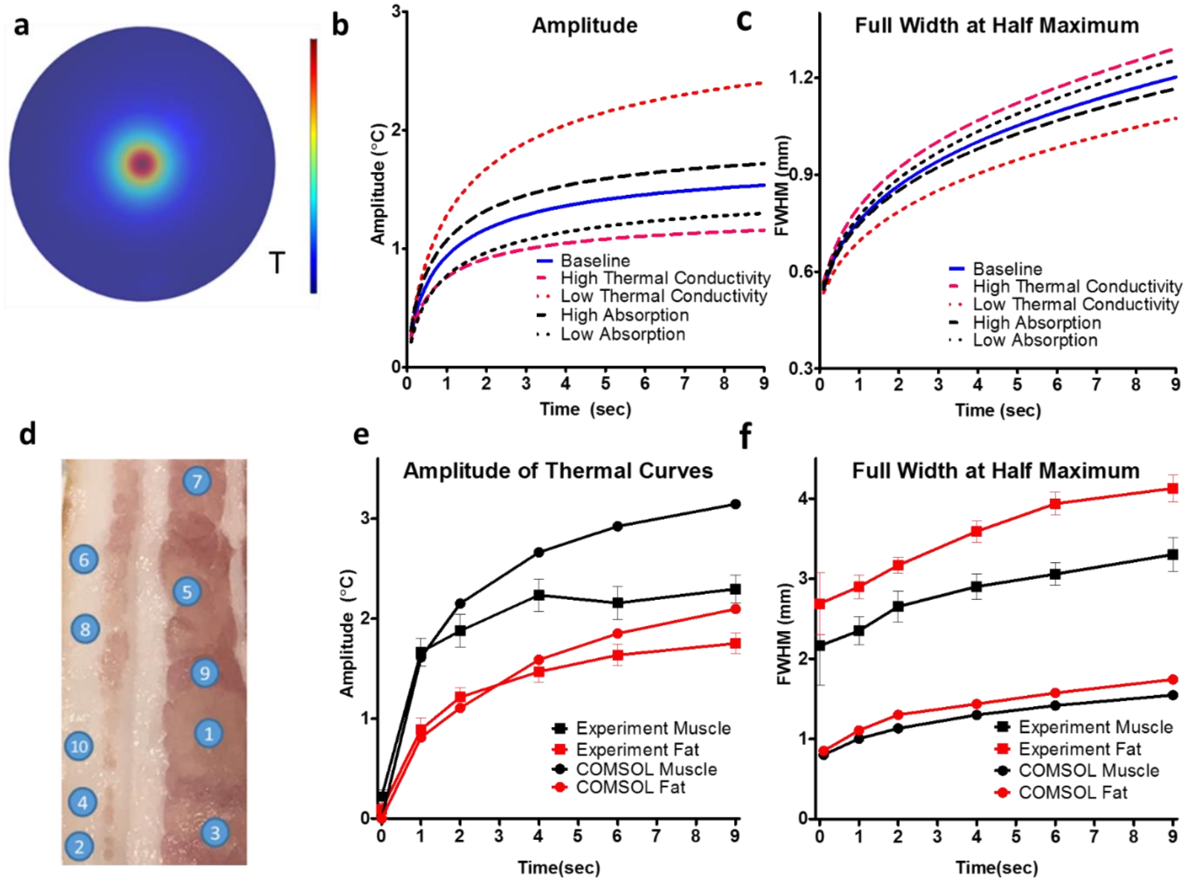

Figure 1. 2 FDTI simulation and validation. a) COMSOL simulation demonstrating radial heating from laser stimulation during the heat rise phase of FDTI; b) amplitude and c) FWHM results from simulated parameter sweep; d) porcine tissue measured for experimental validation of COMSOL model; e) amplitude and f) FHWM comparison between simulated and experimentally measured values of porcine muscle and fat tissue

The model was validated experimentally using porcine tissue with well-differentiated muscle and fat compartments (Figure 1. 2 d-f) using the same laser power and irradiation duration in the model. The FWHM and amplitude of the thermal peak revealed similar trends in the experiment and COMSOL simulation results, verifying that the trends observed in the parameter sweep reflect results from biological experiments. The COMSOL model provides a numerical basis for using FDTI to detect distinct thermal characteristics in different tissue types.

1.3.2 Data acquisition and analysis

FDTI data were acquired with a thermal camera. The images can be visualized as 3D plots with spatial location in x and y, and temperature in z at a fixed time t. Prior to laser stimulation, the 3D plot is essentially flat and reflects steady state skin temperature. A thermal peak grows exponentially with time in the area of laser stimulation. After turning off the laser, the heat decays exponentially as a function of tissue thermal properties. Common features extracted from FDTI, either from single frames or throughout heating, include thermal peak amplitude, width, FWHM, area, and volume. Furthermore, exponential growth and exponential decay constants can be fit to the maximum temperature over time (Figure 1. 1) Additionally, in a perfectly homogeneous sample, the thermal peak is smooth and radially symmetric. Small scale heterogeneity in tissue thermal properties perturbs the expected smooth and radially symmetric image.

1.3.3 FDTI spatial resolution

The effective spatial resolution of FDTI depends on the spatial resolution of the thermal camera used, the laser beam width, and the step size between imaging points. A narrower laser beam generates heating over a smaller tissue volume than a wider laser beam, reducing thermal diffusivity-driven blur and high spatial resolution. The spatial resolution of FDTI and a standard widefield DTI using a 405 nm LED was tested using a custom 3D printed phantom that had 1 mm thick pillars printed in rows and spaced 1 mm apart (Figure 1. 3).

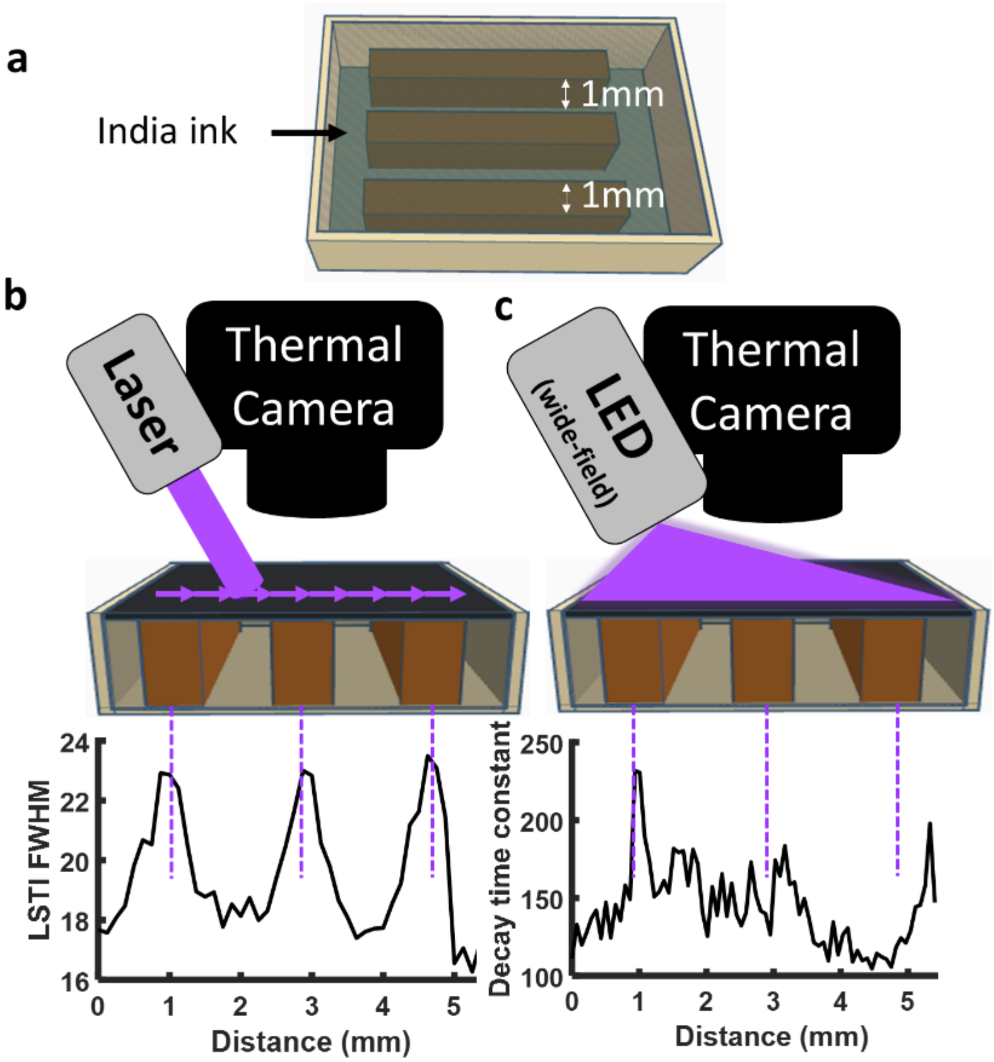

Figure 1. 3 Testing spatial resolution with 3D printed phantoms (a) demonstrates superior spatial resolution for FDTI (b) relative to widefield dynamic thermal imaging (c).

The phantom was filled with India ink solution to obscure the pillars (Figure 1. 3 a). FDTI measurements were taken in 125 micron steps across the phantom and the FWHM for each measurement was extracted and plotted for each step (Figure 1. 3 b). The widefield LED illuminated thermal decay time constants were plotted pixel by pixel against the phantom location (Figure 1. 3 c). The FDTI shows three distinct peaks corresponding to the three pillars, whereas the widefield DTI did not show a correlation to the location on the phantom.

1.3.4 FDTI detects changes in tissue heterogeneity in vivo

Proliferating cells such as tumors can create a high level of disorganization and tissue heterogeneity by recruitment of blood vessels, de-differentiation of cancer cells into different phenotypes, and induction of a robust immune infiltrate. To determine if FDTI can measure malignancy-induced changes in tissue heterogeneity, subcutaneous mouse and rat models of breast cancer were evaluated over the course of tumor development. Two experimental designs with different healthy tissue control sites were investigated: one consisting of the selection of a contralateral site, and another consisting of a temperature-matched control site. FDTI images and videos were acquired in real-time with a thermal camera and a low powered (5mW) laser-induced heat source. The thermal data were processed and analyzed to extract FDTI features based on tissue heat profile.

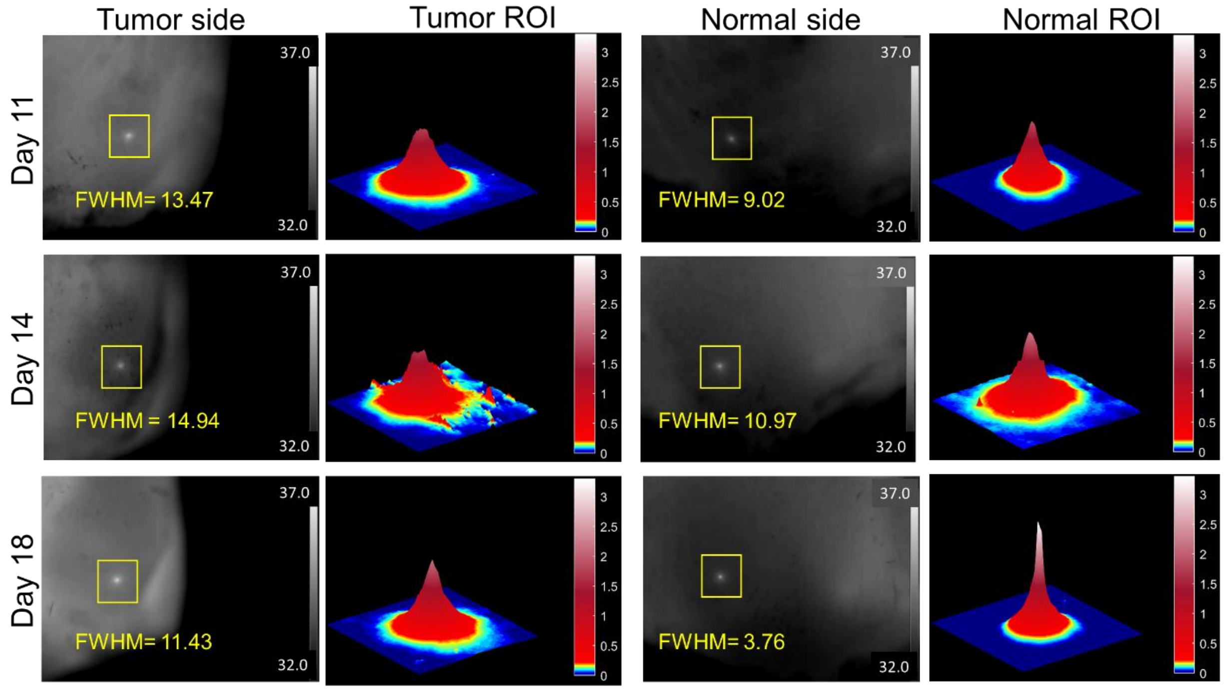

Figure 1. 4 FDTI of one rat throughout tumor progression. Thermal image (left) and corresponding FWHM from FDTI analysis (left center) on tumor. Thermal image (right center) and corresponding FWHM from FDTI analysis (right) from normal tissue over time

A simplified visualization of the FDTI data was obtained by plotting the tissue thermal profiles after 10 seconds of continuous laser stimulation. This allows for a visual comparison of thermal profiles between tumor and healthy tissue. In the early stages, both tumor and healthy tissue exhibited similar but distinguishable heat profiles, measured by FWHM, but this feature diverged as the tumor size increased and the tumor matured (Figure 1. 4). In general, the healthy tissue exhibits a taller and narrower FDTI profile than tumor tissue, which showed a shorter and broader thermal response. As the tumor developed, the thermal response of healthy tissue became sharper and taller. Although the height of the thermal response in the tumor region increased slightly with time, the profile remained broad throughout tumor development. These results point to the potential use of high-resolution FDTI to determine tissue proliferation and heterogeneity. Furthermore, the visual features correspond to consistent findings observed across all of the mouse and rat measurements, which had significantly larger FWHM, standard deviation at steady state, and error when fitting the thermal profiles to a Lorentzian surface plot (Figure 1. 5~Figure 1. 6).

1.3.5 Multiparametric feature classifier enhances the accuracy of tumor detection in a mouse model of cancer

In the mouse experiment, Balb/c mice with subcutaneous breast tumors on the right dorsal flank (n=9) had FDTI measurements made on the tumor and the contralateral sides which served as healthy control (Figure 1. 5 a). Thermal images were collected 10 seconds after turning on the laser, features were extracted and compared with the contralateral-control group. Figure 1. 5 b displays results from three thermal profile features: FWHM, the Lorentzian fitting sum of squared errors (SSE), and the temperature standard deviation at steady state. These features are independent of each other and were tested as classification inputs.

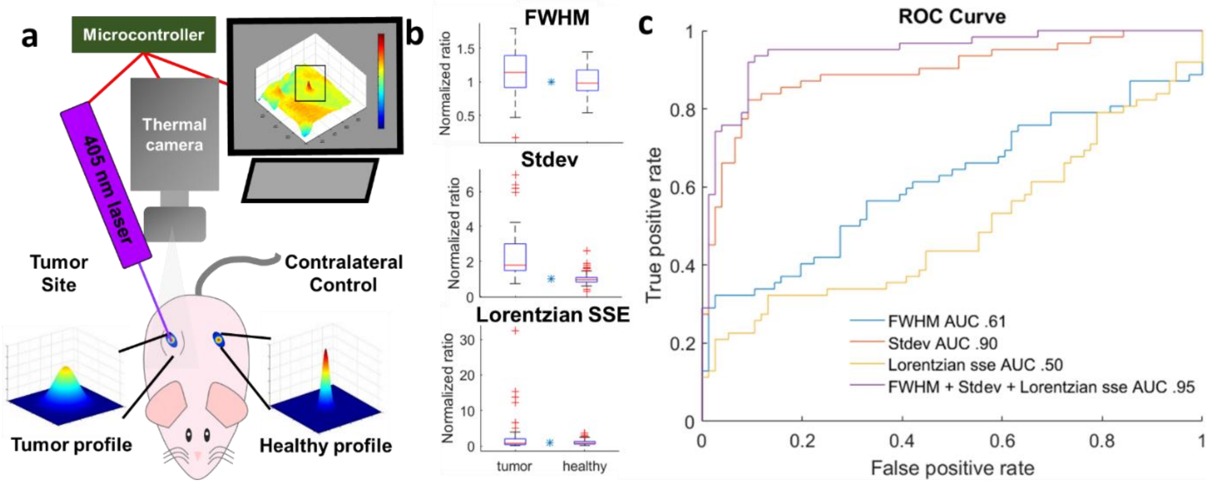

Figure 1. 5 Demonstration of FDTI in the use of cancer detection in a mouse model of breast cancer. a) FDTI experimental setup showing contralateral control experimental design; b) FDTI feature responses between tumor and contralateral control healthy tissues from thermal images of mouse. (n=9, * indicates p-value <0.05). c) Receiver operator characteristic curves from 5-fold cross-validation quadratic discriminant analysis in mice

Results from a 5-fold cross-validation quadratic discriminant analysis are displayed in the form of receiver operator characteristic curves from the three features (Figure 1. 5 c). The area under the curve (AUC) values of single features range from 0.49 to 0.89. However, when combined in a multiple feature classifier, the AUC reached 0.95, demonstrating higher accuracy than any individual feature.

1.3.6 FDTI distinguishes underlying tissue heterogeneity in a rat model of cancer

Thermal imaging is widely used to map body temperature and identify suspicious areas, but the low specificity of the technique has hampered adoption in the clinic[4, 14]. Multiple hot spots may indicate inflammation, infection, or cancer. A unique application of FDTI is the rapid assessment of suspicious lesions that are first flagged using the standard widefield thermal imaging systems. In such a case, it is more relevant to have temperature-matched comparison sites to determine whether thermal stimulation of a suspicious area of tissue can distinguish between cancerous and healthy tissue. In this study, Sprague Dawley rats with subcutaneous right flank breast tumors (n=4) had three measurements acquired from the tumor, and three measurements acquired from temperature-matched sites (Figure 1. 6 a). One of the temperature matched measurements served as the control, and all the remaining measurements were normalized to this control measurement. FDTI data were acquired in a video format, with recording initiated just prior to a 10-second laser exposure, followed by a 10-second observation of thermal recovery. FDTI features were extracted as described in the Methods section, and comparisons were made between features of the tumor and healthy group. Plots between healthy and tumor tissue from the same three features utilized for classification in the mouse study (FWHM, Lorentzian SSE, and steady state temperature standard deviation) were analyzed (Figure 1. 6 b). The trends observed are the same, with tumor tissue having statistically significant higher values than the healthy tissue for all features.

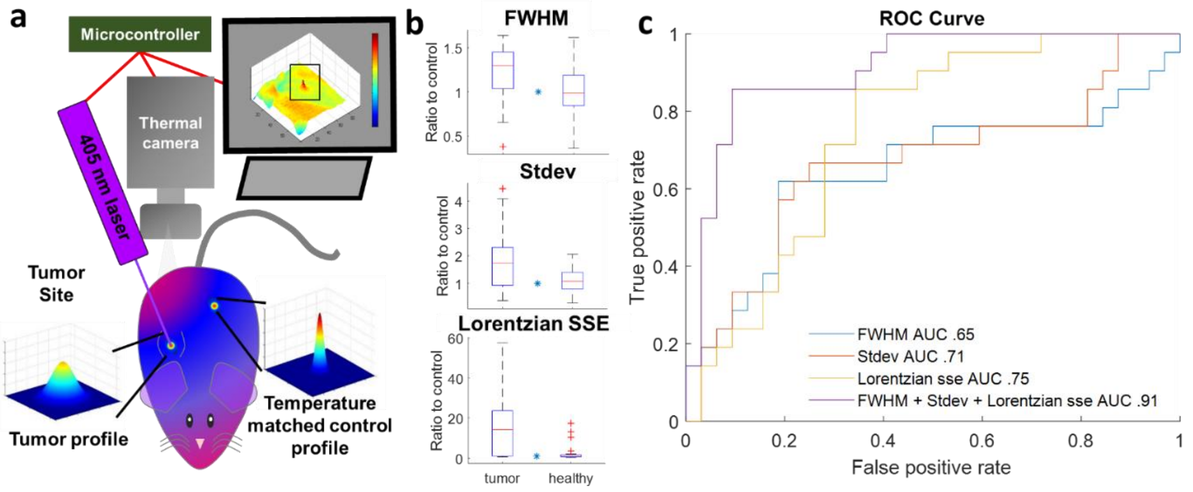

Figure 1. 6 Demonstration of FDTI in the use of cancer detection in a rat model of breast cancer. a) FDTI experimental setup showing and temperature-matched control experimental design; b) FDTI feature responses between tumor and temperature-matched healthy tissues in rats. (, n=4,* indicates p-value <0.05); c) Receiver operator characteristic curves from 5-fold cross-validation quadratic discriminant analysis in rats

Similar to the mouse study, these features were tested as classification inputs. A 5-fold cross-validation quadratic discriminant analysis was displayed in the form of receiver operator characteristic curves from the three features above (Figure 1. 6 c). The area under the curve (AUC) values of single features ranged from 0.65-0.75, but combining them into a multiple feature classifier improved the AUC to 0.91, demonstrating higher accuracy than any individual feature. In addition, the consistency in the multiple feature classifier between mouse and rat studies highlights the robustness of this technique and these features as predictive inputs.

1.4 Discussion

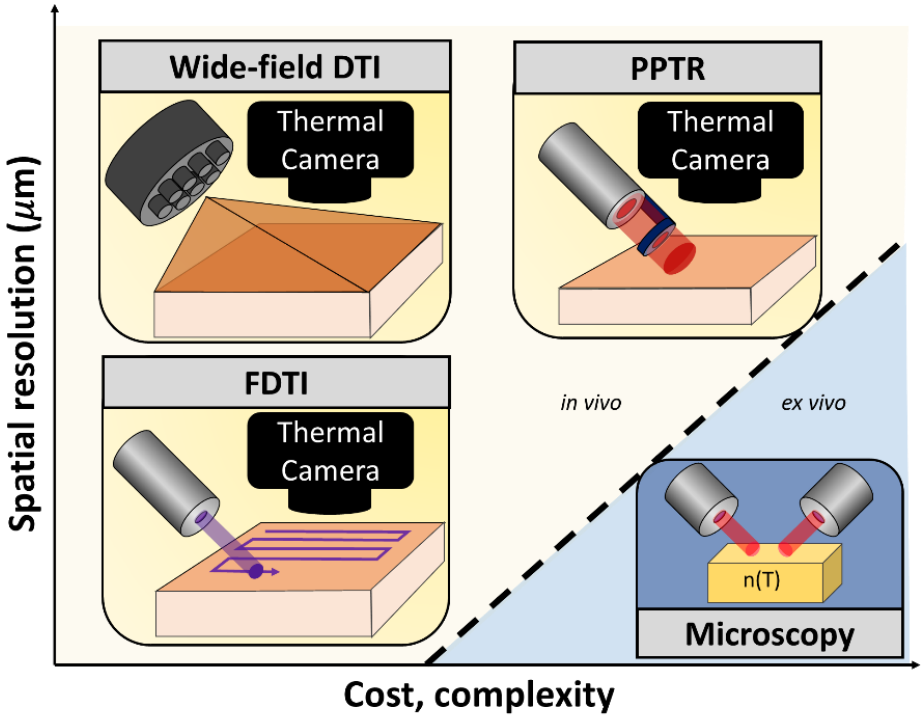

Figure 1. 7 Comparison of dynamic thermal imaging techniques' resolution and complexity

Photothermal techniques, which measure the thermal response of a system to photon absorption, can be used to interrogate the thermal properties of materials. This includes measurement of multiple photothermal sequelae, including change in index of refraction, heating, thermoelastic expansion, secondary infrared irradiation, and photomechanical stresses [15]. For applications at nanoscale, scanning thermal microscopy techniques use thermal probes attached to cantilevers that directly contact the material to detect nanoscale changes in heat flow [16], from which thermal properties can be extracted. At microscale, the 3ω method has been used to measure the thermal conductivity of materials and single cells [17, 18]. A number of microscopes have been developed that take advantage of the local change in refractive index upon chromophore absorption, some of which use vibrational spectroscopy to extract molecular content [15, 19, 20]. Macroscopically, widefield thermal imaging is routinely used in industrial applications such as assessment of electrical connections and bulk material characterization, while DTI has been increasingly used in medical applications [21, 22]. Few methods exist that can probe micro and mesoscopic-resolution applications without the use of bulky, expensive hardware, that limit field applications. To meet this need, we have developed FDTI (Figure 1. 7 **错误!未找到引用源。**).

Existing photothermal methods have reported resolution at sub-micron levels [15, 20, 23], however, the cost and complexity of these techniques have limited their use in the field. In medical applications, more translatable, but significantly lower resolution techniques such as widefield DTI and pulsed photothermal radiometry have been studied. Pulsed photothermal radiometry (PPTR) is a non-contact optical method that applies a pulsed laser to generate heat due to optical absorption and measures thermal diffusivity based on heat propagation through the material [21]. This method has been recently used for physiologic characterization of skin [24] and to predict temperature rise in patients undergoing laser therapy [25]. Both of these techniques apply stimulus over a large area and the subsequent thermal response becomes blurred due to thermal conductivity, significantly reducing the spatial resolution. A recent article achieved sub-diffraction limited thermal imaging of tissue slides stained with exogenous methylene blue nanoparticles for contrast enhancement by irradiating the sample using a scanning focal light beam to prevent thermal blurring[11]. This technique tracked optical absorption induced heating, but did not track heat dissipation over time, confining its sensitivity to optical absorption and specific heat capacity rather than thermal conductivity. Capitalizing upon the successes of these methods, FDTI irradiates small regions of tissue to prevent thermal blur and tracks the response over time, providing sensitivity to heterogeneity in optical and thermal properties. The sub-millimeter resolution demonstrated in our FDTI work is not the absolute resolution limit, rather the resolution is fundamentally limited by spot size, step size, and the thermal resolution of the camera used.

FDTI's instrumentation is exceptionally simple, requiring only a collimated laser and a thermal camera. Furthermore, the extraction of FDTI features is straightforward and can be performed in real time. Indeed, the specifications of FDTI equipment will affect the resolution and sensitivity of the system, but these simple requirements are in stark contrast to high-resolution thermal techniques which utilize expensive laser systems [24], lock-in detection schemes, fragile alignment systems [15, 19-21, 23], or which rely on exogenous contrast[11] which limits in vivo application. In addition, some of the lasers used are painful medical grade therapeutic lasers [24], which highly differ from the painless and low powered irradiation used for FDTI.

FDTI was tested in an in vivo cancer detection application, a possible avenue to pursue in future human studies. A variety of widefield thermal imaging methods have been tested for cancer detection due to their favorable translational characteristics. Some methods aim to improve the accuracy of equilibrium thermal measurements using artificial neural networks and have reported accuracy of 80.95% in tumor detection [26]. DTI has been shown to increase the accuracy significantly (from 54% to 82%) when compared with steady state thermal imaging [27]. Improved classification algorithms have heightened the sensitivity and specificity of this technique to 95-100% and 83-99% respectively, for the diagnosis of skin cancer [5, 28] in a 140 patient trial. While these results are exciting, the spatial resolution limitations of widefield DTI techniques may not allow robust estimation of tumor heterogeneity and margin assessment, which would further expand the utility of dynamic thermal imaging. Additional heat challenge techniques have applied visible light sources including green LEDs that created heat due to absorption by hemoglobin to identify the vascular boundary of tumors [29]. Herein, FDTI had 95% and 91% accuracy in small cohorts of breast cancer mouse and rat models, respectively, using classification based on single point FDTI measurements of cold tumors. A number of quantitative image parameters indicative of cancer were identified from FDTI data. FWHM was significantly higher in cancerous regions, which have higher thermal conductivity than healthy tissues and can thus transfer heat away from the thermal source faster, preventing a large heat buildup. The standard deviation was higher in cancerous tissues and may be due to more heterogeneous tissue that can be observed in tumors. Finally, the goodness of fit to a Lorentzian surface as measured by the sum of squared errors was significantly lower in cancerous tissue, further suggesting that spatial inhomogeneities are more frequent in cancerous tissue and impact the likeness of the FDTI profile to a Lorentzian surface. Importantly, the quantitative nature of the FDTI parameters makes it an objective technique that should not be dependent upon the user or require interpretation, overcoming a large obstacle from standard thermography.

The simplicity of FDTI lends itself to being portable, fast, low cost, and lightweight, and is therefore prime for clinical translation and field applications. This is an important advantage compared to non-widefield thermal methods, which have thus far been performed on tissue sections or in vitro cell samples. Our successful range of experiments spanning 3D printed structures, ex vivo biological tissue, and longitudinal in vivo mouse and rat studies demonstrate the utility of this approach across many biomedical applications and size scales, and warrants further exploration of this technique in human patients. Widefield approaches which have similarly simple and portable instrumentation have shown great promise to positively impact patient care [5, 22, 28, 30], and FDTI is poised to fill the need for simple, inexpensive, and high resolution dynamic thermal imaging.

Development of real-time analysis software and further optimization of the laser irradiation and thermal decay times for scanning and extension into rapid 2D FDTI mapping could further improve FDTI. Although the classification accuracy of in vivo cancer detection was not perfect, the classification was made using single point FDTI measurement that cannot capture the full extent of the tumor's heterogeneous properties. Repeating such experiments with 2D mapping capabilities in larger animal cohorts will be a fairer test of FDTI's diagnostic abilities. Furthermore, depth penetration of the excitation light can be increased by using longer irradiation wavelengths[31], and through longer laser exposure times[32], however, deeper imaging will result in a trade-off of reduced spatial resolution[33].

Interestingly, we observed that mouse and rat tumors progressively grew cold as they increased in size, which is contradictory to human tumors which are known to be warmer than surrounding tissue[34, 35]. However, our finding of cold rodent tumors is supported in literature [36, 37]. This implies that most rodent models do not represent the human disease with respect to an important thermal physiologic parameter. However, a strength of FDTI and dynamic thermal imaging approaches is the sensitivity to thermal properties of the tissue, regardless of baseline temperature. Temperature is known to affect immune response and enzyme activities[38], and these important differences should be considered when conducting cancer research in animal models. Due to this difference in the tumor microenvironment, FDTI trials in humans may yield different results compared to those observed in cold mouse and rat tumors, and should be evaluated independently of the animal data presented herein.

In summary, we have developed FDTI, a platform technology that offers high-resolution and high contrast thermal imaging to applications with sample heterogeneity such as biological tissue. It adds measures of thermal properties to the sources of label-free optical contrast, with the potential to reveal new pathophysiology not yet before seen with conventional optical methods. FDTI addresses an important gap in stimulated thermal imaging with wide-field DTI systems being inexpensive, simple, and clinic-ready but suffering from poor spatial resolution, and thermal microscopes offering high resolution but with costly, complex, non-portable, and ex vivo-only applications (Figure 1. 7).

1.5 Materials and Methods

1.5.1 Experimental FDTI system

The instrumentation used to perform FDTI experiments is shown in Figure 1. 5 a and Figure 1. 6 a. The FDTI system consists of a collimated, low powered, continuous 405 nm laser diode (Laserland, Wuhan, Hubei Province, China). The laser beam profile was characterized and found to be an elliptical Gaussian with FWHM 0.69 mm x 1.35 mm. A polarizer is aligned with the laser beam to limit power output at 5 mW. A FLIR (Wilsonville, OR, USA) T650SC 25 ° high-resolution focal plane array uncooled microbolometer with 640 x 480 pixels, 64 mm x 48 mm field of view, 100 μm spatial resolution, <0.02 ℃ sensitivity, spectral range of 7.5-14 μm, and 30 Hz frame rate is used with a 5.8x Lens (FLIR #T198060) to collect thermal images and videos. The laser is powered using a custom electronic driver circuit controlled by a Teensy LC (Sherwood, Oregon, USA) microcontroller. Both the Teensy and camera are connected to a PC running a custom MATLAB script (MathWorks, Natick, MA) to allow for synchronized, automated control of each component. The script first triggers the camera to record thermal video prior to laser stimulation, then triggers the laser on for a specified pulse duration, and finally continues recording video after the laser is shut off for a sufficient time period to capture return to equilibrium temperature. The laser exposure time for in vivo subcutaneous tumor measurements was tested at 0.1, 1, 3, 5, 10, 20, 30, and 60 seconds to identify the shortest amount of time that reached a plateau in temperature rise, from which 10-second exposure was selected. Similarly, the time until thermal decay plateaued was observed and found to consistently decay within 10 seconds after laser exposure completion.

1.5.2 Experimental image acquisition, processing, and feature extraction

Thermal images and videos are processed and analyzed using our custom image processing pipeline. First, thermal radiometric image or video data is imported into a custom MATLAB graphical user interface (GUI). The user is then prompted to select the laser irradiation point from a thermal preview image. A region of interest (ROI) encompassing the heated tissue is then programmatically generated. A battery of parameters, including peak temperature, thermal peak area, thermal peak volume, 2D Gaussian fitting, 2D Lorentzian fitting, and FWHM are subsequently measured from this ROI. In addition, measures of goodness of fit for temperature rise can be utilized in real-time to ensure appropriate experimental conditions.

1.5.3 FDTI resolution testing

FDTI’s ability to resolve small spatial differences in material properties was tested using a 3D printed phantom composed of black polylactic acid (PLA) filament (Hatchbox 3D, Pomona, CA, USA) in which rows of 1 mm thick pillars were spaced 1 mm apart and filled with a 1000x dilution India ink solution (Higgins, Leeds, MA, USA). The India ink solution provides an optical absorber, and the water and plastic provide thermal conductivity differences on a small spatial scale. To test the spatial resolution as a function of laser beam width, the irradiation beam diameter was adjusted using a 1000 µm pinhole and the beam was translated across the pillars with a 125 µm step size. The data were analyzed by plotting the FWHM and the thermal decay constant was plotted as a function of translated distance.

The spatial resolution of FDTI was directly compared to widefield irradiation DTI techniques by irradiating the phantom with a 405 nm LED with a 1 cm spot size. As analyzed in the literature, the temperature decay after light exposure was fit to an exponential and the decay constant was calculated per pixel in the illumination area. A row spanning the same pillars measured using FDTI was analyzed and per pixel decay time constant was plotted to identify the spatial resolution and directly compare with the FDTI values from the same pillar spacing rows.

1.5.4 Computational model

The FDTI phenomenon was modeled in COMSOL Multiphysics (Burlington, MA, USA) version 5.4.2 by coupling of the Bioheat Transfer and Radiation in Absorbing-Scattering Media modules. This software enabled simulation of heat transfer based on specific properties of the tissue using the finite element method on a custom mesh to solve for the change in heat over time. The model solved Pennes' bioheat equation which requires input for the density, specific heat capacity, initial temperature, ambient temperature, and thermal conductivity of the tissue, blood perfusion rate, and metabolic heat generation, all of which were obtained from values published in the literature (Table 1. 1). Laser-induced heating was incorporated into the model using the Radiation in a Participating Media module. The radiative heat term requires inputs of optical absorption coefficient, scattering coefficient, initial radiative intensity, refractive index, and coefficient of anisotropy. For boundary conditions, the surface was set as a diffuse surface with thermal emissivity and ambient temperature inputs as shown in Table 1. 1. The interior boundaries are set to "open boundaries" and thus allow for heat to transfer through them, and the boundary temperatures are consistent with adjacent internal temperatures throughout the duration of the simulation. Prior to application of the radiative term, the tissue was allowed to self-regulate for two minutes, followed by the application of a 5 mW laser with a Gaussian profile on the tissue for 10 seconds.

Table 1. 1 Parameters used in COMSOL parameter testing

Parameter	Value(s) used	Sources
Absorption Coefficient (1/m)	900 (baseline) 700 (low) 1075 (high)	[39]
Ambient Temperature (K)	296.45	Room temperature
Initial Tissue Temperature (K)	303.45	
Tissue Density (kg/m^3)	1000	[40, 41]
Specific Heat Capacity of Tissue (J/(kg*K))	3000	[41-44]
Metabolic Heat (W/m^3)	200	[45, 46]
Thermal Conductivity (W/(m*K))	0.35 (baseline) 0.21 (low) 0.48 (high)	[40, 41, 43, 44, 47]
Surface Emissivity	0.98	[48]
Refractive Index	1.40	[39]
Blood Perfusion(1/s)	0.001	[49]
Scattering Coefficient(1/m)	2,500	[39]

Coefficient of Anisotropy	0.90	[39]

1.5.5 Computational parameter sweep

The effects of various model parameters on model output were tested using parameter comparison of tissue thermal conductivity and optical absorption at a range of values reported in the literature from physiological studies. Parameter sweep results were analyzed by plotting the cross-section of the surface temperature. The amplitude and FWHM of the thermal peak generated were calculated throughout laser stimulation and compared across parameter values.

1.5.6 Computational testing of biological tissue types

The ability to distinguish between tissue types was tested by evaluating the model using input parameters from fat and muscle tissue based on reported literature values (Table 1. 2). Similar to the parameter sweep, the peak amplitude and FWHM were calculated throughout laser stimulation and compared.

An experiment was designed to test the accuracy of the COMSOL model. Bulk pieces of porcine muscle and porcine fat were experimentally measured using an FDTI system as described below. The amplitude and FWHM were calculated and plotted, and compared to COMSOL simulation results.

Table 1. 2 Parameters used in COMSOL validation of biological tissue types

Parameter	***Porcine Fat***	***Source***	***Porcine Muscle***	***Source***
Absorption Coefficient *(m^{-1})*	150 (λ = 405 nm)	[39, 50]	950 (λ = 405 nm)	[51]

Ambient Temperature (K)	296.45	Room temperature	296.45	Room temperature
Initial Tissue Temperature (K)	294.99	From experimental data	293.34	From experimental data
Tissue Density (kg/m^3)	911	[40, 41]	1090	[40, 41]
*Specific Heat Capacity of Tissue (J/(kg*K))*	2348	[41-44]	3421	[41, 42, 44]
Metabolic Heat (W/m^3)	0	*Ex vivo*, term ignored	0	*Ex vivo*, term ignored
*Thermal Conductivity (W/(m*K))*	0.24	[40, 41, 44]	0.56	[40, 41, 43, 44, 47]
Surface Emissivity	0.98	[48]	0.98	[48]
Refractive Index	1.40	[39]	1.40	[39]
Blood Perfusion (s^{-1})	0	*Ex vivo*, term ignored	0	*Ex vivo*, term ignored
Scattering Coefficient (m^{-1})	7750 (λ = 405 nm)	[51]	7000 (λ = 405 nm)	[51]
Legendre Coefficient of Anisotropy	0.90	[39]	0.90	[39]

1.5.7 In vivo mouse and rat experiments

All animal work was approved and performed under an approved protocol by Washington University's Institutional Animal Care and Use Committee (IACUC). Animals were housed under a 12 hour dark-light cycle.

Two subcutaneous breast cancer models were used. The first subcutaneous model utilized six week-old female Balb/c mice (n=9) that were subcutaneously implanted with 10^6 4T1-Luc-GFP murine breast cancer cells on the right dorsal flank. The tumor size was tracked using calipers and were typically palpable by day 7. Images at steady state and at 10 seconds of laser stimulation on days 7, 8, 10, 11, 14, 16, and 18 were captured post injection. FDTI measurements were acquired on the tumor and matched contralateral sites served as controls.

The second subcutaneous breast cancer model used six week old and adult female Sprague Dawley rats (n=2 each, n=4 total), which were injected with 105 MAT B III mammary adenocarcinoma cells in the right flank. FDTI measurements were acquired on the tumor and temperature-matched regions served as controls.

FDTI videos were taken of the rats every 3-4 days post tumor cell injection. Caliper measurements were taken to track the growth of the tumor. Once a palpable tumor was identified, points were measured on the tumor.

All animals were sacrificed based on humane end-points. Thermal images and videos were used for feature extraction using our image processing pipeline.

1.5.8 Statistical analysis and classification

Statistical analysis was performed using MATLAB R2018a. Multiple image features were extracted from each FDTI image and video as described above. Each feature was correlated using the Spearman correlation against the class label (healthy or cancerous) and ranked to determine which features were most predictive of tissue composition. The ability to distinguish healthy from cancerous tissue based on the individual most predictive features was determined using a t-test with a level of significance set to 0.05. Additional correlation matrix comparing all of the features was calculated to identify independent features, those features serve as individual predictors. Individual predictors and combinations of them were entered to train and evaluate a Quadratic Discriminant Analysis classifier with 5-fold cross-validation using the MATLAB Classification Learner Application. The model performance was evaluated using accuracy measured as area under the receiver operator characteristic (ROC) curve.

1.6 Acknowledgments

This research was supported in part by the National Institutes of Health grants (R01 CA171651, U54 CA199092, R01 EB021048, P50 CA094056, P30 CA091842, S10 OD020129, S10 OD016237, and S10 RR031625), the Department of Defense Breast Cancer Research Program (W81XWH-16-1-0286), and the Alvin J. Siteman Cancer Center Investment Program Research Development Award. CO was supported by a W. M. Keck Foundation Postdoctoral Research Fellowship. We acknowledge Julia Carpenter for her contributions to thermal simulations.

1.7 Contributions

Christine M. O'Brien and Hongyu Meng contributed to experimental design, data collection, image processing and analysis, statistics, interpretation, construction of figures, and writing. Leonid Shmuylovich contributed to experimental design, data collection, data interpretation, construction of figures, and writing. Julia Carpenter conducted thermal simulations and contributed to the construction of figures and writing. Praneeth Gogineni contributed to data analysis and construction of figures. Haini Zhang contributed to data collection. Kevin Bishop contributed to data collection, data analysis, and construction of figures. Suman Mondal contributed to experiment design, data collection, data interpretation, and writing. Gail Sudlow contributed to experimental design and data collection. Clyde Bethea and Cheryl Bethea conceived of the FDTI idea and contributed to experimental design, image analysis, and interpretation. Samuel Achilefu initiated research, co-conceived FDTI implementation, contributed to experimental design, data interpretation, construction of figures, and writing.

1.8 Competing interests, data and Ethical approval

Competing interests:

The authors declare no competing interests.

Data Availability

The datasets generated and analyzed during the current study are available from the corresponding author on reasonable request.

Ethical Approval: All methods were performed in accordance with the relevant guidelines and regulations (i.e. Declaration of Helsinki).

References

1. Topalidou, A., et al., *Thermal imaging applications in neonatal care: a scoping review.* BMC Pregnancy and Childbirth, 2019. **19**(1): p. 381.
2. Bagavathiappan, S., et al., *Infrared thermography for condition monitoring – A review.* Infrared Physics & Technology, 2013. **60**: p. 35-55.
3. Corsi, C., *Infrared: A Key Technology for Security Systems.* Advances in Optical Technologies, 2012. **2012**: p. 15.
4. Vreugdenburg, T.D., et al., *A systematic review of elastography, electrical impedance scanning, and digital infrared thermography for breast cancer screening and diagnosis.* Breast Cancer Research and Treatment, 2013. **137**(3): p. 665-676.
5. Godoy, S.E., et al., *Detection theory for accurate and non-invasive skin cancer diagnosis using dynamic thermal imaging.* Biomedical Optics Express, 2017. **8**(4): p. 2301-2323.
6. Herman, C., *The role of dynamic infrared imaging in melanoma diagnosis.* Expert review of dermatology, 2013. **8**(2): p. 177-184.
7. Oh, G., K.-H. Lee, and E. Chung, *Active thermodynamic contrast imaging for label-free tumor detection in a murine xenograft tumor model.* Biomedical Optics Express, 2017. **8**(11): p. 5013-5026.
8. Nowakowski, A. and M. Kaczmarek, *Active Dynamic Thermography - Problems of implementation in medical diagnostics.* Quantitative InfraRed Thermography Journal, 2011. **8**(1): p. 89-106.
9. Burrell, R.A., et al., *The causes and consequences of genetic heterogeneity in cancer evolution.* Nature, 2013. **501**: p. 338.
10. O'Connor, J.P.B., et al., *Imaging Intratumor Heterogeneity: Role in Therapy Response, Resistance, and Clinical Outcome.* Clinical Cancer Research, 2015. **21**(2): p. 249-257.
11. Bouzin, M., et al., *Photo-activated raster scanning thermal imaging at sub-diffraction resolution.* Nature Communications, 2019. **10**(1): p. 5523.
12. Lawrence, K.P., et al., *The UV/Visible Radiation Boundary Region (385–405 nm) Damages Skin Cells and Induces "dark" Cyclobutane Pyrimidine Dimers in Human Skin in vivo.* Scientific Reports, 2018. **8**(1): p. 12722.
13. Wissler, E.H., *Pennes' 1948 paper revisited.* Journal of applied physiology, 1998. **85**(1): p. 35-41.
14. Omranipour, R., et al., *Comparison of the Accuracy of Thermography and Mammography in the Detection of Breast Cancer.* Breast care (Basel, Switzerland), 2016. **11**(4): p. 260-264.
15. Zharov, V. and D. Lapotko, *Photothermal sensing of nanoscale targets.* Review of Scientific Instruments, 2003. **74**(1): p. 785-788.
16. Gomès, S., A. Assy, and P.-O. Chapuis, *Scanning thermal microscopy: A review.* physica status solidi (a), 2015. **212**(3): p. 477-494.
17. Park, B.K., et al., *Thermal conductivity of biological cells at cellular level and correlation with disease state.* Journal of Applied Physics, 2016. **119**(22): p. 224701.
18. Tong, T. and A. Majumdar, *Reexamining the 3-omega technique for thin film thermal characterization.* Review of Scientific Instruments, 2006. **77**(10): p. 104902.
19. Bai, Y., et al., *Ultrafast chemical imaging by widefield photothermal sensing of infrared absorption.* Science Advances, 2019. **5**(7): p. eaav7127.

20. Lapotko, D.O., et al., *Photothermal time-resolved imaging of living cells.* Lasers in Surgery and Medicine, 2002. **31**(1): p. 53-63.
21. Sergey, A.T., et al., *Non-contact measurement of thermal diffusivity in tissue.* Physics in Medicine & Biology, 2001. **46**(2): p. 551.
22. Pirtini Çetingül, M. and C. Herman, *Quantification of the thermal signature of a melanoma lesion.* International Journal of Thermal Sciences, 2011. **50**(4): p. 421-431.
23. Zhang, D., et al., *Depth-resolved mid-infrared photothermal imaging of living cells and organisms with submicrometer spatial resolution.* Science Advances, 2016. **2**(9): p. e1600521.
24. Verdel, N., et al., *Physiological and structural characterization of human skin in vivo using combined photothermal radiometry and diffuse reflectance spectroscopy.* Biomedical Optics Express, 2019. **10**(2): p. 944-960.
25. Jung, B., et al., *Hand‐held pulsed photothermal radiometry system to estimate epidermal temperature rise during laser therapy.* Skin Research and Technology, 2006. **12**(4): p. 292-297.
26. Ng, E.Y.K. and E.C. Kee, *Advanced integrated technique in breast cancer thermography.* Journal of Medical Engineering & Technology, 2008. **32**(2): p. 103-114.
27. Ohashi, Y. and I. Uchida, *Applying dynamic thermography in the diagnosis of breast cancer.* IEEE Engineering in Medicine and Biology Magazine, 2000. **19**(3): p. 42-51.
28. Godoy, S.E., et al., *Dynamic infrared imaging for skin cancer screening.* Infrared Physics & Technology, 2015. **70**: p. 147-152.
29. Case, J.R., et al., *Noninvasive enhanced mid-IR imaging of breast cancer development in vivo.* Journal of biomedical optics, 2015. **20**(11): p. 116003.
30. Herman, C. and M. Pirtini Cetingul, *Quantitative Visualization and Detection of Skin Cancer Using Dynamic Thermal Imaging.* JoVE, 2011(51): p. e2679.
31. Ash, C., et al., *Effect of wavelength and beam width on penetration in light-tissue interaction using computational methods.* Lasers in medical science, 2017. **32**(8): p. 1909-1918.
32. Zhou, Y. and C. Herman, *Optimization of skin cooling by computational modeling for early thermographic detection of breast cancer.* International Journal of Heat and Mass Transfer, 2018. **126**: p. 864-876.
33. Ntziachristos, V., *Going deeper than microscopy: the optical imaging frontier in biology.* Nature Methods, 2010. **7**: p. 603.
34. Shada, A.L., et al., *Infrared thermography of cutaneous melanoma metastases.* The Journal of surgical research, 2013. **182**(1): p. e9-e14.
35. Anbar, M., *Hyperthermia of the cancerous breast: analysis of mechanism.* Cancer Letters, 1994. **84**(1): p. 23-29.
36. Song, C., et al., *Thermographic assessment of tumor growth in mouse xenografts.* International Journal of Cancer, 2007. **121**(5): p. 1055-1058.
37. Xie, W., et al., *Evaluation of the ability of digital infrared imaging to detect vascular changes in experimental animal tumours.* Int J Cancer, 2004. **108**(5): p. 790-4.
38. Messmer, M.N., et al., *Mild cold-stress depresses immune responses: Implications for cancer models involving laboratory mice.* BioEssays : news and reviews in molecular, cellular and developmental biology, 2014. **36**(9): p. 884-891.
39. Jacques, S.L., *Optical properties of biological tissues: a review.* Physics in Medicine and Biology, 2013. **58**(11): p. R37-R61.

40. Duck, F.A., *Chapter 2 - Thermal Properties of Tissue*, in *Physical Properties of Tissues*, F.A. Duck, Editor. 1990, Academic Press: London. p. 9-42.
41. MCINTOSH, R.L. and V. ANDERSON, *A COMPREHENSIVE TISSUE PROPERTIES DATABASE PROVIDED FOR THE THERMAL ASSESSMENT OF A HUMAN AT REST.* Biophysical Reviews and Letters, 2010. **05**(03): p. 129-151.
42. van den Berg, P.M., et al., *A computational model of the electromagnetic heating of biological tissue with application to hyperthermic cancer therapy.* IEEE Trans Biomed Eng, 1983. **30**(12): p. 797-805.
43. Collins, C.M., et al., *Temperature and SAR calculations for a human head within volume and surface coils at 64 and 300 MHz.* J Magn Reson Imaging, 2004. **19**(5): p. 650-6.
44. Van Leeuwen, G.M., et al., *Calculation of change in brain temperatures due to exposure to a mobile phone.* Phys Med Biol, 1999. **44**(10): p. 2367-79.
45. Cetingul, M.P. and C. Herman, *A heat transfer model of skin tissue for the detection of lesions: sensitivity analysis.* Phys Med Biol, 2010. **55**(19): p. 5933-51.
46. Ma, J., et al., *Thermal damage in three-dimensional vivo bio-tissues induced by moving heat sources in laser therapy.* Scientific Reports, 2019. **9**(1): p. 10987.
47. Bowman, H.F., E.G. Cravalho, and M. Woods, *Theory, measurement, and application of thermal properties of biomaterials.* Annu Rev Biophys Bioeng, 1975. **4**(00): p. 43-80.
48. Soerensen, D., et al., *Determining the emissivity of pig skin for accurate infrared thermography*. Vol. 109. 2014. 52–58.
49. Jiang, S.C., et al., *Effects of thermal properties and geometrical dimensions on skin burn injuries.* Burns, 2002. **28**(8): p. 713-717.
50. Bashkatov, A.N., et al., *Optical properties of human skin, subcutaneous and mucous tissues in the wavelength range from 400 to 2000 nm.* Journal of Physics D: Applied Physics, 2005. **38**(15): p. 2543-2555.
51. Filatova, S.A., I.A. Shcherbakov, and V.B. Tsvetkov, *Optical properties of animal tissues in the wavelength range from 350 to 2600 nm*. Vol. 22. 2017: SPIE. 1-7, 7.

Chapter 2: Multiparametric focal dynamic thermal imaging classifier detects early-stage tumors with high accuracy

This chapter is based on a submitted manuscript. Hongyu Meng, Christine M. O'Brien, Haini Zhang, Leo Shmuylovich, Karen Nwosu, Suman B. Mondal, Julie Prior, Katie Duncan, Gail Sudlow, Samuel Achilefu.

I wrote the manuscript in collaboration with the help of Christine, Leo, and Hanru, designed and executed the experiments, analyzed the data, made illustrations and edited the manuscript with collaborators.

2.1 Abstract

Significance: Early tumor detection improves prognosis and survival rates, necessitating the development of new imaging technologies for cancer screening, with a focus on label-free techniques. While conventional thermal imaging is attractive for this application, low contrast for early-stage tumors and low detection accuracy prevent its adoption as a clinical tool for cancer screening.

Aim: The primary objective of this study is to develop a multiparametric approach for detecting early-stage tumors in mice using focal dynamic thermal imaging (FDTI).

Approach: FDTI uses a narrow beam, low-power 405 nm laser to stimulate a finite target tissue area and perturb the thermal equilibrium in that region. The ensuing thermal response is captured with a high-resolution thermal camera. Blinded stimulation of different regions on a tumor-bearing mouse is followed by FDTI thermal features extraction and analysis. Bioluminescence imaging (BLI) was used to establish ground truth regarding the tumor region. Changes in thermal features were evaluated as a function of tumor progression. Tumors were identified as "early-stage" until they became visible by conventional thermal imaging or palpable.

Results: BLI identified subcutaneously implanted cancer cells in mice before they formed palpable tumors in mice. Unlike conventional static thermal imaging, FDTI successfully detected early-stage tumors based on the differential response of tumor and normal tissue during laser stimulation and thermal recovery periods. Further, the shape of the thermal recovery response was more irregular compared to normal tissue. The irregular shape of the 3D thermal recovery plots of tumors compared to normal tissue suggests the contribution of the heterogeneous tumor environment to the response pattern. Quantitative multiparametric FDTI feature classifier successfully predicted tumor onset with high accuracy (~90%). Inversion of the extracted FDTI features (tumor/normal tissue ratio) with tumor progression offers a potential prediction model for estimating tumor stage.

Conclusion: FDTI can detect tumors exhibiting subtle thermal characteristics with high accuracy at early stages when they are not detectable by conventional static thermal imaging. The simplicity, portability, low cost and use of nonionizing radiation make FDTI attractive as an alternative imaging technology for point-of-care cancer screening.

Keywords: laser, dynamic thermal imaging, tumor, cancer, screening, detection.

2.2 Introduction

Recent improvements in infrared optics and sensors have increased the applications of thermal imaging in the medical field.[1-7] Biomedical thermal imaging uses thermal cameras to visualize the body's heat profile.[8-10] This non-contact, label-free technique is attractive for use in hospitals, patient care settings, and research laboratories because of its portability, ease of use, and real-time image display capability. Clinically, some medical conditions such as vasodilation, inflammation, and cancer typically exhibit elevated temperatures in patients, which forms suspicious hot spots.[11-13] These thermal features can be used to distinguish abnormal from surrounding healthy tissues. As a result, the U.S. Food and Drug Administration (FDA) approved conventional thermal imaging for limited clinical applications, including temperature measurements and mapping abnormal heat patterns in the body.

Previous studies have demonstrated the benefits of improved prognosis when tumors are detected at early stages compared to late stages.[14-19] For example, the 5-year breast cancer survival rate when diagnosed at stage I is 98%, while a stage IV diagnosis is only 27%.[20] Similarly, the

5-year survival rate for melanoma is 99% for diagnosis at a localized stage and 27% for distant stage.[21] Given its many advantages, thermal imaging technology would ideally be useful for screening patients to distinguish between health and cancerous tissue. However, temperature differences caused by early-stage tumors may not always be stable and distinguishable from surrounding healthy tissue.[22] The temperature difference of tumors is mainly caused by alterations in perfusion and metabolic activity.[23-26] Because early-stage tumors are small, the thermal signals from small cancerous tissues easily blend into the healthy surrounding tissues, minimizing the contrast that would otherwise be seen in large, later-stage tumors. This has resulted in poor sensitivity and specificity when tested as early-stage cancer diagnostics.[27] Moreover, dynamic changes caused by normal metabolism or non-cancer-associated disease could further confound thermal imaging data.

To improve the accuracy of image classification, deep learning tools such as deep convolutional neural networks have been used in different fields.[28-32] However, these methods usually require large data sets,[30] which are not readily available in some biomedical thermal imaging research areas such as breast cancer.[33] An alternative approach to enhance the accuracy of this technique is dynamic thermal imaging (DTI), which leverages the different thermal characteristics of cancer compared to normal tissues.[13, 34, 35] For example, melanoma has higher thermal conductivity compared to healthy tissue.[36, 37] DTI reveals these differences by applying a hot or cold stimulus over a target area, which disrupts the local tissue thermal balance and enables probing of thermal properties by recording the tissue temperature response from the stimulus. Analysis of the rate of temperature rise and fall yields higher contrast with improved specificity to distinguish healthy and cancerous tissues. Thus, the enhanced differential response to stimuli between diseased and normal tissue has allowed the use of DTI in multiple tumor detection studies.[36, 38-41]

While DTI is arguably a major advance in biomedical thermal imaging, the application of thermal stimulus over a large area of tissue and the ensuing thermal conductivity blends subtle differences in small areas of tissue, which decreases potentially attainable high spatial resolution and signal contrast. Recently, we developed focal dynamic thermal imaging (FDTI) to overcome this problem.[42] FDTI uses a narrow laser beam to generate a heat rise in a small area, reducing neighboring tissue crosstalk and improving spatial resolution and contrast. Similar to DTI, the rate of temperature rise and fall can be used to probe thermal properties. In addition, tissue heterogeneity can be interrogated by quantifying different features, such as stimulation peak value and full width at half maximum (FWHM). However, the ability of FDTI to detect early-stage tumors has not been explored.

Here, we tested the hypothesis that the high spatial resolution and tissue contrast provided by FDTI will detect early-stage tumors compared to conventional steady state thermal imaging. Tumor growth in mice implanted with luciferase-expressing tumor cells was tracked using bioluminescence imaging (BLI). Before tumors were visible or detectable by palpation, we initiated blinded steady state thermal imaging and FDTI, which was continued until tumors were sufficiently large to be detected by both techniques. BLI was used to validate which of the multiple FDTI stimulation points corresponded to the small tumor and labeled as "tumor points". Using a thermal feature classifier generated from the analysis of how the FDTI features of early-stage cancerous tissue differed from healthy tissue over different stages of tumor growth, we demonstrated that FDTI could detect early tumors with high accuracy.

2.3 Materials and methods

2.3.1 Mouse model and bioluminescence Imaging

All animal studies were approved and performed under an approved protocol by Washington University's Institutional Animal Care and Use Committee (IACUC). Two subcutaneous breast cancer mouse models were used to investigate the ability of FDTI to detect early-stage tumors. We subcutaneously implanted $3*10^4$ 4T1-Luc-GFP murine breast cancer cells on the right dorsal flank of 6-week-old female BALB/c mice (n = 9; Charles River Laboratories Inc. Wilmington, MA). In the second model, $2*10^6$ HT1080-Luc human sarcoma cells were implanted subcutaneously in the flanks of 6-week-old immunodeficient NCI Athymic NCr-nu/nu nude mice (n=10; Charles River Laboratories Inc. Wilmington, MA). Tumor growth was monitored over time until the tumors became visible and palpable. The tumor can be observed by naked eye or steady state thermal imaging without stimulation in some mice around day 15 for BALB/c 4T1-Luc-GFP, and day 22 for nude HT1080-LUC.

For BLI, mice were anesthetized using inhaled isoflurane (2% vaporized in O_2) and intraperitoneally injected with 100 mg/kg D-luciferin in PBS (Gold Biotechnology, St. Louis, MO, USA) for imaging. BLI was performed to locate tumors using an IVIS Lumina system (PerkinElmer, Waltham, MA). The BLI color image was reported in radiance as photons/sec/cm^2/steradian (p/s/cm^2/sr).

2.3.2 FDTI system

We previously described the FDTI system in detail,[42] which is illustrated in **错误!未找到引用源。**. Briefly, the system is equipped with a 5mW, collimated, 405 nm laser diode (Laserland, Wuhan, Hubei Province, China) with spot FWHM of 0.69 mm × 1.35 mm. Thermal images and videos were captured using a high-resolution microbolometer (FLIR T650SC 25°, Wilsonville, OR, USA) and lens (FLIR T198060). The laser output and thermal data capture were controlled via custom electronics which were connected to a laptop computer running a custom MATLAB (MathWorks, Natick, MA) script.

2.3.3 Steady state thermal imaging and FDTI procedure

FDTI measurements were acquired from the dorsal flank every 2~3 days starting on day 2 (4T1-Luc-GFP) and day 6 (HT1080-Luc) post-inoculation of the cancer cells until day 15 or day 25 post-injection for the two tumor models, respectively. Analysis of each mouse was discontinued once the tumor was palpable or could be visualized with the naked eye. Six black dots were painted on each mouse for positioning.

Blinded steady state thermal scans were acquired on the right and left dorsal flank, as well as 2-4 FDTI measurements per side. During FDTI measurements, 4 thermal markers (black paper and plastic markers) were placed near the black dots painted on the mouse before imaging for positioning to enable co-registration with the BLI images. For each spot, a color image was acquired before laser stimulation, followed by 1 s baseline recording at steady state. Thermal video recording continued after a 10 s laser stimulation, followed by 5 s of thermal recovery. The data were imported into a custom MATLAB script for processing and analysis. Bioluminescence imaging was performed after FDTI measurements.

2.3.4 Image processing and analysis

Registration

BLI results were used to determine tumor location (**错误!未找到引用源。**). Three registration methods featured in the MATLAB image registration toolbox were used for each set of images: manually selecting feature points, generating corner points, and generating scale-invariant feature transform features. Compared to others, the manually selecting method performed best in test group with the smallest average root mean square error and was therefore used for all subsequent image registration. All the FDTI spots that localized on the BLI signal area were labeled "tumor", and FDTI measurements outside BLI signal were labeled "normal".

Early stage

Tumors were classified as "early-stage" when identified by BLI but were invisible to the naked eye or traditional thermal imaging.

Feature and analysis

FDTI videos were first imported into MATLAB. For each video, a user selects the region of interest (ROI) based on the location of the laser stimulation spots. FDTI features were extracted from the ROI, including mean value, standard derivation, peak temperature, full width at half maximum (FWHM), 2D Lorentzian surface fitting parameters ($d + e\left[1 + \left(\frac{y-h}{k}\right)^2\right] / \left[1 + \left(\frac{x-f}{g}\right)^2\right]$), 2D Gaussian fitting parameters, exponential growth and exponential decay time constants, subarea (area under the thermal rise curve), subarea binary (the sum of all the pixels larger than zero in subarea).

Next, the breathing artifact was quantified by checking feature stability and any data that did not meet the criteria were removed. The filter standard is included in the feature stability component. A Spearman correlation matrix was calculated to identify independent features that could be combined for multiparametric classification. The MATLAB Classification Learner App was used to test each feature and feature combinations to train and evaluate classifier performance using 5-fold cross-validation. Model accuracy was evaluated using area under the receiver operator characteristic (ROC) curve (AUC).

2.3 Results

2.3.1 FDTI system and image registration

A simplified schematic of the FDTI platform is shown in Figure 2. 1. A low-powered 405 nm laser was used to stimulate finite regions on mouse tissue. This process perturbed the thermal equilibrium of the tissue. After a short stimulation period, the laser was turned off and tissue was allowed to reestablish thermal equilibrium. A high-resolution thermal camera captures both steady state (before thermal stimulation) and FDTI-induced changes in the thermal profiles of tissue in the ROI. Using a multiparametric analysis method, differences in the thermal response were used to identify disease from healthy tissue.

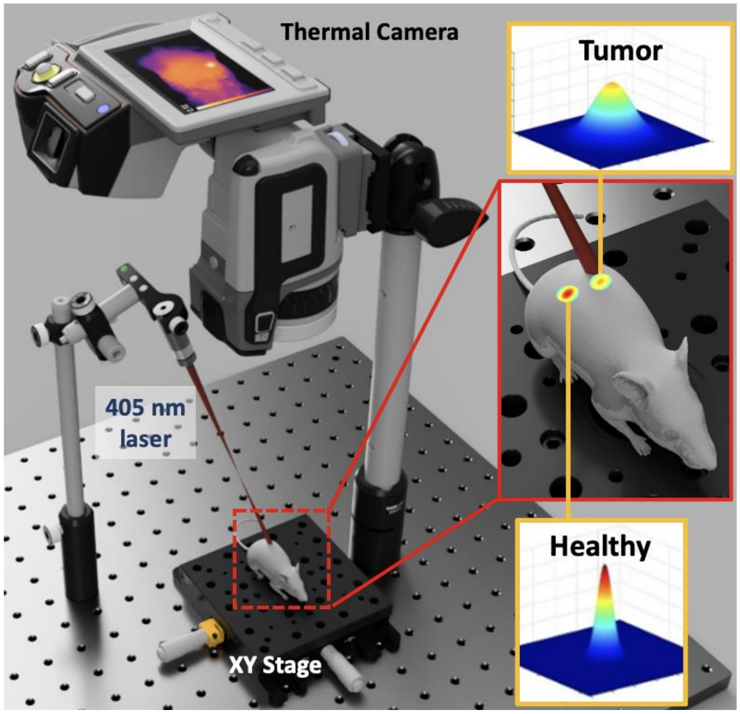

Figure 2. 1 Illustration of FDTI setup including data collection and analysis outcomes.

Bioluminescence, thermal (with laser spot) and color images of tumor-bearing mice were recorded and registered (Figure 2. 2). Fiducial markers were placed at different positions to enable co-registration of the disparate images and data comparison (see Methods section).

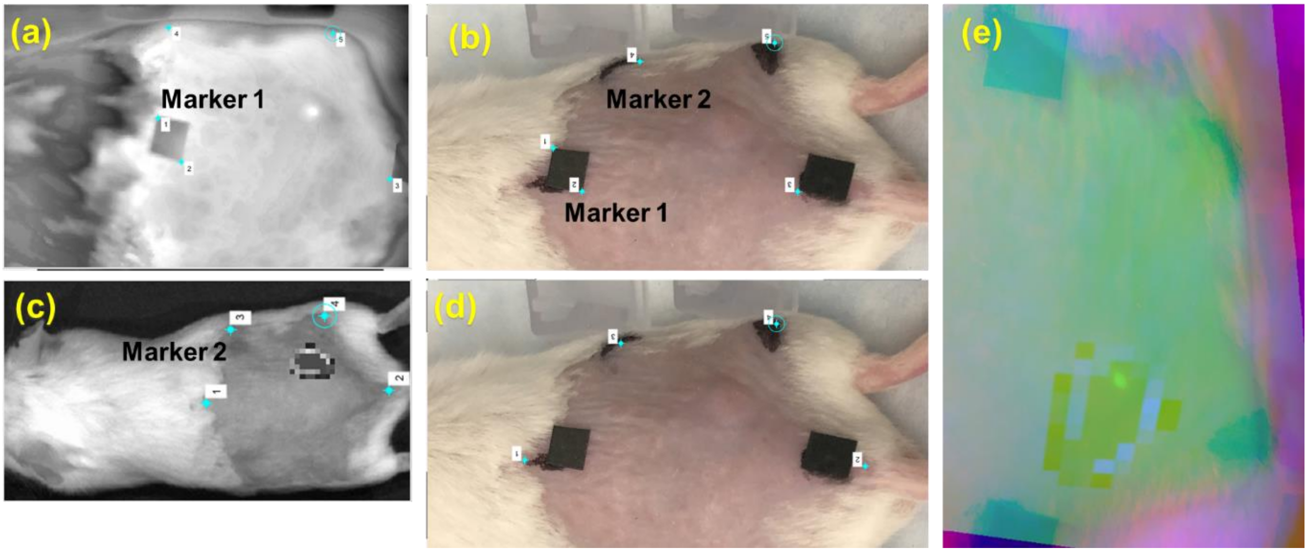

Figure 2. 2. Representative image registration procedure. (a) Thermal image, gray scale. (b) Color image and spots selected for thermal-color matching. (c) BLI image, gray scale; the dark spot is the BLI signal of tumor. (d) Color image and spots selected for BLI-color matching. (e) Co-registered bioluminescence-focal dynamic thermal images showing the laser spot overlapped with the tumor, which is identified as "tumor spot".

2.3.2. Conventional static thermal imaging is less effective in detecting early-stage tumor

In traditional thermal imaging, the temperature of the tissue and the surrounding and contralateral reference areas are compared. Regions are considered suspicious if significant temperature differences are found. Large tumors are typically warmer than healthy tissue in humans, but there is a dart of evidence that non-palpable small tumors can generate thermal effects detectable by static imaging methods. An interesting phenomenon observed by many researchers is that most subcutaneous mouse tumor models are cold, regardless of the size.[42] This endothermal phenomenon presents additional challenges in distinguishing early-stage tumors. To explore the role of immune response in mouse tumor models, we used 4T1-Luc-GFP cells in the immunocompetent BALB/c mice and HT1080-Luc in immunodeficient NCI Athymic NCr-nu/nu mice. Figure 2. 3 **错误!未找到引用源。**a-l shows an example of steady state traditional thermal and bioluminescence images of a single 4T1-Luc-GFP tumor in a BALB/c mouse over time. Each group has three images, thermal image, BLI, and mean value boxplot. We used green and yellow circles to denote the contralateral side and tumor area, respectively. BLI served as the ground truth for tumor location. For the boxplot, the average values per 0.1 s in the 1 s steady state image from the tumor and the contralateral (normal) areas were compared.

Similarity of the thermal images in both the tumor and normal tissue areas made it difficult to differentiate the tissue by visual inspection. Furthermore, results of the data analysis of both regions were not statistically significant. Attempts to adjust the temperature range, manually set the threshold, and reduce the ROI did not improve the outcome. Extension of the procedure to HT1080-LUC tumor model (Figure 2. 3 m-x) exhibited similar results as the 4T1-Luc-GFP mouse model. Together, these results demonstrate that the subcutaneous tumors in mice remained "cold" regardless of the tumor size and immune status of the model. Notably, conventional static thermal imaging is not sufficiently stable and accurate to detect early-stage tumors from surrounding healthy tissue.

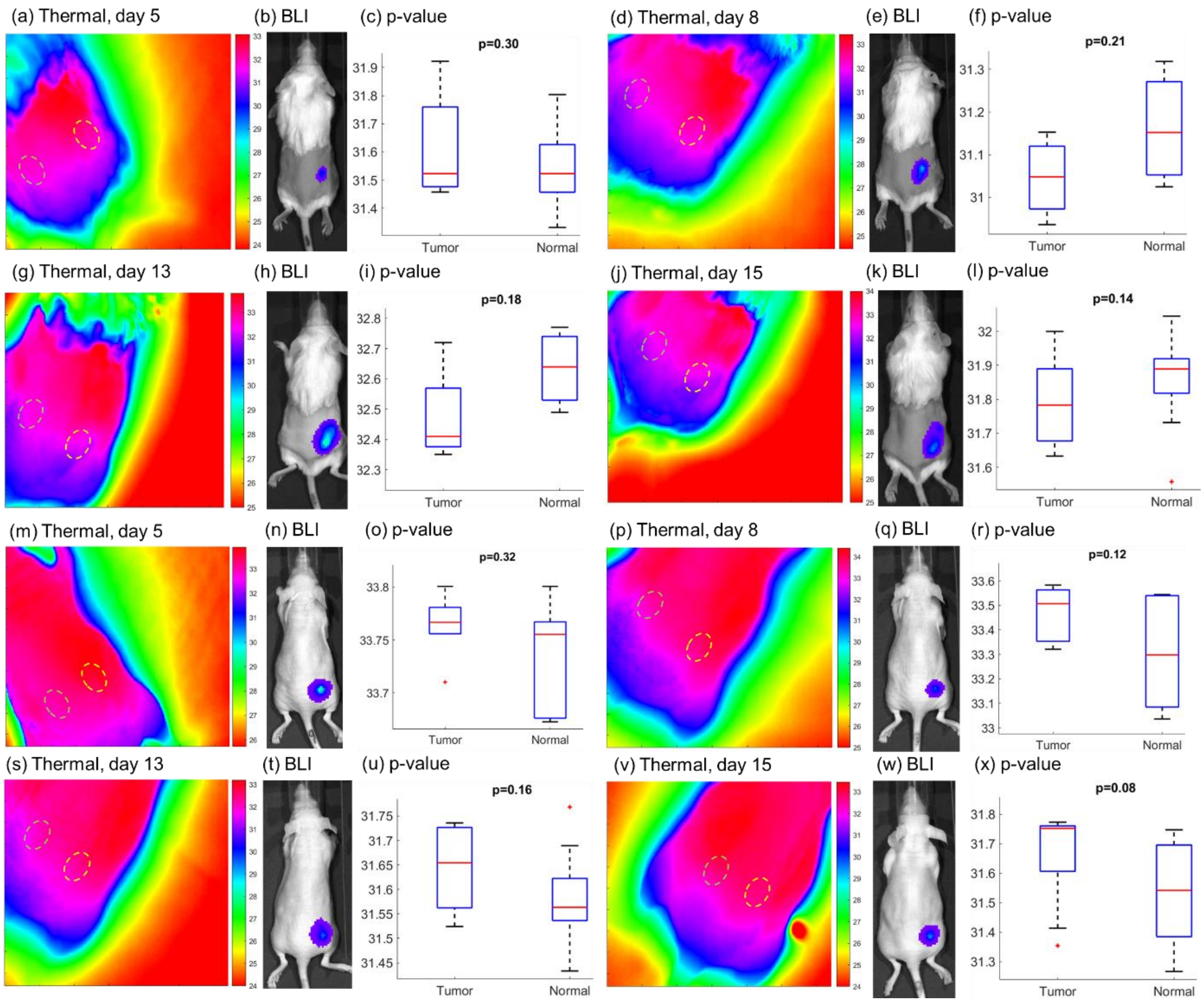

Figure 2. 3 Comparison of conventional thermal imaging with BLI for early tumor detection. (a-l) 4T1-Luc-GFP tumor model in BALB/c mouse without laser stimulation, on days 5,8,13 and 15. (m-x) HT1080-LUC tumor in nude mouse without laser stimulation on days 5,8,13 and 15. (a,d,g,j.m,p,s,v) Thermal images; yellow circle represents area validated by BLI as tumor region, green circle represents the non-tumor contralateral side. (b,e,h,k,n,q,t,w) BLI showing the location and progression of tumors over time. Due to the different growth rates between the two tumor models, BALB/c and nude mice groups are shown on a BLI scale of 1*10^7–5*10^8 and 5*10^6–5*10^8, respectively. (c,e,i,l,o,r,u,x) Statistical analysis of mean ROI value in tumor versus non-tumor contralateral areas; statistiscal signifance is set at $p<0.05$.

2.3.3. Optimizing FDTI features' stability is critical for data reproducibility

In the process of collecting data from mice, we observed that mouse breathing affected the stability of the laser stimulation points, exhibiting periodic fluctuations in some collected data. Consequently, we sought to exclude respiration artifacts while retaining stable features stable for each point. We collected each point multiple times, and no obvious respiration impact on the point was observed during the collection process. The fluctuation range of the feature under this condition provided us with a reference value for the threshold.

Figure 2. 4 highlights the stability of extracted features from an HT1080-LUC tumor-bearing mouse. For ease of illustration, the subpanels are grouped into full thermal image, thermal imaging of the ROI, and a 3D view of the tumor ROI where temperature is plotted in the z axis (Figure 2. 4 a-c), and the corresponding healthy tissue (Figure 2. 4 d-f). The laser stimulation was performed three times per spot and three features for tumor (Figure 2. 4 g-i) and normal (Figure 2. 4 j-l) are shown for each stimulus: peak value (subtracted steady state background), FWHM on the x-axis, and FWHM on the y-axis. We found that the volatility of these features is different: the rise, near stationary, and decay phases of the plot. Among the different features examined, FWHM exhibited a high fluctuation rate, attaining up to 15% for FWHM-y on tumor at 11 s. Based on these findings, we estimated the increase and decay rate threshold of data at each stage and set the threshold to 15%. Thus, features with fluctuations greater than this threshold were not used in subsequent FDTI analysis.

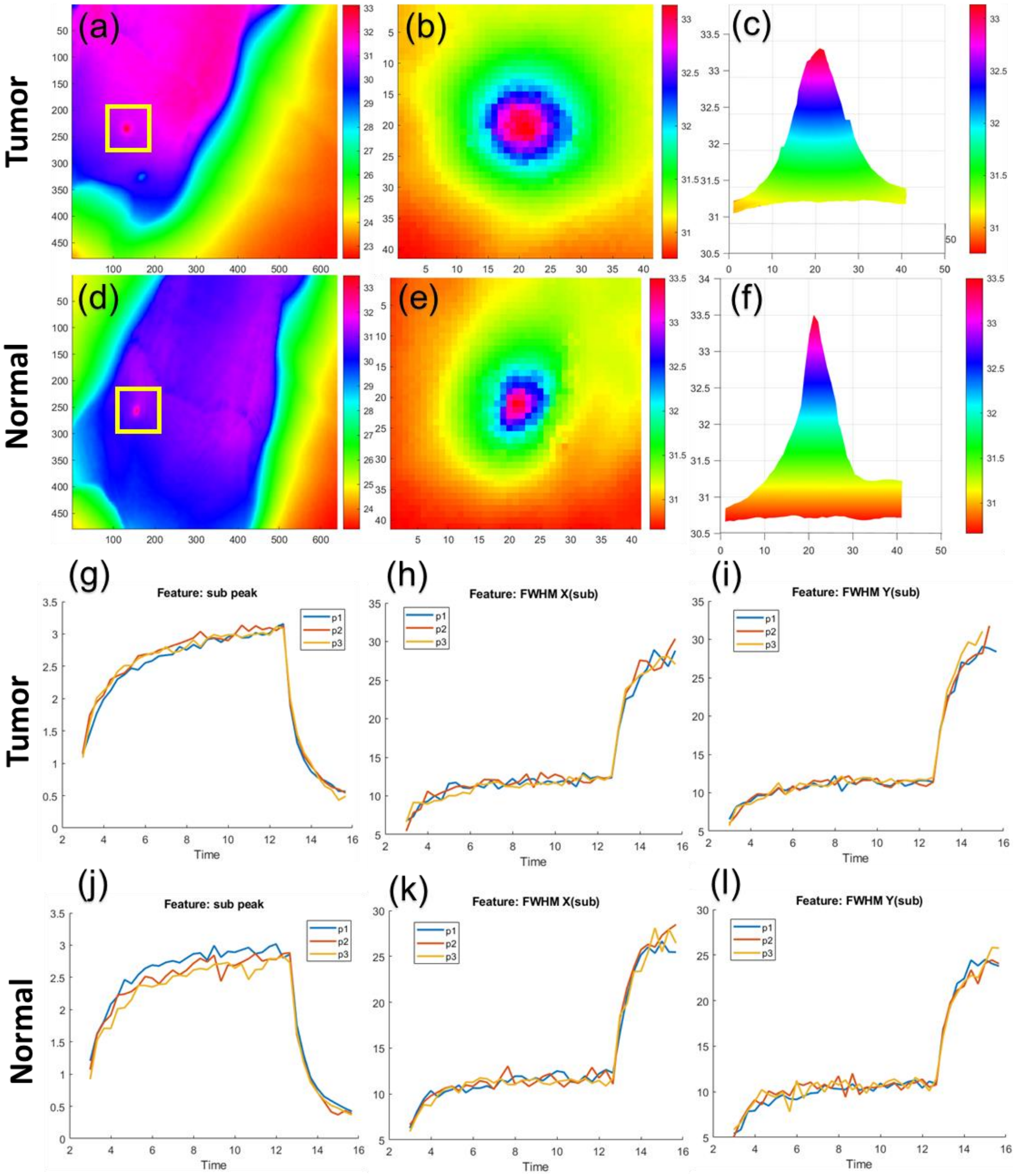

Figure 2. 4 Feature stability test using HT1080-LUC tumor in nude mice. (a) Full image, (b) ROI, and (c) ROI temperature side view of tumor thermal response. (d) Full image, (e) ROI, and (f) ROI temperature side view of normal tissue thermal response. (g) Peak value, (h) FWHM-x, and (i) FWHM-y of the thermal response on tumor at the same spot from three laser stimulations. (j) Peak value, (k) FWHM-x, and (l) FWHM-y of the thermal response on normal tissue from three laser stimulations.

2.3.4 FDTI detects early-stage tumors

Perturbation of thermal equilibrium with laser spot stimulation is expected to induce a different response of tissue, depending on the underlying composition and physiologic parameters such as cell types, vascular density, and blood flow. To determine if FDTI can identify tumors before they are detectable by conventional static thermal imaging, we compared the thermal response profiles by tumor and normal tissue in both immunocompetent (4T1-Luc-GFP BALB/c; Figure 2. 5 a-h) and immunodeficient (HT1080 in NCI Athymic NCr-nu/nu; Figure 2. 5 i-p) mouse models of cancer. Thermal maps were acquired after initiating laser stimulation on the tumor (Figure 2. 5 a,i) and normal (Figure 2. 5 b,j) tissue for 10 s. The corresponding representative side views of background-subtracted ROI from the thermal maps are shown in Figure 2. 5 e,f,m,n. In both animal models, the tumor exhibited lower peak temperature and larger FHWM than normal tissue. We also evaluated tissue response profiles after turning off the laser for 3s. The thermal decay map (Figure 2. 5 c,d,k,l) and corresponding background-subtracted ROI side view show that the tumor peak temperature rapidly appeared to approach that of normal tissue (Figure 2. 5 g,h,o,p). However, the thermal recovery time for the stimulated hot spot on the tumor was generally longer than normal tissue. Further, the shape of the thermal recovery response was more irregular compared to normal tissue. While the endothermal nature of the tumors in mice may account for the decreased peak temperature during stimulation compared to normal tissue, the heterogeneity of the tumor environment could lead to disparity in the response time, which creates an irregular thermal response shape after laser stimulation.

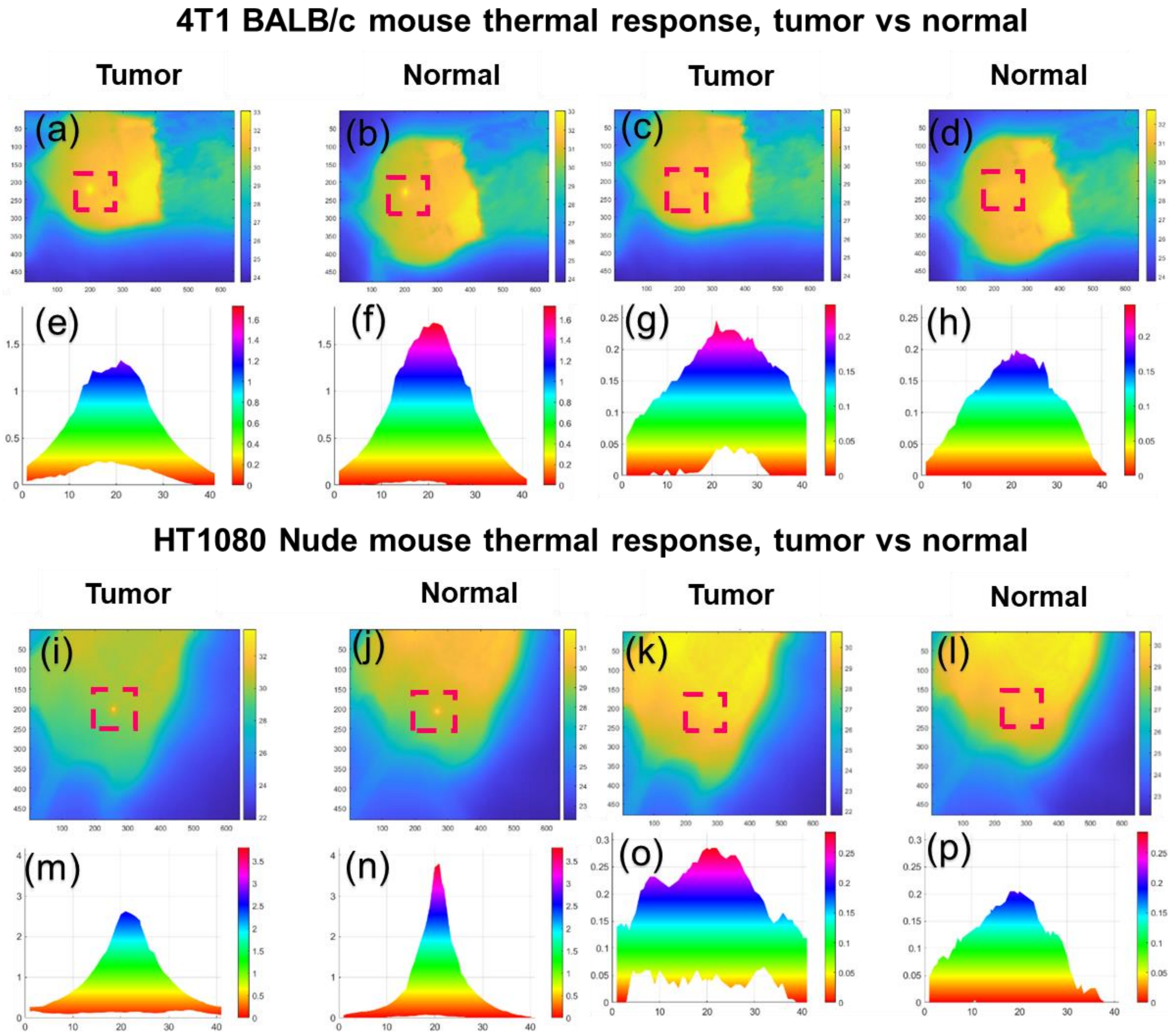

4T1 BALB/c mouse thermal response, tumor vs normal

HT1080 Nude mouse thermal response, tumor vs normal

Figure 2. 5 Representstive thermal response of different tumor models in mice. (a-h) Response of 4T1-Luc-GFP tumors in BALB/c mice. (i-p) Response of HT1080-Luc tumors in nude mice. (a) Laser spot on tumor for 10 s; the red square is ROI. (b) Laser spot on normal tissue for 10 s. (c) Recovery stage of (a) after turning off laser for 3 s.(d) Recover stage of (b) after turning off laser for 3 s. (e-h) The thermal pattern of ROI in (a-d). (i-p) Corresponding representative images under similar conditions described in (a-h) in HT1080-Luc tumors in nude mice.

2.3.5. Multiparametric FDTI feature classifier predicts tumor onset with high accuracy

To determine the classification accuracy, we extracted FDTI features from healthy and tumors spots (Figure 2. 6 错误!未找到引用源。 and Table 2. 1). Five features were tested as classification inputs with five-fold cross-validation analysis: 2D Lorentzian fitting adjusted r-square error (L adjrsq), the sum of all pixels in the subtracted ROI where the thermal increase is greater than zero (subarea larger than zero), FWHM in x- and y-axes of subtracted background thermal images (FWHM X sub, FWHM Y sub), and peak temperature dividing FWHM in the x-axis and y-axis (pow/(x*y)). Samples were randomly divided into a training set (included 80% of the FDTI measurements) and testing set (included 20% of the FDTI measurements). Results are shown as ROC curves. The AUC values of single features were variable and did not exceed 0.75. When a multi-feature classifier was used, the AUC values reached 0.81 and 0.87 in 4T1-Luc-GFP BALB/c) and HT1080-Luc NCI Athymic NCr-nu/nu mice. This finding demonstrates that FDTI can be used to identity tumors at a stage when they are not visible by conventional static thermal imaging.

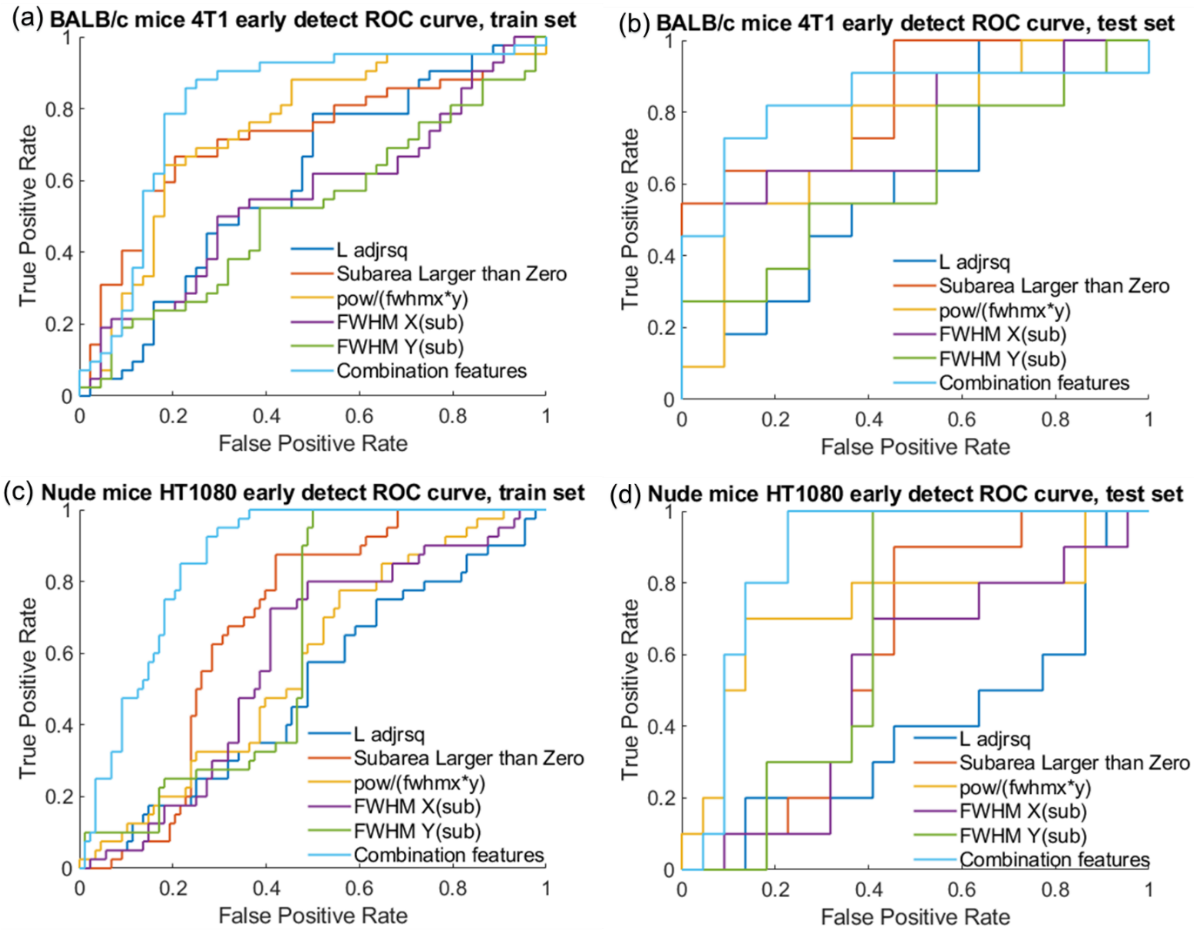

Figure 2. 6 ROC curves for tumor and normal feature classifier. (a) Training set ROC curves of 4T1-Luc-GFP tumors in BALB/c mice. Features shown are Lorentzian fitting adjusted r square, Subtracted area>0, FWHM x and y, peak/(FWHMx*FWHMy), and 5-feature combined classifier. AUC values are shown in Table 2. 1. (b) Test set ROC curves of 4T1-Luc-GFP tumors in BALB/c. (c) Training set ROC curves of HT1080-Luc tumors in nude mice. (d) Test set ROC curves of HT1080-Luc tumors in nude mice.

Table 2. 1 Single feature and multiple-feature combination classifier AUC values

Feature **Mice**	**Lorentz fitting adjusted rsq**	**Sub area larger than zero**	**Pow/(FWHMx*FWHMy)**	**FWHM x**	**FWHM y**	**Combine**

BALB/c train set AUC	0.6012	0.7947	0.7424	0.5574	0.5179	**0.8347**
BALB/c test Set AUC	0.6198	0.7192	0.7438	0.7521	0.6281	**0.8106**
Nude train set AUC	0.5045	0.6835	0.5733	0.5878	0.6273	**0.8773**
Nude test Set AUC	0.3955	0.6045	0.7318	0.5364	0.6636	**0.8634**

To assess how FDTI features changed as the tumors grew, we plotted the ratio of FDTI features from tumor spots and normal spots over time (tumor / normal, shown in Figure 2. 7). We evaluated the following features: Peak/(FWHM in x axis * FWHM in y axis), shown as Pow/(fwhmx*y); the sum of all the pixels larger than zero in subtracted steady state thermal image, shown as Subarea Larger than zero; and Lorentzian fitting adjusted r-square, shown as L adjrsq. The black line in the figure represents the tumor-to-normal ratio of average temperature in the steady state, simulating the conventional thermal imaging method. Other lines represent different feature tumor/normal ratios. The corresponding bioluminescence images before laser stimulation and the associated intensity values are shown in Figure 2. 7 for comparison. Threshold settings of 1*10^7 – 5*10^8 and 5*10^6 – 5*10^8 were used for BALB/c and NCI Athymic NCr-nu/nu groups, respectively.

Unlike the HT1080-Luc model, the BLI intensity for 4T1-Luc-GFP tumor model started to decrease by day 15, suggesting the onset of necrosis. As the tumor grew, the tumor/normal ratio of some features gradually increased or decreased. By using conventional thermal imaging as a benchmark, some features exhibited significant differences by day 5 post-tumor inoculation. Our data show that tumor progression leads to an inversion of the features, which depends on the tumor type. Future studies explore the relationship between the feature inversion of tumor/normal tissue ratio and the onset of necrosis. In addition, the tumor stage-dependent feature changes suggest that certain features may be optimal for cancer detection at different stages of tumor progression. Thus, validating this trend in a large cohort of diverse tumors could offer a prediction model for estimating tumor stage using the ratios of specific features.

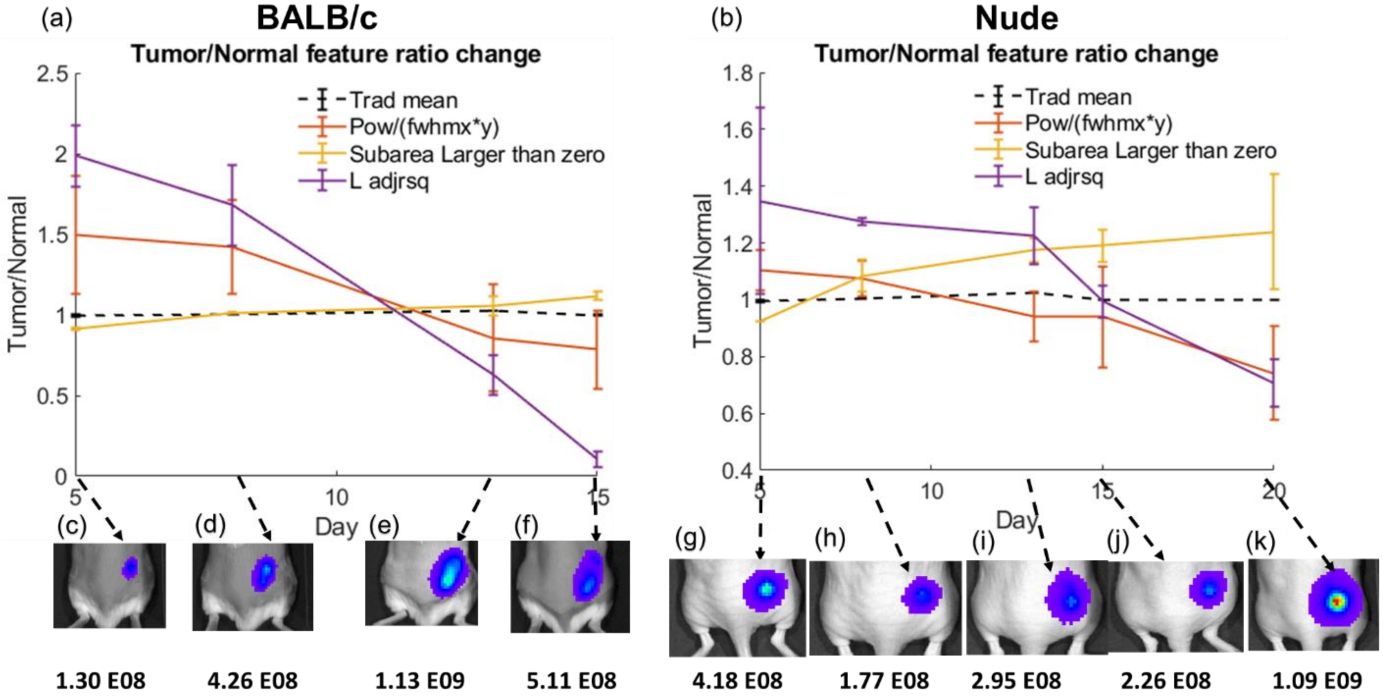

Figure 2. 7: Change in tumor-to-normal feature ratio during the study. (a) 4T1-Luc-GFP tumor in BALB/c mice. (b) HT1080-LUC tumor in nude mice. Black dotted line: average value ratio of tumor area/normal area. Other lines: feature ratio of tumor/normal. (c-f) Related BLI for BALB/c mice, on days 5, 8, 13 and 15. (g-k) Related BLI for nude mice on days 5,8,13,15 and 20. BLI intensity scale is shown below images (c-k). BALB/c and nude mice groups are shown on a BLI scale of 1*10^7–5*10^8 and 5*10^6–5*10^8, respectively.

2.4 Discussion

Early tumor detection is important for improving patient survival and prognosis. Perhaps advances in portable screening technologies could address issues associated with the lack of access to current screening systems found at major hospitals. With the new trend of building hospitals closer to patients in the USA, developing cancer-screening systems for point-of-care applications will help decrease health disparity and enable early disease detection. Within this context, the use of nonionizing radiation for label-free thermal imaging presents an advantage over standard imaging methods. The problem, however, with conventional thermal imaging is that the early-stage tumors are unlikely to exhibit thermal signatures that are significantly different from surrounding normal tissue. Our previous study demonstrated that stimulating finite tissue volumes with lasers, followed by dynamic thermal imaging with a high-resolution camera, could delineate tumors from surrounding tissue.

Our data confirmed that temperature differences between early-stage tumors and normal tissue are not statistically significant to distinguish them. While previous dynamic thermal imaging studies have focused on imaging mature tumors, our current work evaluated the feasibility of using FDTI to detect the onset of tumors. Implementation of reference BLI data allowed us to define tumor location and differentiate it from non-tumor tissue. To prevent bias in data acquisition and analysis, laser stimulation was performed at points and data collected before confirming the location of tumors with BLI. Our study also considered how the immune system could affect the thermal response. Cancer is a disease of inflammation that involves an intricate interplay between tumor-supporting and repressive immune cells.[43, 44] We found the immunocompetent BALB/c and immunodeficient NCI Athymic NCr-nu/nu models grew at different rates. For this reason, it was important to acquire and analyze data when both tumor models were largely in the growth phase to minimize discrepancies caused by differences in the tumor stage.

The two tumor models used in this study responded similarly to laser stimulation. Probably, immune cells in the immunodeficient subcutaneous tumors were not fully integrated into the tumor microenvironment at the early stages of tumor development. A spontaneous tumor model could more adequately recapitulate the human cancer environment. Our data consistently showed that the peak temperature during laser stimulation was higher in tumors than in normal tissue. This is expected because the tumors are slightly colder than normal tissue. However, a different thermal response profile could be obtained in human patients, where the tumors are typically hotter than the surrounding tissue.[12] Nonetheless, the response is expected to be tissue-dependent. The decay phase of our data appears to provide information about tumor heterogeneity. The environment of tumors consists of multiple cell types, new blood vessels, and distorted flow dynamics.[45] After laser stimulation, each cellular component of the tumor tissue could dissipate heat differently, correlating the observed irregular-shaped thermal decay response in both tumor models (Figure 2. 5).

Although visual inspection of the images shown in Figure 2. 5 provides evidence of tumor vs. non-tumor regions before the tumors are detectable by conventional thermal imaging techniques, extracting and analyzing thermal features of FDTI provides quantitative information about the potential of using this technique for early tumor detection. With AUC up to 0.88, our study demonstrates that FDTI is capable of detecting small tumors with high accuracy. Optimization of the stimulation area, intensity, and time can all be achieved by adjusting the laser beam. Although the speed of data acquisition can be improved significantly, only 16 s were used to collect data for each point, making the technology suitable for screening multiple suspicious areas.

Some characteristics of FDTI could provide additional diagnostic information. A particular case is the changes in thermal features with tumor progression (Figure 2. 7). As the tumor progressed, the spot size of the laser stimulation site (subarea larger than zero) increased correspondingly.

This finding agrees with a previous study demonstrating that the tumors are more sensitive to heat and have higher thermal conductivity than non-tumor tissues.[46-50] The inversion of three of the thermal features shown in Fig. 7 as the tumor grew is striking. While the physical and molecular underpinnings of this finding require extensive studies in the future, it demonstrates that certain features could be more sensitive for cancer detection at different stages of growth. For example, the points of intersection between two or more features could represent a change in tumor heterogeneity, vascular density, or other pathophysiologic and metabolic conditions. In the immunocompetent BALB/c mice, all three features exhibited a close intersection point at about 12 days post tumor inoculation, but the immunodeficient NCI Athymic NCr-nu/nu mice had three different intersection points. Correlating these trends with the intrinsic pathophysiology of cancer could elevate the impact of FDTI beyond cancer screening.

FDTI is still a relatively new technique with many opportunities for improvement. For example, testing FDTI in animal models with different skin pigmentation will test the challenges of adopting the method for cancer screening. Perhaps, adapting parameters used to estimate melanin content in the skin could be used to estimate the appropriate input light for each patient.[51-54] Furthermore, stability of the laser spot is critical to obtain reproducible data. Since breathing is the primary cause of motion artifact in this study, it was easily corrected by analyzing feature stability and setting a threshold to filter the data. However, other factors order than breathing could confound FDTI data in patients, requiring the development of a modular approach to address the larger problem.

2.5 Conclusion

FDTI is a non-contact, non-invasive, label-free imaging device that can detect tumors before they are visible by conventional static thermal imaging, naked eye, or palpation. Multiparametric analysis revealed some thermal features that help to improve the accuracy of early cancer detection. Beyond cancer detection, the consistent changes in thermal features with tumor progression could provide additional information about tumor heterogeneity and pathophysiology. FDTI requires further optimization and testing in multiple cancer types before clinical translation for cancer screening or detection.

Disclosures

The authors declare that there are no conflicts of interest related to this article.

Acknowledgments

This study was supported by grants from the National Institutes of Health (R01 EB030987, R01 CA260855, U54 CA199092, R01 EB021048, P30 CA091842, P30 CA091842-19S3, P30 AR073752, R01 AR067491, S10 OD027042, S10 OD016237, S10 RR031625, and S10 OD020129), the Department of Defense Breast Cancer Research Program (W81XWH-16-1-0286), and the Siteman Investment Program Research Development Award.

Code, Data, and Materials Availability

The raw data for this study were generated at Washington University in St. Louis. Data or materials supporting this study's findings are available from the corresponding author SA.

References

1. Bagavathiappan, S., et al., *Infrared thermography for condition monitoring – A review.* Infrared Physics & Technology, 2013. **60**: p. 35-55.
2. Brzezinski, R.Y., et al., *Automated thermal imaging for the detection of fatty liver disease.* Scientific Reports, 2020. **10**(1): p. 15532.
3. Topalidou, A., et al., *Thermal imaging applications in neonatal care: a scoping review.* BMC Pregnancy Childbirth, 2019. **19**(1): p. 381.

4. Kasiteropoulou, D., A. Topalidou, and S. Downe, *A computational fluid dynamics modelling of maternal-fetal heat exchange and blood flow in the umbilical cord.* PLoS One, 2020. **15**(7): p. e0231997.
5. Wearn, C., et al., *Prospective comparative evaluation study of Laser Doppler Imaging and thermal imaging in the assessment of burn depth.* Burns, 2018. **44**(1): p. 124-133.
6. Chojnowski, M., *Infrared thermal imaging in connective tissue diseases.* Reumatologia, 2017. **55**(1): p. 38-43.
7. Kacmaz, S., et al., *The use of infrared thermal imaging in the diagnosis of deep vein thrombosis.* Infrared Physics & Technology, 2017. **86**: p. 120-129.
8. Ammer, K., *The Glamorgan Protocol for recording and evaluation of thermal images of the human body.* Thermol Int, 2008. **18**(4): p. 125-44.
9. Tc, I.S.O. and S.I. Sc62D, *Particular requirements for the basic safety and essential performance of screening thermographs for human febrile temperature screening*. 2008.
10. Iso, T.R., *Medical electrical equipment—deployment, implementation and operational guidelines for identifying febrile humans using a screening thermograph*. 2009.
11. Collins, A.J. and J.A. Cosh, *Temperature and biochemical studies of joint inflammation. A preliminary investigation.* Annals of the rheumatic diseases, 1970. **29**(4): p. 386.
12. Lawson, R.N. and M.S. Chughtai, *Breast cancer and body temperature.* Canadian medical association journal, 1963. **88**(2): p. 68.
13. Anbar, M., *Clinical thermal imaging today.* IEEE Engineering in Medicine and Biology Magazine, 1998. **17**(4): p. 25-33.
14. Nixon, A.J., et al., *Relationship of patient age to pathologic features of the tumor and prognosis for patients with stage I or II breast cancer.* Journal of Clinical Oncology, 1994. **12**(5): p. 888-894.
15. Karim, S., et al., *Association Between Prognosis and Tumor Laterality in Early-Stage Colon Cancer.* JAMA Oncology, 2017. **3**(10): p. 1386-1392.
16. Rudolph, E., et al., *Effects of tumour stage, comorbidity and therapy on survival of laryngeal cancer patients: a systematic review and a meta-analysis.* European Archives of Oto-Rhino-Laryngology, 2011. **268**(2): p. 165-179.
17. Velez, N.F., et al., *Association of Advanced Leukemic Stage and Skin Cancer Tumor Stage With Poor Skin Cancer Outcomes in Patients With Chronic Lymphocytic Leukemia.* JAMA Dermatology, 2014. **150**(3): p. 280-287.
18. Siegel, R.L., et al., *Colorectal cancer statistics, 2020.* CA: a cancer journal for clinicians, 2020. **70**(3): p. 145-164.
19. Feng, R.M., et al., *Current cancer situation in China: good or bad news from the 2018 Global Cancer Statistics?* Cancer communications, 2019. **39**(1): p. 1-12.
20. DeSantis, C.E., et al., *Breast cancer statistics, 2019.* CA: a cancer journal for clinicians, 2019. **69**(6): p. 438-451.
21. Keung, E.Z. and J.E. Gershenwald, *The eighth edition American Joint Committee on Cancer (AJCC) melanoma staging system: implications for melanoma treatment and care.* Expert review of anticancer therapy, 2018. **18**(8): p. 775-784.
22. Foster, K.R., *Thermographic detection of breast cancer.* IEEE Eng Med Biol Mag, 1998. **17**(6): p. 10-4.
23. Wu, Z., et al., *A basic step toward understanding skin surface temperature distributions caused by internal heat sources.* Physics in Medicine and Biology, 2007. **52**(17): p. 5379-5392.

24. Jiang, L., W. Zhan, and M.H. Loew, *Modeling static and dynamic thermography of the human breast under elastic deformation.* Physics in Medicine and Biology, 2010. **56**(1): p. 187-202.
25. Alfano, R.R., et al., *Parametric study of different contributors to tumor thermal profile*, in *Optical Biopsy XII*. 2014.
26. Fu, Z.-J., et al., *Numerical investigation on the effect of tumor on the thermal behavior inside the skin tissue.* International Journal of Heat and Mass Transfer, 2017. **108**: p. 1154-1163.
27. Kennedy, D.A., T. Lee, and D. Seely, *A Comparative Review of Thermography as a Breast Cancer Screening Technique.* Integrative Cancer Therapies, 2009. **8**(1): p. 9-16.
28. Yadav, S.S. and S.M. Jadhav, *Thermal infrared imaging based breast cancer diagnosis using machine learning techniques.* Multimedia Tools and Applications, 2020.
29. Petrie, T., et al., *Melanoma Early Detection: Big Data, Bigger Picture.* Journal of Investigative Dermatology, 2019. **139**(1): p. 25-30.
30. Esteva, A., et al., *Dermatologist-level classification of skin cancer with deep neural networks.* Nature, 2017. **542**(7639): p. 115-118.
31. Haenssle, H.A., et al., *Man against machine: diagnostic performance of a deep learning convolutional neural network for dermoscopic melanoma recognition in comparison to 58 dermatologists.* Annals of Oncology, 2018. **29**(8): p. 1836-1842.
32. Mambou, S.J., et al., *Breast cancer detection using infrared thermal imaging and a deep learning model.* Sensors, 2018. **18**(9): p. 2799.
33. Houssein, E.H., et al., *Deep and machine learning techniques for medical imaging-based breast cancer: A comprehensive review.* Expert Systems with Applications, 2021. **167**: p. 114161.
34. Qi, H. and N.A. Diakides, *Infrared imaging in medicine*. 2007, CRC Press Boca Raton.
35. Jones, B.F., *A reappraisal of the use of infrared thermal image analysis in medicine.* IEEE Transactions on Medical Imaging, 1998. **17**(6): p. 1019-1027.
36. Okabe, T., et al., *First-in-human clinical study of novel technique to diagnose malignant melanoma via thermal conductivity measurements.* Sci. Rep., 2019. **9**(1): p. 3853.
37. Herman, C. and M.P. Cetingul, *Quantitative Visualization and Detection of Skin Cancer Using Dynamic Thermal Imaging.* Jove-Journal of Visualized Experiments, 2011(51).
38. Oh, G., K.H. Lee, and E. Chung, *Active thermodynamic contrast imaging for label-free tumor detection in a murine xenograft tumor model.* Biomedical Optics Express, 2017. **8**(11): p. 5013-5026.
39. Vreugdenburg, T.D., et al., *A systematic review of elastography, electrical impedance scanning, and digital infrared thermography for breast cancer screening and diagnosis.* Breast cancer research and treatment, 2013. **137**(3): p. 665-676.
40. Rassiwala, M., et al., *Evaluation of digital infra–red thermal imaging as an adjunctive screening method for breast carcinoma: A pilot study.* International Journal of Surgery, 2014. **12**(12): p. 1439-1443.
41. Gurjarpadhye, A.A., et al., *Infrared Imaging Tools for Diagnostic Applications in Dermatology.* SM journal of clinical and medical imaging, 2015. **1**(1): p. 1-5.
42. O'Brien, C.M., et al., *Focal dynamic thermal imaging for label-free high-resolution characterization of materials and tissue heterogeneity.* Scientific Reports, 2020. **10**(1): p. 12549.

43. Munn, L.L., *Cancer and inflammation.* Wiley Interdisciplinary Reviews: Systems Biology and Medicine, 2017. **9**(2): p. e1370.
44. Greten, F.R. and S.I. Grivennikov, *Inflammation and cancer: triggers, mechanisms, and consequences.* Immunity, 2019. **51**(1): p. 27-41.
45. Fukumura, D. and R.K. Jain, *Tumor microenvironment abnormalities: causes, consequences, and strategies to normalize.* Journal of cellular biochemistry, 2007. **101**(4): p. 937-949.
46. Zhu, D., et al., *Monitoring thermal-induced changes in tumor blood flow and microvessels with laser speckle contrast imaging.* Applied Optics, 2007. **46**(10): p. 1911-1917.
47. Ren, Y., et al., *Thermal dosage investigation for optimal temperature distribution in gold nanoparticle enhanced photothermal therapy.* International Journal of Heat and Mass Transfer, 2017. **106**: p. 212-221.
48. Bagaria, H.G. and D.T. Johnson, *Transient solution to the bioheat equation and optimization for magnetic fluid hyperthermia treatment.* International Journal of Hyperthermia, 2005. **21**(1): p. 57-75.
49. Mital, M. and R.M. Pidaparti, *Breast Tumor Simulation and Parameters Estimation Using Evolutionary Algorithms.* Modelling and Simulation in Engineering, 2008. **2008**: p. 756436.
50. Chanmugam, A., R. Hatwar, and C. Herman, *Thermal analysis of cancerous breast model*, in *Int Mech Eng Congress Expo*. 2012. p. 134-143.
51. Eichhorn, R., et al., *Early diagnosis of melanotic melanoma based on laser-induced melanin fluorescence.* Journal of Biomedical Optics, 2009. **14**(3): p. 034033.
52. Salomatina, E., et al., *Optical properties of normal and cancerous human skin in the visible and near-infrared spectral range.* Journal of Biomedical Optics, 2006. **11**(6): p. 064026.
53. Colombo, L.L., et al., *Photothermal effect by 808-nm laser irradiation of melanin: a proof-of-concept study of photothermal therapy using B16-F10 melanotic melanoma growing in BALB/c mice.* Biomedical optics express, 2019. **10**(6): p. 2932-2941.
54. Pirtini Çetingül, M. and C. Herman, *Quantification of the thermal signature of a melanoma lesion.* International Journal of Thermal Sciences, 2011. **50**(4): p. 421-431.

Chapter 3: FDTI system optimization

This chapter describes the optimization of the FDTI imaging system, including assumptions, experimental design, test procedures and results. The collaborators in this section include Leo Shmuylovich, Christine O'Brien, Hanru Zhang, Lei Fang, Hengbo Huang, and other laboratory members. I wrote the chapter, designed and executed the experiments, analyzed the data, organized the information, and made most illustrations.

3.1 Abstract

This chapter mainly introduces the optimization of FDTI imaging system. In order to reduce the imaging time in the hardware, we extended the FDTI system and proposed a new design. On the software, we tested feature selection and tried methods to accelerate data collection and analysis. In terms of automating the system and enhancing the robustness of the system, we made and tested registration markers, tested multiple image registration, target recognition and motion correction methods, and proposed a system optimization scheme. These works help to apply the FDTI system to the clinical environment.

3.2 Introduction

In the previous work, we built Focal dynamic thermal imaging (FDTI) platform, which can achieve faster speed, higher resolution and higher accuracy in early tumor detection compared with traditional thermal imaging and dynamic thermal imaging (DTI) technology.

However, if we want to use the FDTI system for clinical acquisition, there are still some problems to be solved. The first issue is about time. In previous experiments, it took 16 seconds for FDTI to collect a point, including 1 second in the steady state, 10 seconds in the rising stage, and 5 seconds in the recovering stage. When only a few points need to be collected, this is acceptable. But, the resolution of FDTI technology is affected by the spot size, which limits its acquisition speed when the user need to scan a wide area. For example, with elliptical laser beam FWHM 0.69 mm x 1.35 mm, suppose we collect 1cm x 1cm square at a time, it will cost 784 seconds to scan a 7cm x 7cm area. When the suspicious area expands, the time spent will increase rapidly, which restricts the application of FDTI.

In addition, in previous experiments we have observed the effect of motion on the system. We can solve the problem by setting a threshold to filter out data that does not meet the requirements. But in order to save time while ensuring accuracy, we need more robust collection methods, and correct the motion effect on the system and results.

The advantages of thermal imaging include non-invasive, functional imaging, as well as the relative portability of the imaging system. In previous experiments, we used a portable, low-power pencil laser instead of a large laser to reduce system complexity and improve portability. But there is still room for optimization on other hardware.

3.3 Hardware Optimizations

First, we analyzed the size of FDTI hot spot. **Figure 3. 1** (a) shows an example of the hot spot after laser turned on for 10s in FDTI experiment. The temperature rise threshold is set to 0.05^{o}C based on the sensitivity of common infrared cameras. By converting pixels to physical distances, we found the top and bottom diameter of the laser hot spot is 3.5 ±0.2mm, and the left and right diameter is 4.2 ±0.2mm. This difference is because the laser beam is elliptical.

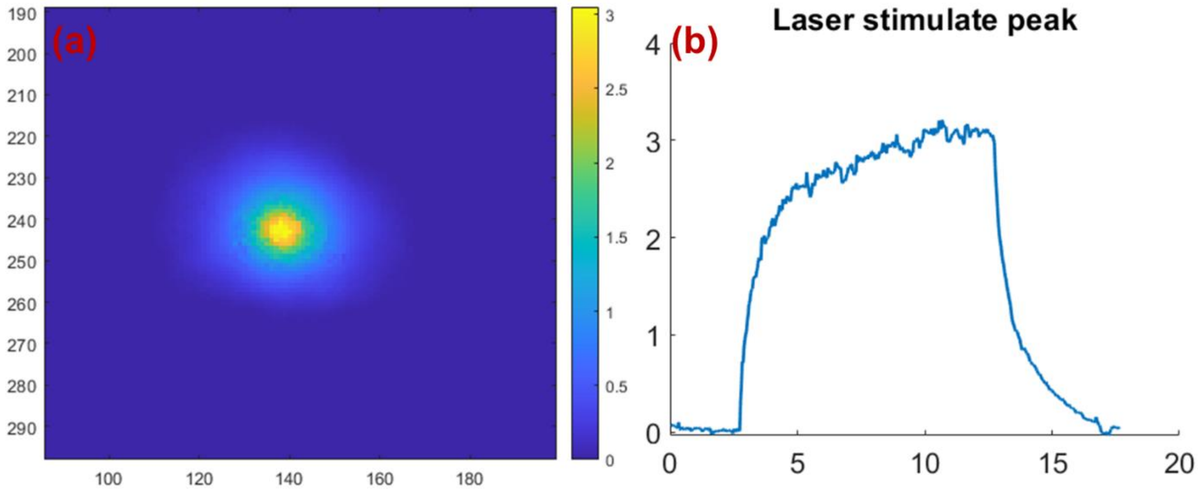

Figure 3. 1. (a) An example of hot spot generated by laser. Laser had been turned on for 10s.

Based on that, if we can generate multiple non-overlapping hot spots at the same time, it is possible to collect multiple points in one video. We can use beam splitter to achieve simultaneous excitation of multiple lasers, or use a matrix composed of multiple laser diodes. The distance of laser beams should larger than the hot spot diameter. Similarly, we can also use a single beam of laser plus an automatic scanning system, which can save the process of adjusting the target position during acquisition. Systems sketch are shown in Figure 3. 2.

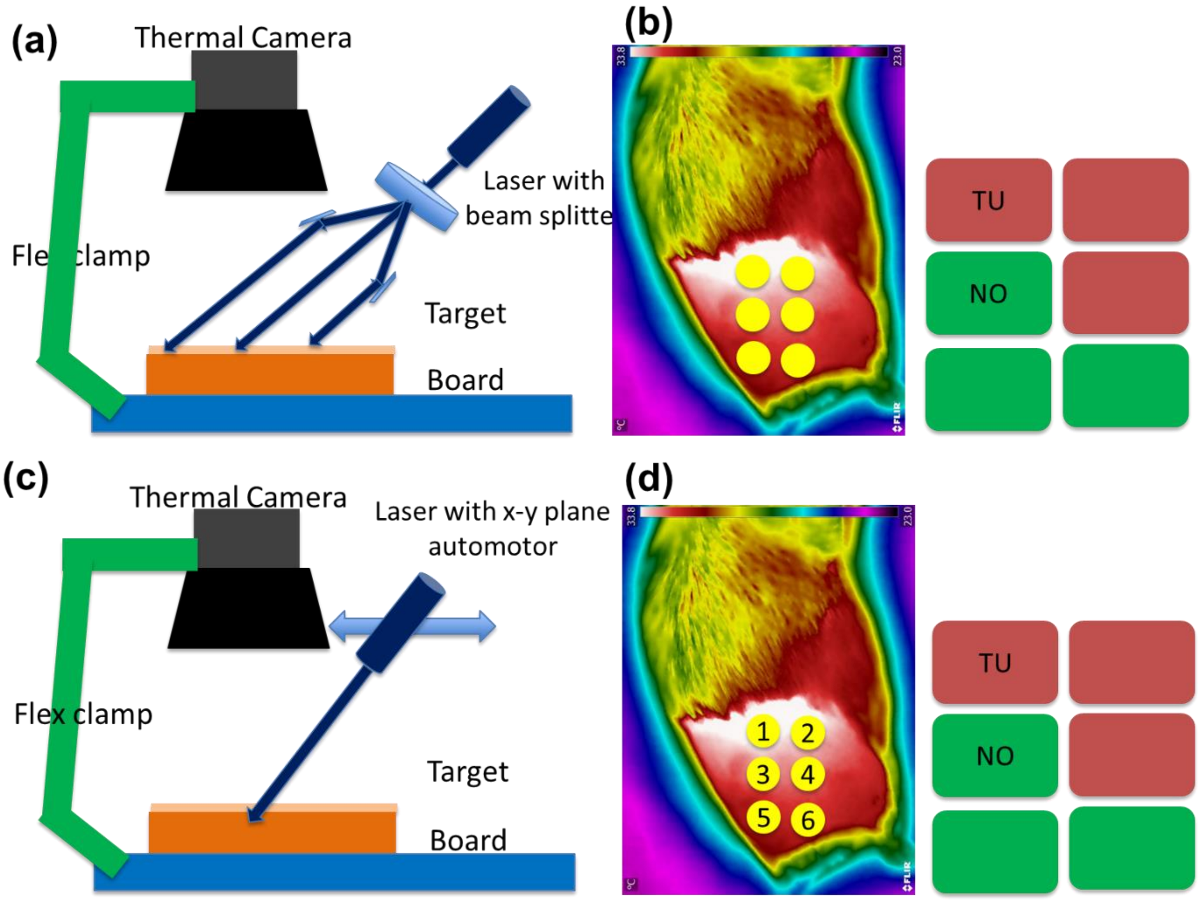

Figure 3. 2 Optimized FDTI for collecting multiple points. (a) FDTI system with beam splitter. (b) Schematic diagram of images collected by the system in (a) and the output results. (c) FDTI system with scanning auto motor in x-y plane. (d) Schematic diagram of images and results from the system in (d).

3.4 Feature optimizations

3.4.1 Background

To improve the system to save data collection time, besides hardware update, another way is to reduce the acquisition time. We can divide the acquisition process into four time periods: steady state (laser off), rising stage (laser on), steady state (laser on) and recovering stage (laser off). The end of the rising stage is taken as: the temperature reaches 85% of the temperature at the end of the steady state with laser on. The threshold is selected based on the feature stability analysis in Chapter 2. Features produced at different stages may have unequal effects in the final result.

An example of the peak change curve during the acquisition process is shown in the Figure 3. 1 (b). Lengths of the processes shown in Figure 3. 2 (b) are: 2.73 second for steady state, 2.63s for rising state, 7.21 s for steady state (with stimulation), and 5.07s for recovering stage. The time length from the temperature rising point to the temperature declining point is 9.84s, near the preset value 10s; the recovering stage length is 5.07s, near the preset value 5s. Both of them meet the expectations of the experimental design. There is an offset of the starting point in the figure: the steady state exceeds the preset value 1s. This offset was corrected by minus 1.7 seconds at the beginning (about 50 frames). Since the features used in the previous analysis (Chapter 1 and 2) are all extracted after the laser is turned on, this offset does not affect the previous results.

From the figure, we can observe that the heating process only accounts for a small part of the acquisition process. If we can use the features of a certain stage to achieve an acceptable accuracy rate, we can effectively shorten the acquisition time.

3.4.2 Methods

We extracted the data of the rising part and analyzed the features generated by the rise and decay parts. For rise part, the 3 second to 5.3 second part of each video was separated as dataset, for decay part, video between 12.7 and 15.7s was separated. Thermal images were extracted from videos for analysis. The ROI selection and feature extraction parts were the same with previous chapters. The mouse tumor model continues to use the previous early detect data set.

Statistical analysis was performed using MATLAB R2018a. The training set, test set, 5-fold cross-validation and ROC curve settings are the same as the previous chapters.

3.4.3 Results and discussion

ROC curves of rising and decay part are shown in Figure 3. 3 and Figure 3. 4.

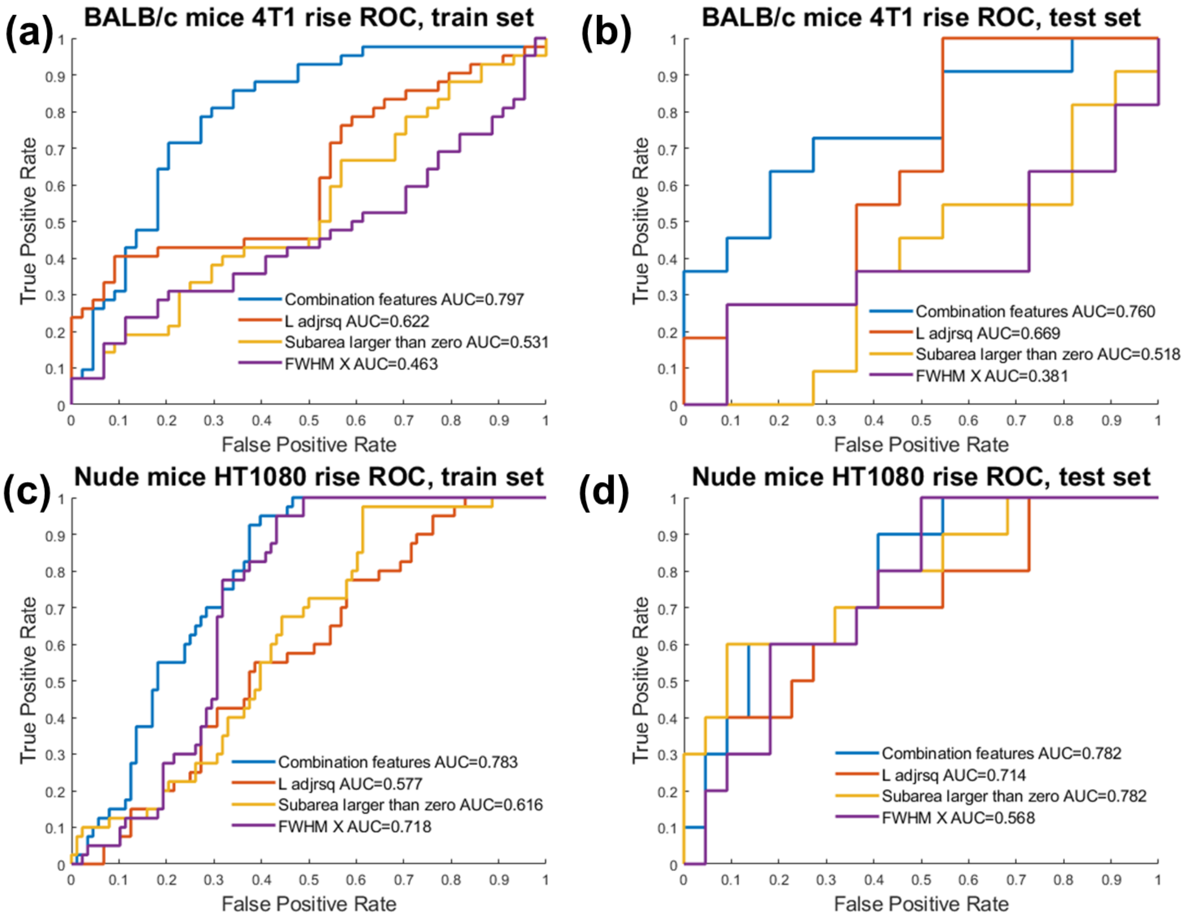

Figure 3. 3. The ROC curve of the feature classifier in the rising part of FDTI. (a) BALB/c mice, 4T1 tumor, train set. (b) BALB/c mice, 4T1 tumor, test set. (c) Nude mice, HT1080 tumor, train set. (d) Test set of (c). 5-fold cross validation was used in separating train and test set.

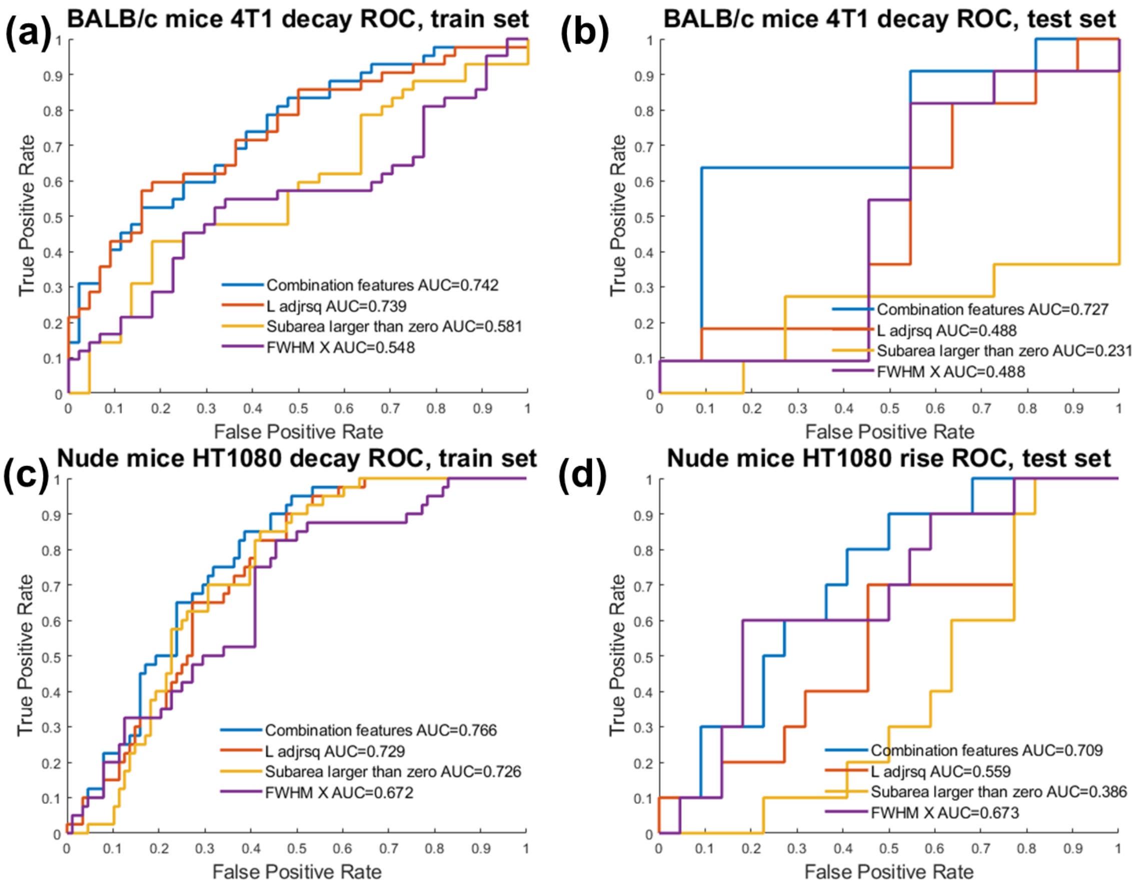

Figure 3. 4. The ROC curve of the feature classifier in the decay part of FDTI. (a) BALB/c mice, 4T1 tumor, train set. (b) BALB/c mice, 4T1 tumor, test set. (c) Nude mice, HT1080 tumor, train set. (d) Test set of (c). 5-fold cross validation was used in separating train and test set.

Figure 3. 3 shows the result of rise data analysis in both BALB/c and nude mouse tumor model. For train sets, 3-feature classifier accuracy is lower than 0.80, and test sets are lower. Figure 3. 4 shows the decay part was the same.

The accuracy is lower than the previous results. But in this experiment, we continue to use the previous data analysis parameters, and export 3 frames of images per second. For a 16-second video, this is enough to generate a set with 48 thermal images for analysis, but for the rising and falling interval of 2 to 3 seconds, this data set seems a bit small. If we export 10 images per second, the effect should be different.

In addition, here we use the data set for early tumor detection. Considering that the early stage tumor in this experiment is invisible to the naked eye and traditional thermal imaging, the accuracy rate will inevitably be low. For each point, the rising part ascending and descending segments are analyzed separately, which also causes a decrease in accuracy. Furthermore, here we completely exclude the steady-state period (7.21s, about 50% of the collection time). If we keep only some of them, the accuracy rate should increase. In addition, we are currently using continuous lasers. If pulsed lasers are used, different results may be obtained.

As conclusion, there is room for time optimization in the process of tumor data collection. Based on the test on rising and decay period, as the acquisition time decreases, the accuracy of FDTI will decrease. How to shorten the acquisition time depends on the threshold of the accuracy.

3.5 Build a robust and highly automated system

3.5.1 Background

In the early tumor detection experiment, the Bioluminescence (BLI) image and the thermal image need to be registered, but the thermal image can provide too few features, so the color image has to be introduced as the registration reference.

However, the resolution of the thermal image was lower than BLI, the field of view (FOV) of thermal was smaller, and the thermal image provided only temperature information. Some objects with large differences in color images may have the same value under thermal imaging, which makes it difficult to detect the difference. This makes many feature extraction methods based on conventional gray images, such as edge detection, corner point detection, and covariance matching, no longer work. An example is shown in **Figure 3. 5**.

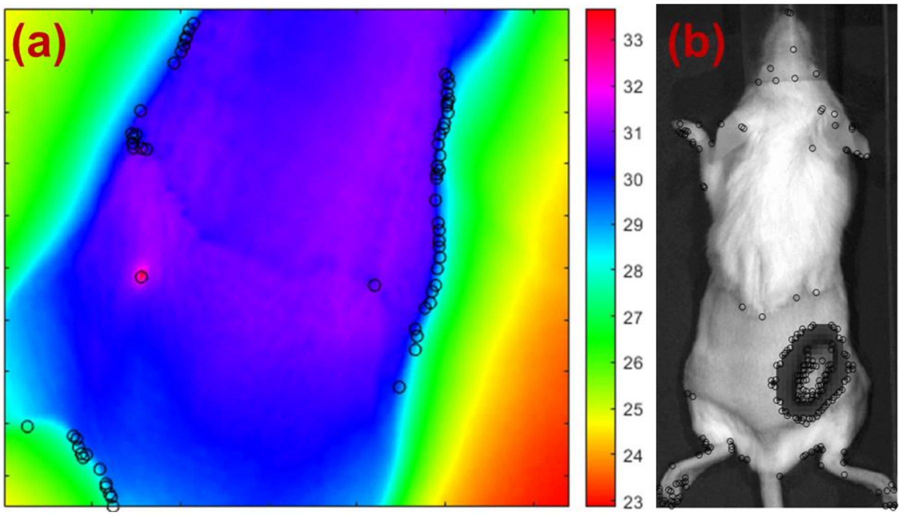

Figure 3. 5 Example of corner point detect in thermal image and BLI. (a) Corner point detect in thermal image. (b) Corner point detect in BLI figure. The detected Harris corners are shown in black circles

Due to FDTI and BLI use different backgrounds, ideally, most of the feature points for registration should on the mouse body. But as the example in Figure 3. 5 (a) shows, the corner detect results are mainly on the border of mouse and background. At the same time, the laser signal also has an impact, this can be eliminated by using steady state image. But for BLI, the system output image is a superimposed image of a color and fluorescent signal. Similar issues also happen to other features, such as border detect and matching, and speeded up robust features (SURF). For these reasons, there are few matching points to match between thermal image and BLI. Besides, the field of view (FOV) of the BLI image is larger than that of the thermal image. Even after the block calculation, the matching effect of the covariance matrix is not good.

For these reasons, we need to introduce color images as registration benchmarks, and add markers in the experiment.

3.5.2 Marker selection and test

For the mouse experiment, we added small markers to meet the demand. A set of schematic diagrams has been shown in **错误!未找到引用源。**. In that experiment, manual selection of registration points worked best. After that, in order to improve the robustness of the system and the ability of automatic acquisition and processing, we try to use a reusable marker with a regular shape and let the system automatically find the registration point.

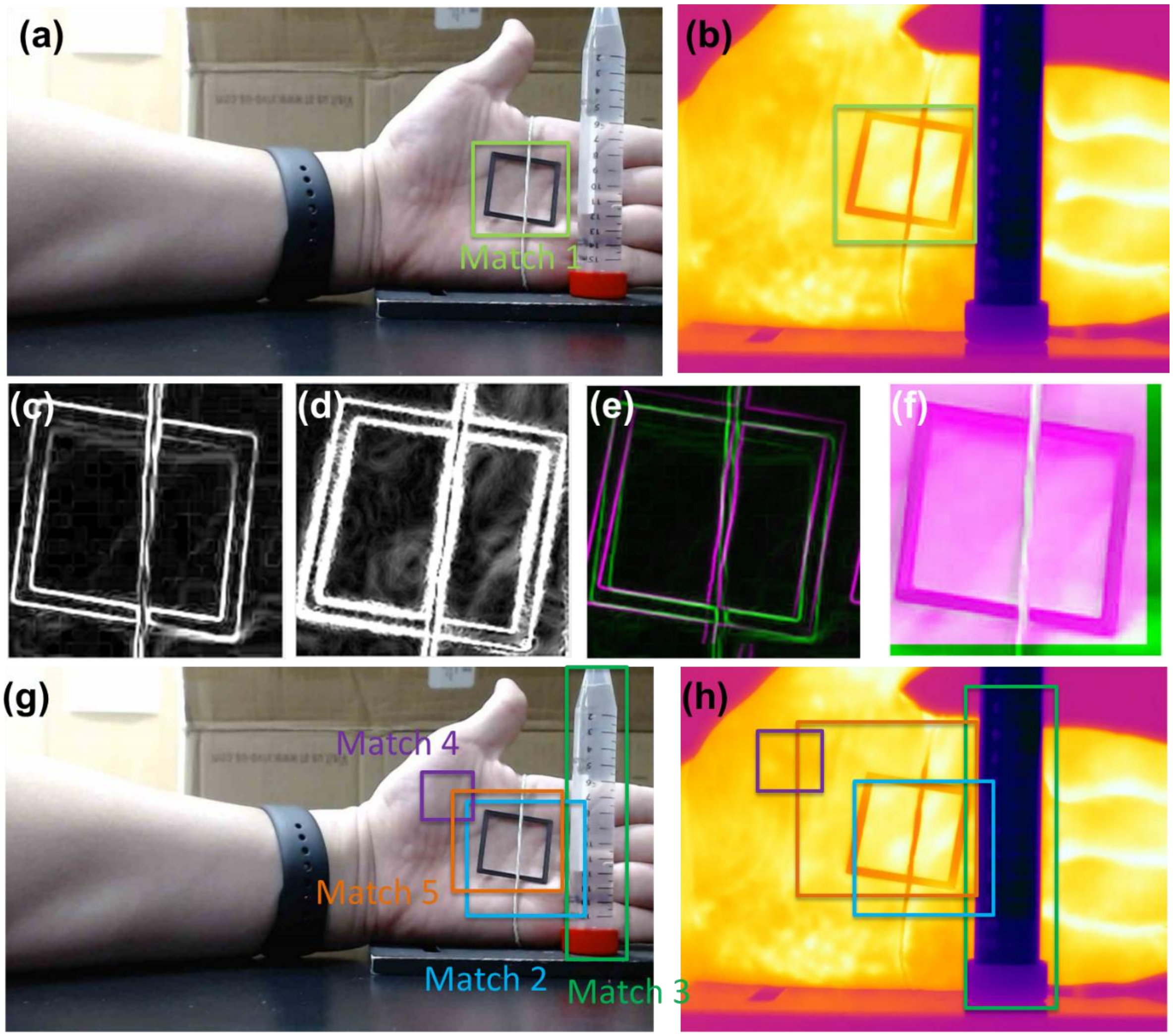

Figure 3. 6 Example of single marker registration test. (a) Color image. The green box is the manually selected registration area (registration ROI). (b) Steady state thermal image of system. (c) The image after gradient extraction of ROI in (a). (d) The image after gradient extraction of ROI in (b). (e) Overlap image of (c) and (d) (f) The registered image of ROI in (a) and (b). (g) Test the registration in multiple cases, rectangles of different colors represent ROI in different situations. Match 2: The marker is not completely contained in one image, here is thermal image. Match 3: Other types of markers. Match 4: Marker is not in ROI. Match 5: ROI size is not equal.

We used 3D printer to make a 40mm x 40mm x 2mm polylactic acid (PLA) rectangle marker. The border of the marker was 2mm wide. The marker appeared as a shadow under thermal imaging. The color image was captured with Logitech C920 webcam. Based on this marker, we conducted a series of tests on the registration method. First, we fix marker on target, capture color and thermal images, then manually select ROI for registration in them. Then we use corner registration, SURF features, covariance matrix, edge detection and gradient extraction to extract registration features, and test the performance. After that, we changed the ROI to simulate four different situations to test the robustness of the current method. Then, we changed the position and posture of the target, and repeated the above process. A total of 3 groups of different positions and postures were tested on the target, each group contained 10 pictures. Manual evaluation is used to evaluate the registration results, which are divided into good, fair, and poor. The registration method that gets the most "good" results is considered the best.

Figure 3. 6 shows an example of test. Sub figure (a)(b) show the color image and thermal image, and the selection of the registered ROI. Sub figure (c) to (f) present the registration results of a set of features (gradient extraction).

Figure 3. 6 (g) and (h) show the simulation of ROI under different situations. Matching 2 simulates the case where the marker is not completely covered due to cameras have different FOV. Matching 3 simulates the situation where there are other interfering targets ahead. Matching 4 simulates the situation where the marker is not detected and causes the ROI to shift. Matching 5 simulates the situation where sizes of ROIs are different. The results of multiple situation simulation experiment are shown in Table 3. 1. It shows three main factors that need to be considered for the registration: whether the ROI size is the same, whether the MARKER is in both FOV, and whether the two ROIs has a large overlap.

Table 3. 1 Registration method test results

Match \ ROI	Same size	Marker in FOV	Large overlap	Good results
Matching 1	Y	Y	Y	28/30 (Gradient)
Matching 2	Y	Y for color, part for thermal	N	23/30 (Gradient)
Matching 3	Y	N	Y	X [1]
Matching 4	Y	N	N	X
Matching 5	N	Y	Y	25/30 (Gradient)

[1] "X" represents there are less than 5 good images in all methods.

Among the three groups of images, the gradient registration method performed the best. This may be related to the characteristics of the marker and the image. In experiments, we found that the border detect method will detect too many edges (with canny operator), and it is necessary to manually adjust the detection threshold. The corner detection method has fewer features in the ROI compared with gradient, and it does not perform well in matching 2. The SURF method encountered problems in matching the features of the two images, SURF features on thermal images are few compared with color images.

Discussion

Gradient map performs best in the comparison of the registration methods. This is related to the characteristics of the marker. The thermal image only displays temperature information. Therefore, in order to improve the contrast with the background and facilitate system identification, the marker should appear as a bright or dark area on the thermal image. This facilitates the generation of gradient features. If we use different materials to make the marker, or add different shapes to the marker, the gradient features will be richer and we can distinguish the direction of the marker.

Generally, the registration effect should be measured by numerical values, such as root mean square error (RMSE). But in the experiment, for some groups (such as matching 4), the registration results are very bad, the matched image have almost no overlapping parts with one of origin image, which makes the numerical indicators lost their meaning. Moreover, in some groups, one algorithm got a poorer effect on key target registration (the marker), but it obtained a lower RMSE because it had a better registration on another part. Due to this, we decided to use the score as a judgment indicator.

In the test results, the priority of the marker is higher than the overlap of the ROI area. This is because most features used in registration comes from the marker. When the marker is fully included, the impact of ROIs of different sizes is relatively small. This is applicable to all the tested features, the reason is that the tested features can be matched by scale transformation.

Therefore, in further research, the primary goal should be to detect markers. The ROI size can be appropriately larger to increase the overlap rate of the ROI in the two images, that can improve the registration accuracy.

3.5.3 Marker detection

Based on the rectangular marker in the previous part, we added letters and patterns to the marker for the camera to recognize. We used a 3D printer to print a 40mm x 40mm x 2mm black PLA marker with the letters "ORL" and a rectangle area. The width of the border is 2mm, the heights of the three letters are 10mm. The distance between the upper edge and the letters is 2mm. The distance between the upper edge of the rectangle area and the letters is the same. The marker was affixed to the target, the thermal camera (FLIR T650SC) and the color camera (Logitech, C920 webcam) were fixed on the table. Thermal and color images of the target were taken and processed with MATLAB script on a laptop.

For thermal images and color images, gradient feature maps were generated. Then elementary pattern recognition technologies (such as circle and rectangle recognition) were applied on the maps. Optical character recognition (OCR) was also used.

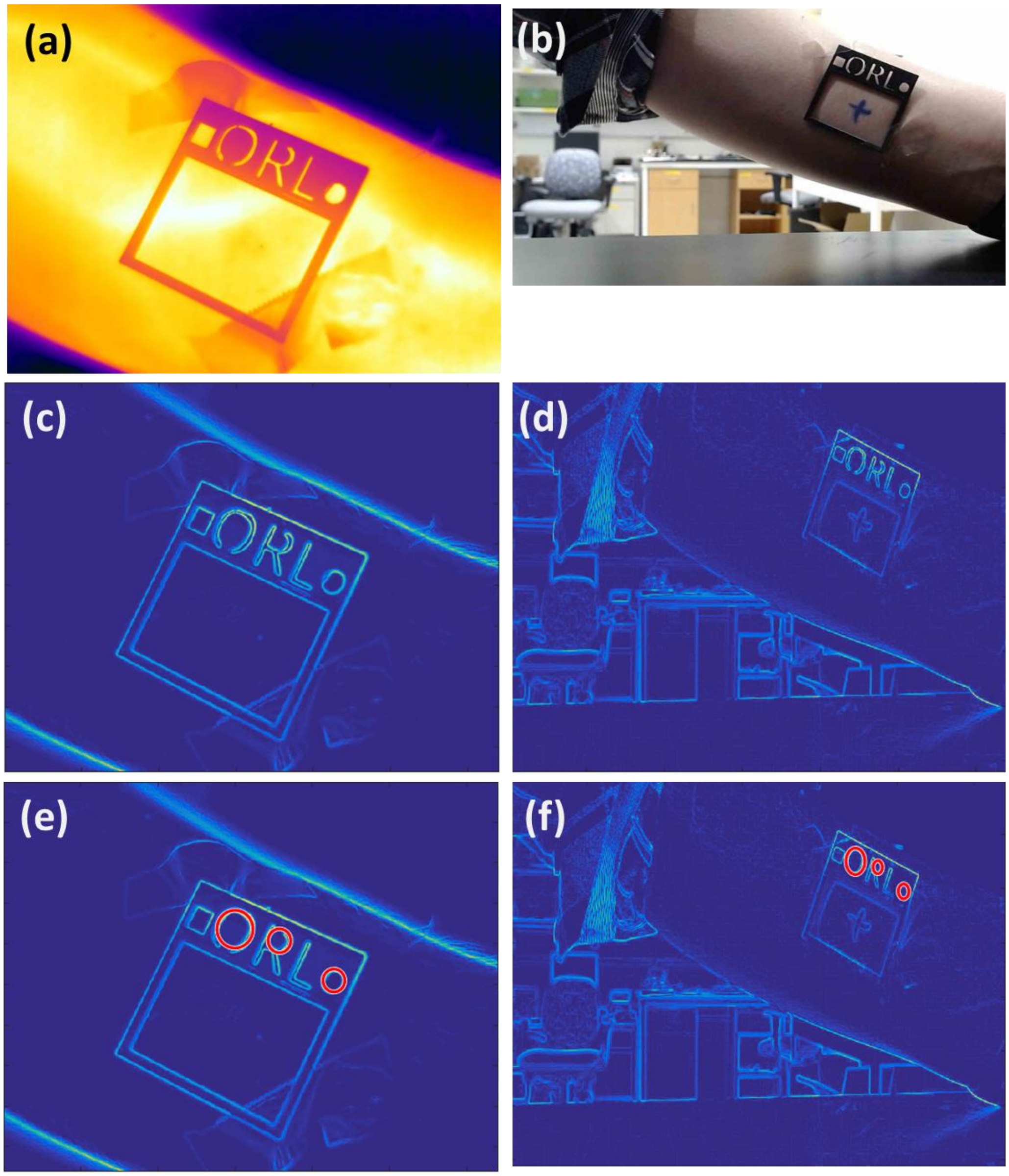

Figure 3. 7 (a) Thermal image of target with marker. (b) Color image of target with marker. (c) The gradient feature map of (a), (d) The gradient feature map of (b). (e) Pattern matching example, the result of circle recognition in (c). (f) The result of circle recognition in (d)

A set of recognition and matching results on this marker are shown in Figure 3. 7. The gradient feature obtained in the previous experiment is used. Among the matching of several shapes and letters, the result of round matching performs the best. An example is shown in subfigure (e) and (f). The three circles in the picture are matched in pairs.

Furthermore, the data collection environment may not always ideal. In the clinical or other environment, there could exist interference, for example, the background of thermal imaging or color image may be complicated, so there may exist a pattern similar to the marker. Or, the illumination of the environment may affect the gradient information, for example: too dark, too bright, or large shadows.

To test the system's stability with complex environments, we conducted further tests. We used the same method, and chose the same parameters as the previous experiment. In the first set of tests, we placed debris in the background, such as a box printed with letters, a rectangular similar in size to the marker, or a round marble with a diameter of about 1cm. This is to simulate a complex imaging background to test the performance of the system. In the second set of tests, we tilted the target in different directions to create a shadow that would cover the letters. This is to simulate the situation where the color camera imaging is affected by uneven illumination, in order to test the performance of the system.

Figure 3. 8 shows the test results of anti-interference ability of the system under these two conditions.

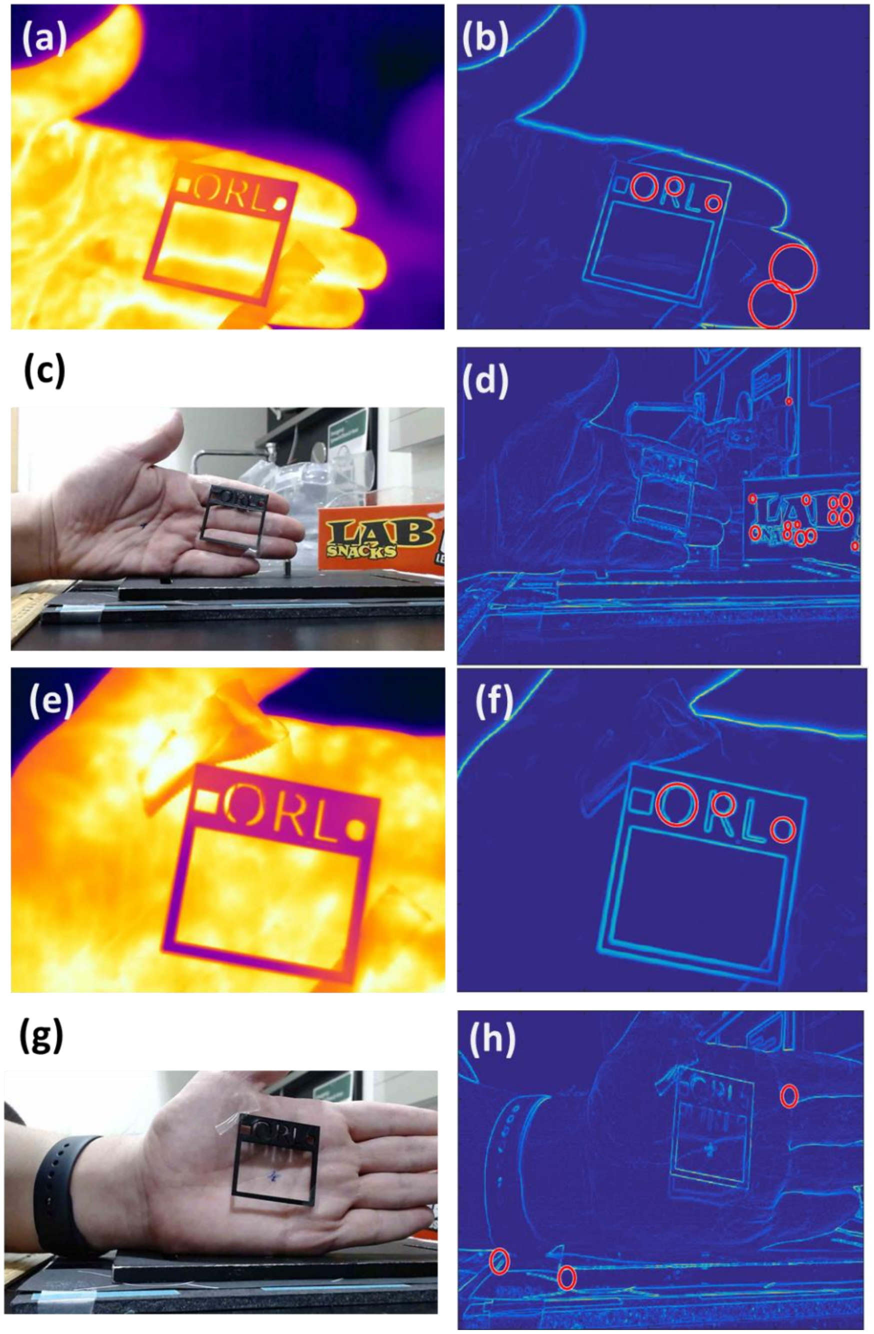

Figure 3. 8 Testing the matching results under interference. (a) Thermal image with marker. (b) Gradient map of (a), with circle recognition. (c) Color image with marker related to (a), contains a complex background. (d) Gradient map of(c), with circle recognition. (e) Thermal image with marker. (f) Gradient map of (e), with circle recognition. (g) Color image with marker related to (e), contains shadows that obscure the letters. (h) Gradient map of (g), with circle recognition

Results of the first test are shown in Figure 3. 8 (a)~(d), the second in Figure 3. 8 (e)~(h). In these tests, the circle detection method gave poor results. In the first group, when there is a complex background, the system finds more circles in the background than in the target area. This is because there is no manual selection of the ROI area in this part (We hope that the system can automatically detect the marker). In the second group, when there were shadows covering the recognition letters, they affected the gradient map performance, that lead to the fail for system to recognize the target.

Discussion

In the first part of pattern recognition, OCR performed unexpected poor. It cannot find letters, and cannot find ROI. We tried to adjust parameters for the algorithm and the OCR software, but it does not work. We also tried image pre-processing for OCR, it also does not work. This includes mature commercial OCR software. The reason may be that the common OCR function and software are trained and designed for pdf files and photos of books. They works well when working on recognize a large number of densely arranged small texts, but are not adapted to the situation in the experiment.

When the background was clean and the illumination was uniform, the circle recognition performed good. But when a similar pattern appeared in the background, or the gradient map was affected by the light, the result became worse.

This means that we should pay attention to the environmental background and illumination when collecting data in the experiment. And, we should choose more complex and less common templates for pattern matching. Knowledge in the field of template matching can help us to reach this goal. The article represented by [1] outlines the application of thermal imaging and also contains knowledge of template matching, same as [2-5]. We have made several markers with more complex shapes, such as Figure 3. 9, in subsequent studies, they will be tested for matching effects.

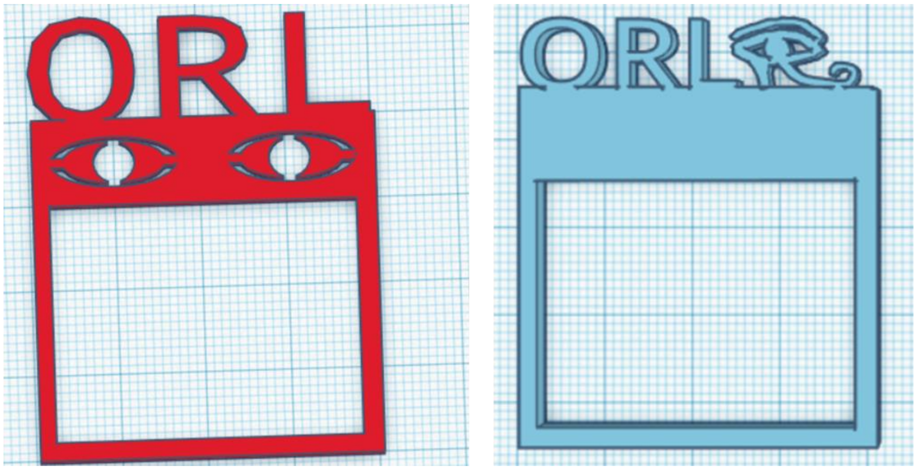

Figure 3. 9 Some examples of markers going to be tested in template matching.

Another feasible way is to perform background filtering. The method eliminates background interference by filtering with specific signals such as color. This method is suitable for color images with complex backgrounds. In the test, the subject sits in front of the color camera, a face detection algorithm is used for detecting the subject's face. Then a ROI is selected as the color filter benchmark. The parts in the background that are similar in color to the ROI area will left after filtering. Then we can adjust the previous method or perform template matching. A group of background filtering examples are shown in **Figure 3. 10**.

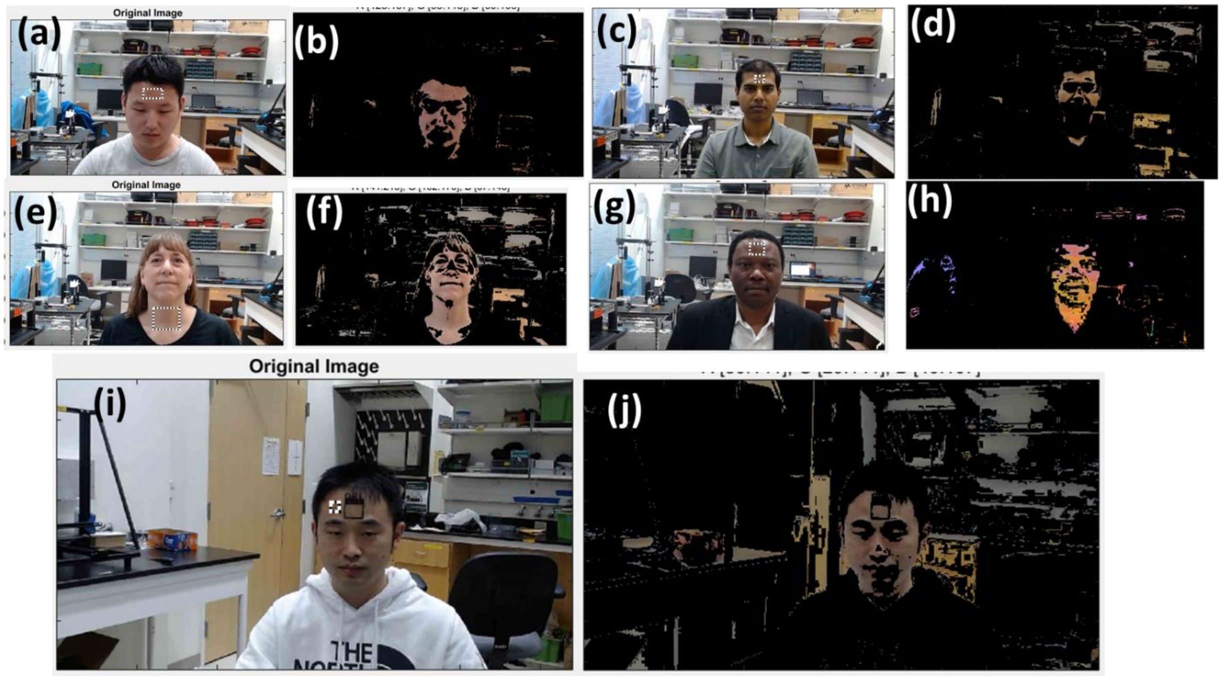

Figure 3. 10: Background filtering by face detection and color filter. (a) Color image before filtering. After the face is detected, the skin of the subject's forehead is selected as the color filter benchmark. (b) Image after using color filter on (a). (c)(d), (e)(f), (g)(h): Repeat the test on subjects with different skin colors. (i)(j) Test complex background color images with the marker

The test has shown that background filtering can remove most irrelevant signals in the complex background. From (a) to (h), the test shows the method suits for people with different skin colors. Sub figure (i) and (j) shows the filter result with the printed marker. During the filtering process, the marker is retained. This facilitates the use of thermal images and previous methods for further registration. Here, the ROI area of the face detection is not used to crop the image, because in actual situations, we may not image human face.

Besides, in the experiment, the target showed obvious movement, due to the time gap between the color image and the thermal imaging collection, which increased the difficulty of pattern matching. In the following sections, we will discuss the issue of motion correction.

3.5.4 Motion correction

In previous mouse experiments, breathing effect had affected the stimulation position of laser spot. To solve that problem, we sampled the same point multiple times, analyzed and compared features, estimated the fluctuation value of the feature, and solved this problem by setting a threshold to filter the data. In the clinical environment, due to time constraints, it is difficult for us to repeatedly sample a certain point and do feature analysis of the patient. At the same time, we hope to optimize the acquisition time of the system. Therefore, we need to introduce motion correction to improve the quality of the data and reduce the waste of data. At the same time, high-quality data is conducive to getting more accurate results.

In the experiment, we attached the marker to the target, and then performed FDTI acquisition, and record thermal video of the process. We applied border detect and generated gradient images of the collected data, and register each frame of the image according to the movement of the marker. Results are shown in Figure 3. 11. To improve the accuracy of motion calibration, local interpolation was applied on the feature map to achieve sub-pixel level registration. In subfigure (a), FDTI system was used on subject’s skin to collect video, the red dots and green dots showed the relative laser spot position with and without motion correction. An example of motion effect can be observed in superimposed subfigure (b), and the motion is corrected in (c), the border map showed in (d) demonstrated the effect of motion correction. In the figure, the motion correction shows good results.

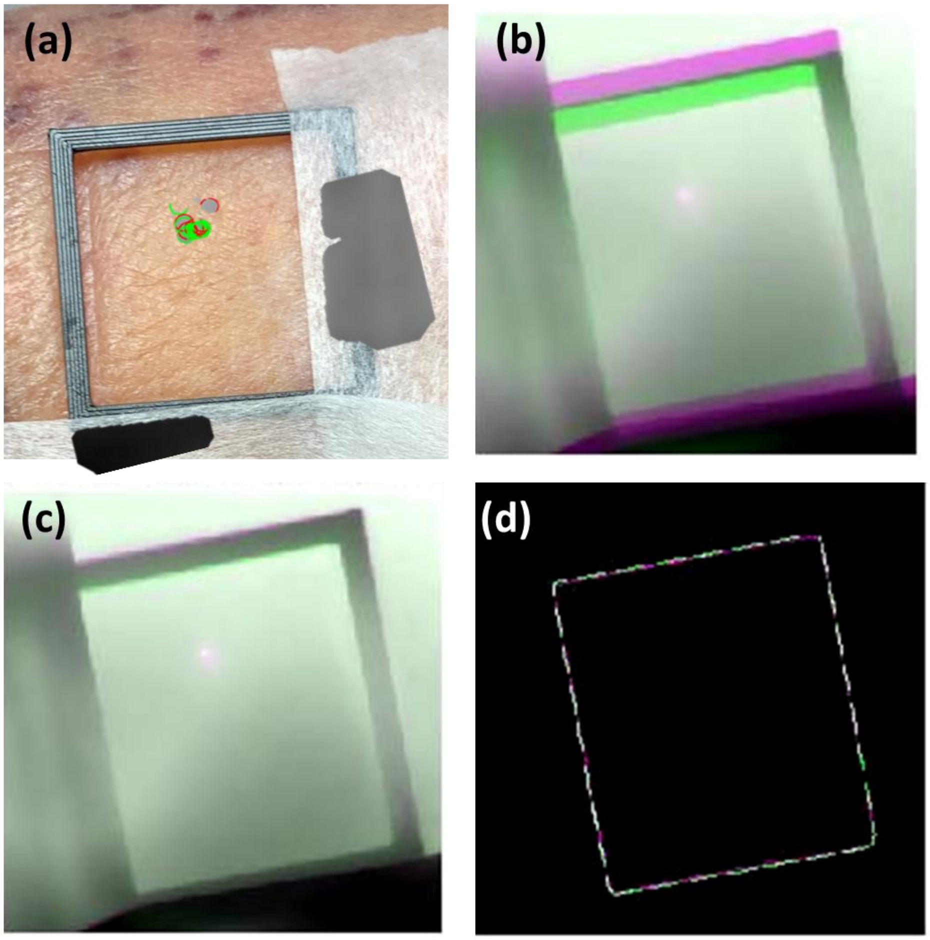

Figure 3. 11. Motion correction result on human. (a) Color image with the marker, red dots are positions of laser spot before motion correction, green dots are positions after correction. (b) The superimpose image of 0s and 7s, without motion correction. (c) Superimpose image of 0s and 7s with motion correction. (d) The superimpose image of the edge of the images on 0s and 7s with motion correction.

3.5.5 Discussion

In the experiment, we verified the necessity of motion correction and the effect of motion correction based on gradient features.

Based on that, we can change the style of the marker so that the system can automatically find and recognize the marker, and then automatically apply the motion correction to the target. This helps to enhance the robustness and applicability of the system.

In order to verify the effectiveness of this system, we will collect more data and look forward to user feedback.

However, the imaging system still has some shortcomings. Compared with color images, the depth of field of thermal imaging is smaller. This makes the registration accuracy drop when imaging a non-planar surface (such as mouse dorsal). We tried to segment the image by region and register, but this step still needs to manually select the area. At the same time, the blur caused by out-of-focus thermal imaging cannot be avoided.

It seems that this problem cannot be solved from the perspective of software alone, because the parameters of the thermal imaging camera used in the experiment are difficult to adjust. A more feasible solution is to change the hardware design. A possible design is described in Figure 3. 12.

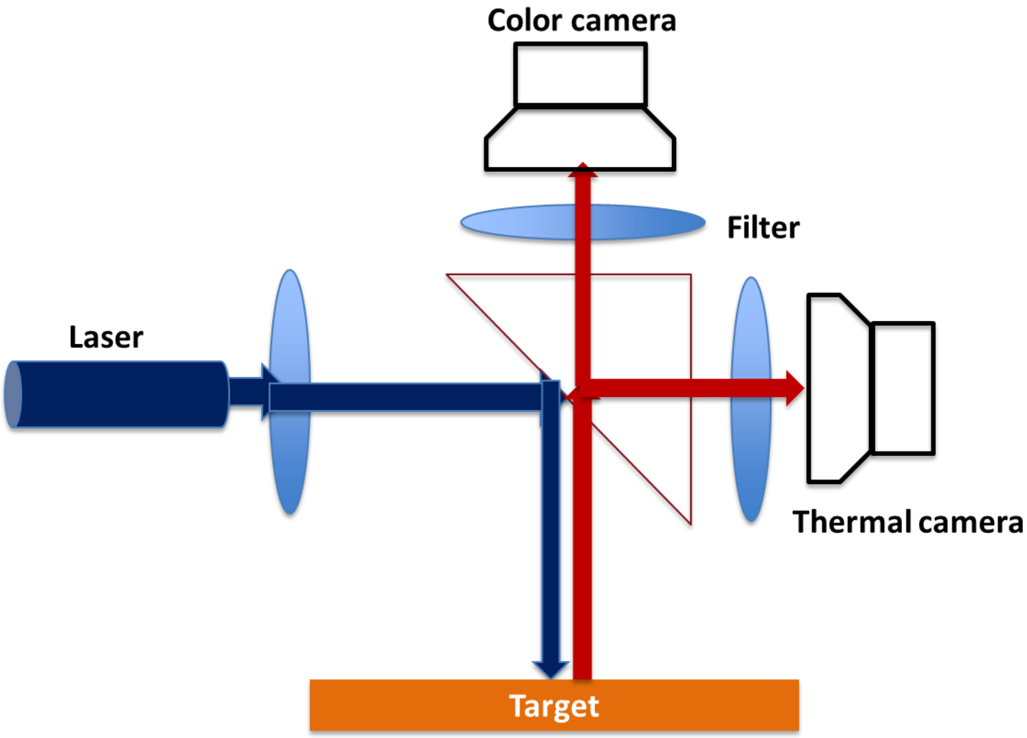

Figure 3. 12 Sketch of improved imaging system. The system includes lasers, small color and infrared cameras. The signal is separated by a half mirror and a filter.

In the design of the figure, the infrared camera and the color camera are at right angles to each other to capture signals. The cameras can collect images and videos with the same FOV and depth of field. At the same time, color cameras and infrared cameras can be replaced by small camera modules, which reduce costs of the system.

For the system shown in the figure, Indium tin oxide (ITO) film can reflect infrared light and transmit visible light at the same time, which may be a suitable material for the half-mirror. This material is mostly used in the field of solar energy. It seems that it can also be applied to infrared imaging.

In addition, in order to quickly generate hot spots, we chose a 405nm laser for thermal imaging. But the penetrating ability of this wavelength laser is shallow, usually 2~3 mm. The penetration ability of 780nm laser is stronger, but the thermal effect is relatively weak. The system can test lasers of different wavelengths to select equipment suitable for imaging tumors of different depths.

The system has the potential for optimization in multiple directions, and need further research.

Reference

1. Gade, R. and T.B. Moeslund, *Thermal cameras and applications: a survey.* Machine Vision and Applications, 2014. **25**(1): p. 245-262.
2. Kopaczka, M., J. Nestler, and D. Merhof. *Face detection in thermal infrared images: A comparison of algorithm-and machine-learning-based approaches*. Springer.
3. Ribeiro, R.F., J.M. Fernandes, and A.J.R. Neves, *Face detection on infrared thermal image.* SIGNAL 2017 Editors, 2017: p. 45.
4. Chen, C., et al., *Image stitching and partitioning algorithms for infrared thermal human-body images.* Opto-Electronic Engineering, 2019. **46**(9): p. 180689-1-180689-9.
5. Lamberti, F., et al., *Intensity variation function and template matching-based pedestrian tracking in infrared imagery with occlusion detection and recovery.* Optical Engineering, 2015. **54**(3): p. 033106.

Chapter 4: Application of thermal imaging on human

4.1 Abstract

This part tests the thermal imaging system's ability to detect brain tumors, nerve damage and other diseases. It also contains some relevant hypothetical tests during the COVID-19 epidemic. The collaborators in this section include Kalen Dionne, Christopher Malone, Bhuvic Patel, and Leo Shmuylovich. I wrote the chapter, designed and conducted the experiments with collaborators, analyzed the data, and participated in the design of the new GUI.

4.2 Observing brain and nerves activity with thermal imaging

4.2.1 Background

The study of the brain has long been a hot spot in scientific research. Through brain imaging, researchers can establish correlations between various diseases and brain changes. For example, researchers use brain imaging to study catatonia [1], in the COVID-19 pandemic, researchers also observe the brain changes of patients [2]. Psychologists also use brain imaging to study the relationship between mental illness and brain changes [3, 4]. In these studies, researchers use a variety of non-invasive brain imaging tools, including magnetic resonance imaging (MRI), positron emission tomography (PET)/X-ray computed tomography (CT), and the second near-infrared (NIR-II) region of wavelength. These studies involve physiological indicators of the brain and nerves, and the temperature of brain and nerve tissue is related to a variety of physiological parameters [5], and it will affect some signals, such as BOLD signal of fMRI used for brain tumor[6-8] and external stimuli [9-11]. Our target is to investigate the effects of changes in physiological characteristics on thermal imaging, such as brain tumor, nerve damage, and stroke.

4.2.2 Materials and methods

All animal work was approved and performed under an approved protocol by Washington University's Institutional Animal Care and Use Committee (IACUC).

The brain tumor part is a correlation research of article [12] to model human brain tumor therapy. Mouse model was performed on immunocompromised mouse with Glioblastoma. 50,000 GL261 cells were injected to 7 weeks old C57BL/6J mouse (n=5) in 3 uL of PBS through drilled hole in mouse skull. Mouse bregma was set as the origin (x,y,z = 0,0,0) to establish a left-hand coordinate system. Tumor was planted at x=1.5mm, y=0.98mm, z=2mm from origin point, sketch shown in Figure 4. 1 (a). The therapy laser system is Dornier Medilas Fibertom 8100 , laser wavelength is 1064 nm with 2W power, it is irradiated to the lesion through a probe. Two thermocouples are installed near the probe (core) and 1mm away from probe (Penumbra) to record temperature change. A thermal camera (FLIR T650sc) was installed above the experimental device to record surface temperature changes. Laser ablation was performed 7 days after tumor injection. For the control group (n=5), the system setting is the same as the setting for tumor group except for the tumor cells.

Nerve damage rodent model was performed on Wistar rats (n=2). The healthy rat was operated to expose nerves of legs, the right side nerve was clamped with a hemostatic forceps for 1 minute, and then the hemostatic forceps were removed. Then nerves on both sides were observed with thermal camera (FLIR T650SC) after 3 minutes of recovery. Then they were washed with PBS.

If nerve damage can be observed on the surface of the skin with an infrared camera, that would be ideal. Stroke is one of the most serious nerve damages. Based on this, we tested a mouse stroke model (n=2) and tested the effects of thermal imaging in healthy volunteers that simulate a stroke.

4.2.3 Results and discussion

This part includes the respective results and discussions of brain tumor experiment and nerve injury experiment.

Brain tumor

Brain tumor laser therapy results are shown in Figure 4. 1. Sub figure (a) shows the sketch of tumor cell injection position. (b) is thermal camera view before laser turned on. During the therapy, bright heat signals can be captured in the tumor area, (c) is the temperature change recorded of tumor core and penumbra during experiment. The experiment simulates the human brain tumor laser therapy. During therapy stage, glioblastoma tended to fluctuate more compared with normal tissue.

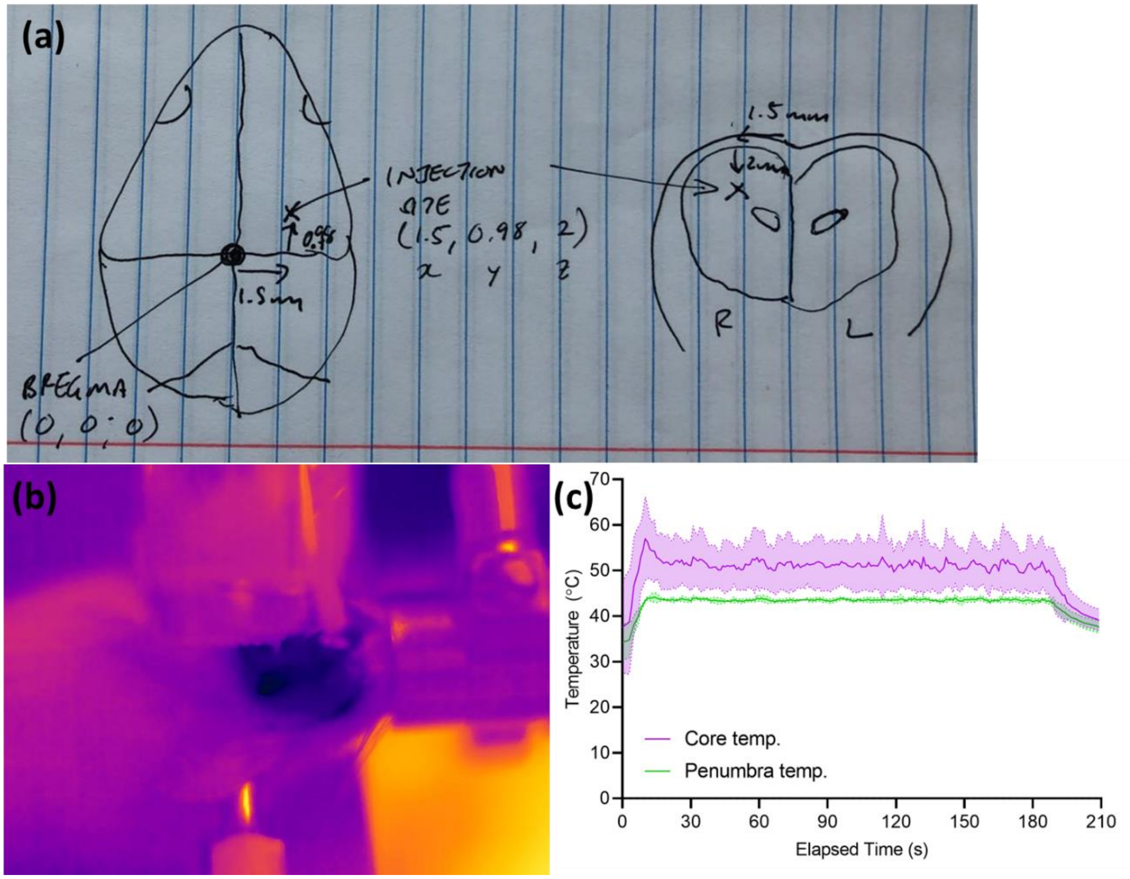

Figure 4. 1 (a) sketch of brain tumor planted in mouse. (b) Thermal camera view of the laser therapy. (c) Temperature change during laser therapy of tumor core and penumbra 1mm anterior to the laser center. Solid line: mean value. Shade: standard deviation. (c) is the same as Supplementary_Figure_1 in [12].

Nerve damage

The results of rat nerve damage are shown in Figure 4. 2. (a) and (c) show the thermal image of the injured side of the nerve. The shadow of the nerve bundle can be observed in the figure. The average temperature of this area is 32.08~32.36°C, which is 0.3~0.7°C lower than the surrounding tissue temperature. (b) and (d) show the contralateral side. The nerve bundle is not obvious in thermal image, its average temperature is 32.30°C to 32.83°C, which cannot be distinguished from surrounding tissue.

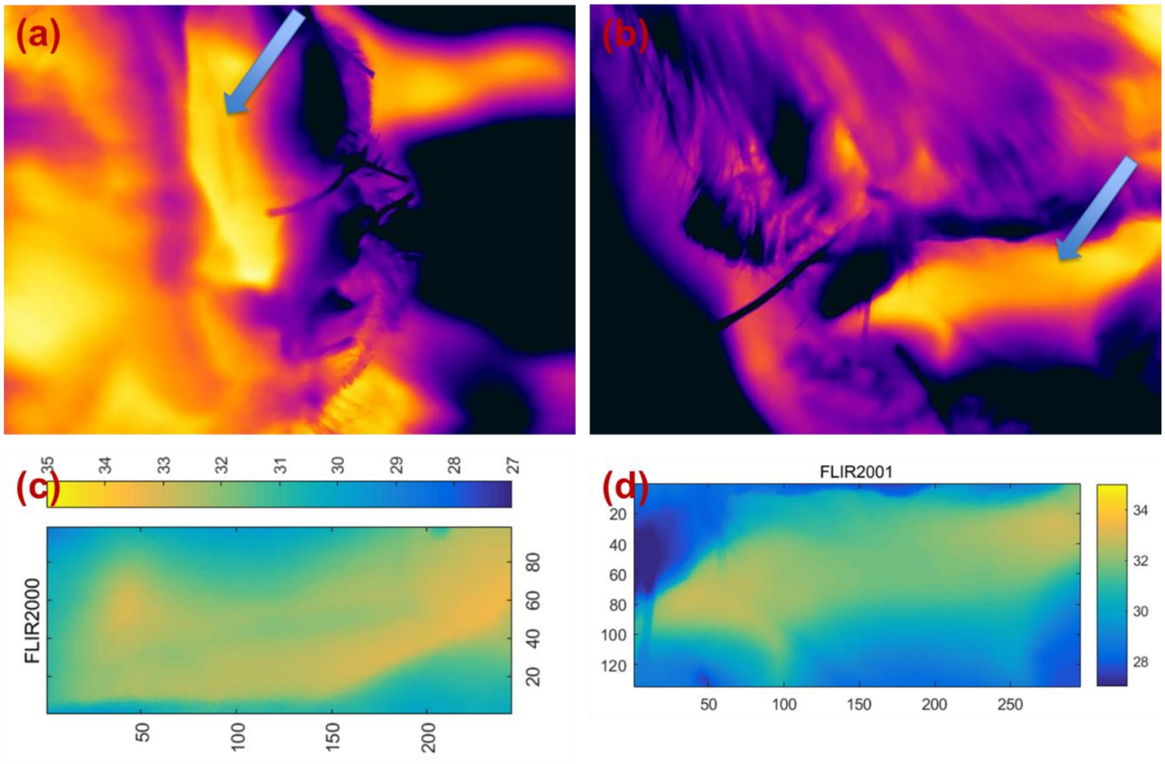

Figure 4. 2. (a) Thermal image of the rat's right leg nerve after surgery, blue arrow. The blue arrow points out the location of the nerve. (b) Thermal image of the contralateral side of (a) after surgery. The blue arrow points to nerve. (c) is the temperature map with color bar of (a), (d) is the temperature map of (b).

The appearance of the injured nerve under naked eye observation is the same as that of the contralateral nerve, but it is different under thermal imaging. This means that thermal imaging has the potential to detect nerve damage.

However, the detection effectiveness of thermal imaging and other specific details remain to be explored. We still don't know what degree of damage will cause significant changes in thermal imaging signals, and we still need more animal experiments to explore this view.

Stroke model simulation

Brain blood flow is blocked in stroke patients, that may change their facial temperature. Based on that assumption, we tested healthy human for simulation, and mouse stroke model.

In the simulation experiment (Figure 4. 3), a healthy subject placed ice pack and hot water bottle on his neck, near carotid artery, to model the stroke case. The experiment tested if the temperature change in local blood would be reflected in the facial temperature. Four groups of symmetrical ROIs were selected, the positions were forehead, eyes, upper cheek, and lower cheek. Temperature changes of each group on left and right side is compared. Subfigure (a) shows an example of a subject with the cold and hot bags, the blue and green dots are ROIs on upper cheek, their average temperature changes are shown in (b).

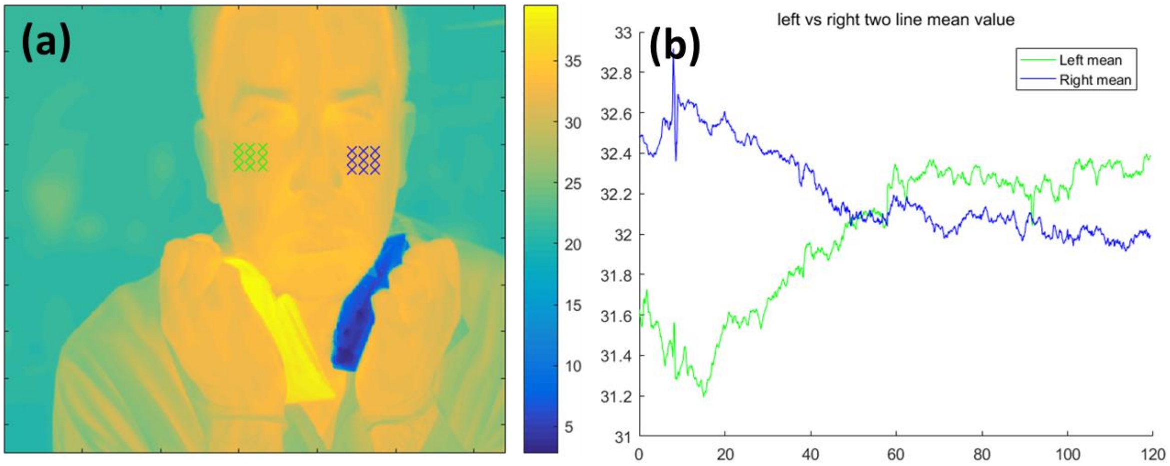

Figure 4. 3. A test that simulates a stroke in healthy subjects. (a) A subject put ice and hot bag on neck. Blue dots and green dots are the ROIs on the right and left (right and left of camera view). The average temperatures change of them during experiment are shown in (b).

The figure shows that when the blood flow temperature is affected, its upward or downward trend will be reflected in the facial temperature. Therefore, if blood flow to the brain is blocked, its temperature response should be stronger. Based on this, we tested a mouse stroke model.

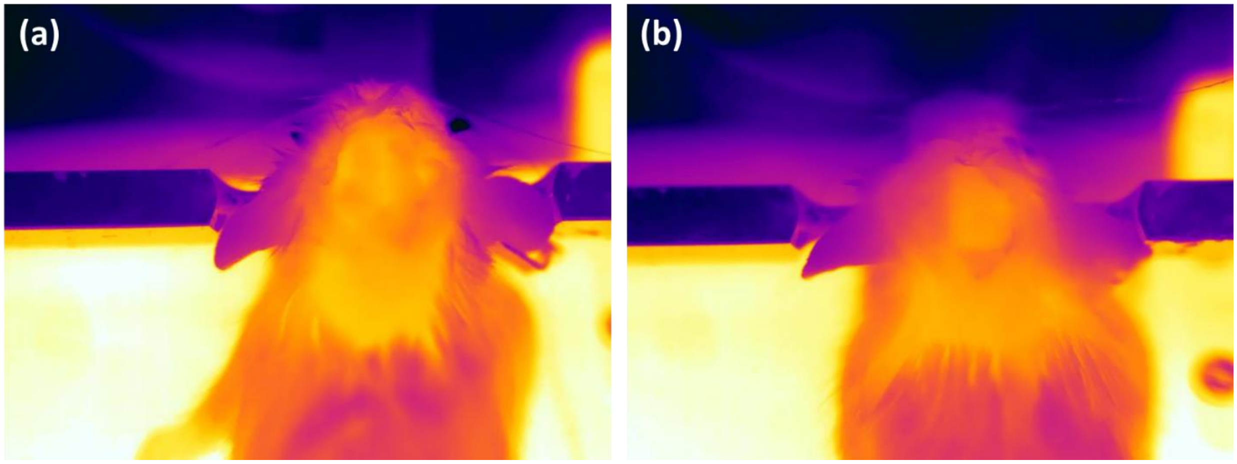

Figure 4. 4. Mouse stroke model test results. (a) Mouse thermal image before stroke. (b) Mouse thermal image after stroke for 5 minutes.

In the test of the mouse stroke model, the average temperature in brain area after stroke has dropped. But it is hard to distinguish the small structures from temperature change due to the resolution of thermal camera. There may be a link between a stroke and a drop in temperature, but it needs more experiment to be proved.

4.3 Thermal imaging tests in COVID-19 related research

4.3.1 Background

In 2020, the world experienced the COVID-19 pandemic, and there is still no sign of its end. The gold standard for identifying people infected with COVID-19 is swab and kit testing. However, the swab needs to go deep into the nasal cavity, which is inconvenient to operate and will cause discomfort to the subject. The test results of the kit are accurate, but they are consumables, the speed is slow, and sometimes there is a shortage of materials, so most institutions and regions do not use it as a daily inspection process.

As COVID-19 infected people often have fever symptoms, thermal imaging has become a common testing device in public places. The infrared camera can read the temperature data of the subject without contacting with him. When the temperature exceeds the threshold, it will alarm.

The following work is mainly on collecting data from healthy people, and test the application possibilities of infrared cameras in temperature collection.

4.3.2 Methods and tests

The subjects (n=8) were asked to take thermal images including wearing a mask, not wearing a mask, remain steady state and moving their head.

When the infrared camera captures images from subjects, most of the time they are walking into a room or passing by a public place. Their heads are moving during collection. To solve this problem, different motion correction methods are applied to thermal images.

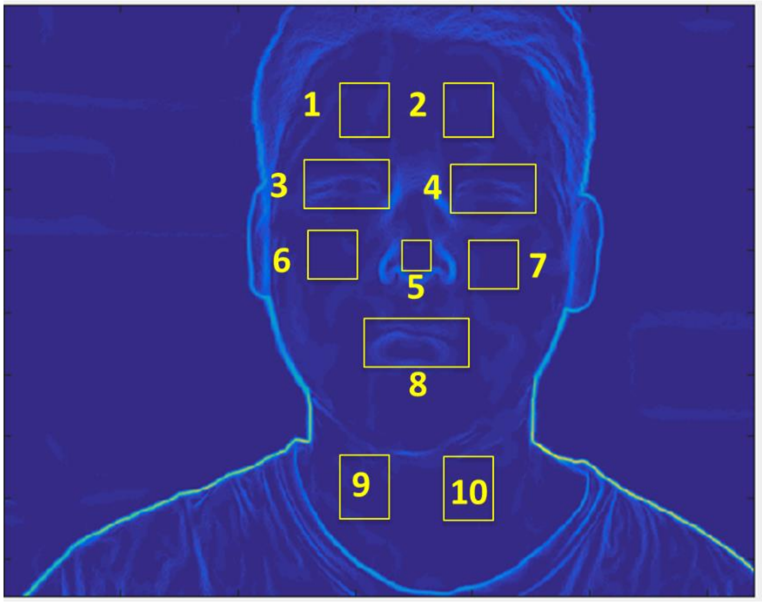

Figure 4. 5 An example of the subject's facial ROI area collection during experiment.

The subject first took off the masks and glasses, and after being still in front of the camera for 2 minutes, a 10-second video was taken in the initial state. Then they will test different postures: raise their heads, lower their heads, and turn their heads at a small angle to the left and right. Each stage lasts for 10 seconds, and returns to the initial state after the end.

10 different ROIs are manually selected for each subject, including the left and right side of subjects' head, face, eyes, neck, the subject's nose and mouth, as shown in Figure 4. 5. Each collected ROI area is numbered in the order of middle-left-right as shown in figure. For different subjects, ROIs with same number have the same size. The average temperature and temperature change of each ROI are recorded.

4.3.3 Results and discussion

The first analysis is to determine which area tends to have the most stable temperature and the least interference from small head movements.

Due to the large individual differences between subjects, and the number of subjects is not enough to smooth out individual differences, we used a scoring method.

The average temperature change of all ROI regions during movement of each subject will be ranked from small to large. For each subject, the ROI with the smallest difference gets 10 points, the second smallest get 9, and so on. When the average temperature difference is below 0.1 ℃, the temperature was considered the same. The part with the highest score will be recorded as the part with the most stable temperature. Average scores of the ten ROIs are shown in Table 4. 1.

Table 4. 1: The average score of the face temperature ROIs

ROI	1	2	3	4	5
1	4.0	4.5	3.2	5.0	2.0

ROI	**6**	**7**	**8**	**9**	**10**
6	4.6	3.0	4.2	5.8	4.0

Experimental results show that the most stable part is the right side of the neck, and the most unstable part is the tip of the nose. One of the possible reasons is the motion effect. Though the subjects were asked to move as required, and motion correction methods were applied to the results, the effects of movement still cannot be completely eliminated.

The second analysis is about comparing the temperature of different side.

In most thermal imaging studies, we usually assume that the temperature on left and right side are the same, unless there are special circumstances, for example, there are organs such as liver in the location to be collected. But there may be a slight difference in temperature on the left and right sides. We tested to study which group of opposite regions has the most stable temperature. We used the same dataset and ROI as the previous test. In order to exclude motion effect, we only analyzed the data in the steady state. Comparison results are shown in Figure 4. 6.

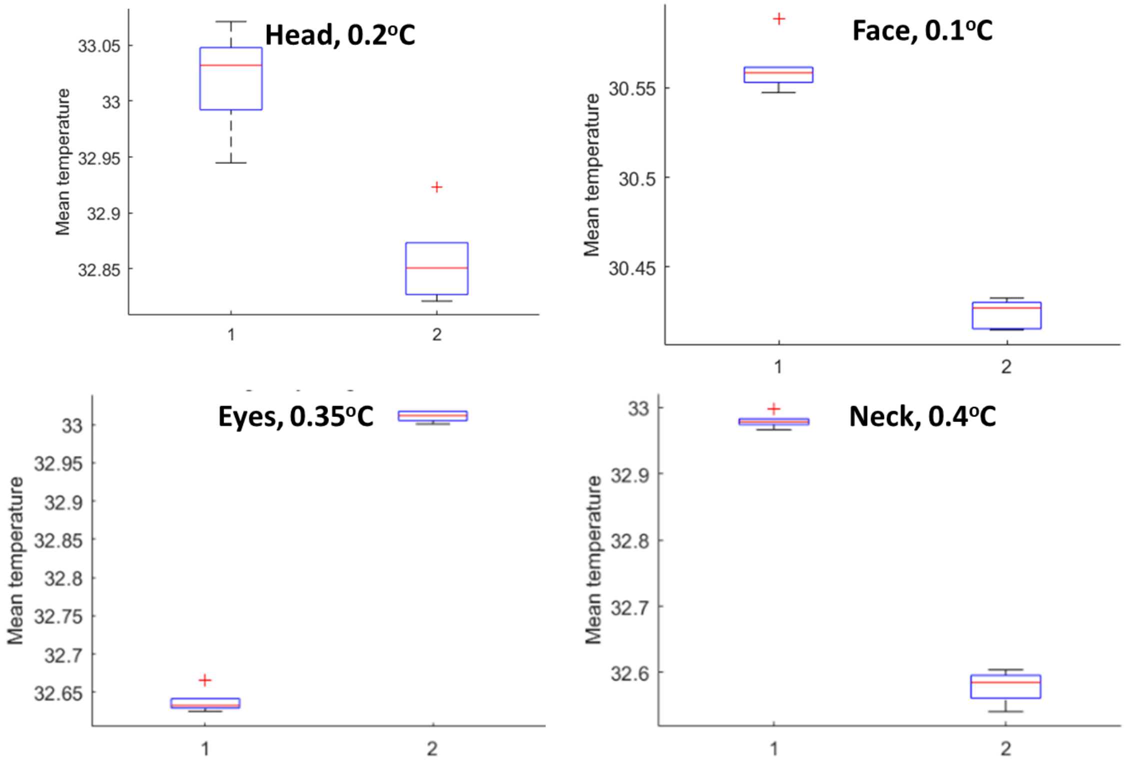

Figure 4. 6. Comparison of the average temperature of the ROI area on left and right sides of subjects. 1~left, 2~right. The title of the subgraph is the ROI location, and the difference between thei average values.

The figure compares the difference between the left and right ROI average temperature of each group of subjects. In the experiment, the difference in face temperature between left and right is the smallest.

In order to find the area with the closest temperature between different subjects, we also calculated the temperature distribution of each ROI area. The standard deviation of the ROI area of the right eye is the smallest, then left eye, the ROI of left neck part (number 10) ranks the third.

In this part of the research, we have found that when using a thermal camera to collect human temperature facial images, some subtle differences should be noted. The movement of the head will affect the data collection. In this case, the temperature of the cheeks, one side of the eyes, and the neck are relatively stable. When we compare the temperature of left and right side at steady state, the temperature between the eyes of different subjects is the smallest. This may because the mucosal temperature is closer to the body temperature, and the eye temperature is not as easily affected by air flow as the skin surface temperature. However, the temperature of the left and right eyes has larger difference compared to skin surface such as forehead and face, the reason for this phenomenon is not clear. Considering that the experiment was done during the epidemic and the number of subjects was limited, we need to collect more samples to study this phenomenon.

4.4 Software for thermal image capture and processing

Background

In the process of establishing the FDTI system, we wrote an interface suitable for controlling the T650SC thermal camera and the laser. In the work of optimizing the FDTI system, we hope that users can observe the performance of some features in real time, and then quickly determine the state of the current point. In the subsequent work of applying the thermal imaging system to human for data collection and analysis, we built another interface based on demand. At the same time, in the optimization of the hardware system, we also need to provide control of other hardware, such as step motor, and possible new thermal cameras.

We hope to develop a system that meets various requirements. The system can control the thermal and color camera, display some data and features such as FWHM in real time, and can use the graphical interface (GUI) to read the saved data for analysis and display.

Following example in Figure 4. 7 shows a part of the GUI that has been established, it is used for data visualization and analysis. Data is displayed in interaction area, and the user can do some intuitive tests without writing code, such as segmenting suspicious areas. The irregular area circled by white line in the thermal image gives an example of image segmentation. It uses region growing algorithm and is controlled by threshold. Users can export the current data to other formats for software analysis, or do batch processing. Some features such as FDTI's hot spot temperature rise curve can be displayed in the lower half of the GUI.

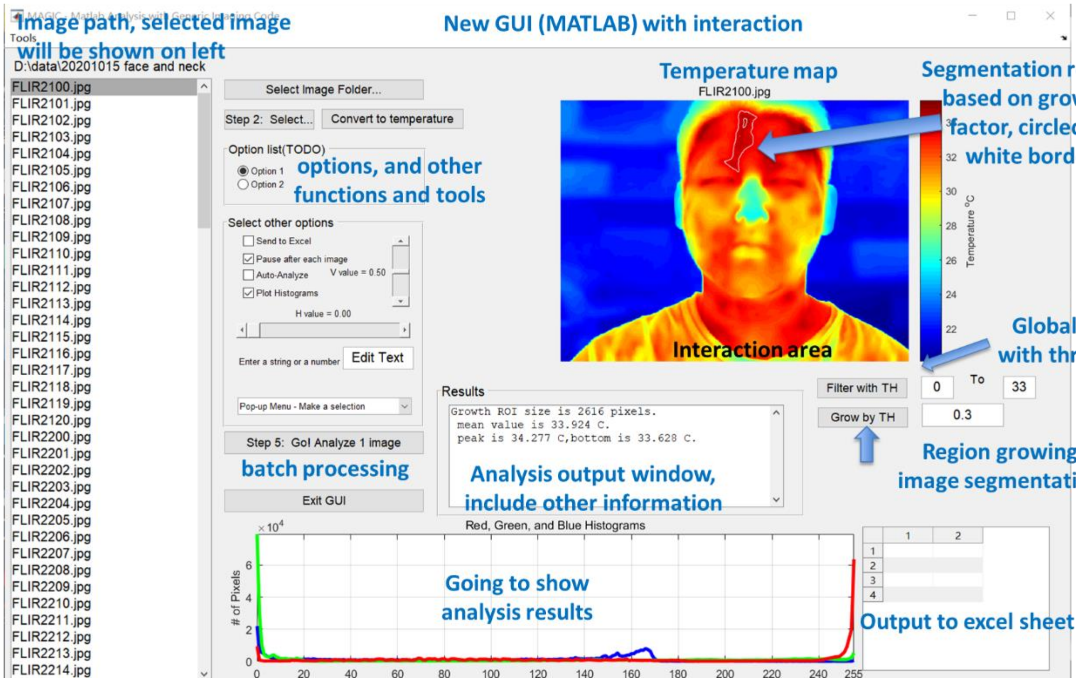

```
Growth ROI size is 2616 pixels.
 mean value is 33.924 C.
 peak is 34.277 C,bottom is 33.628 C.
```

Figure 4. 7. Data processing interface of the new GUI, an example.

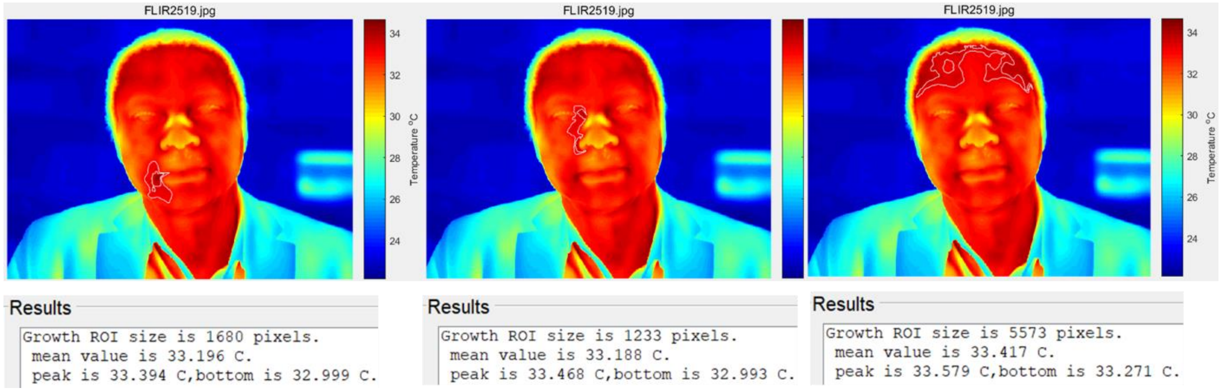

```
Growth ROI size is 1680 pixels.
 mean value is 33.196 C.
 peak is 33.394 C,bottom is 32.999 C.
```

```
Growth ROI size is 1233 pixels.
 mean value is 33.188 C.
 peak is 33.468 C,bottom is 32.993 C.
```

```
Growth ROI size is 5573 pixels.
 mean value is 33.417 C.
 peak is 33.579 C,bottom is 33.271 C.
```

Figure 4. 8. A simulation of non-researcher using the system.

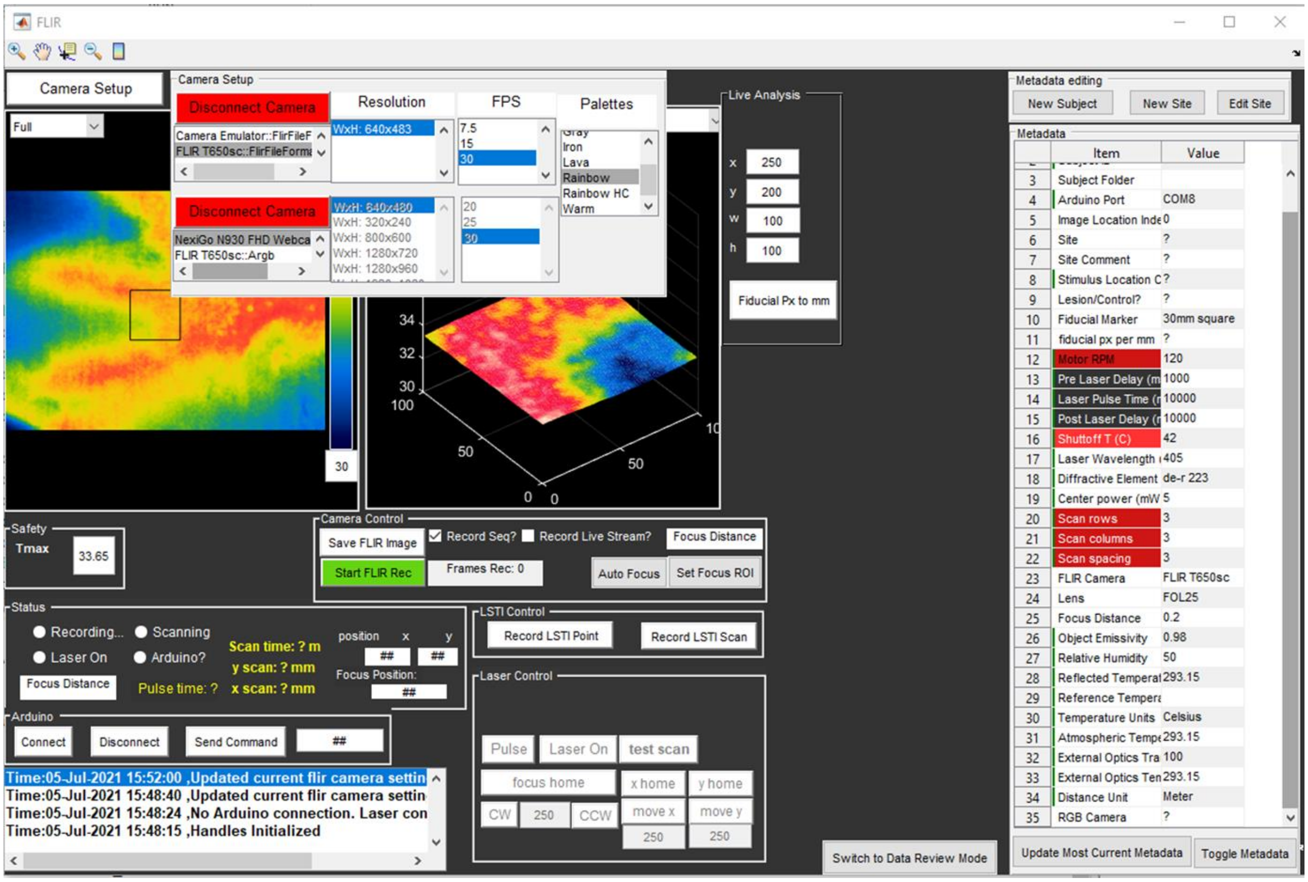

Tmax 33.65

x 250

y 200

w 100

h 100

	Item	Value
3	Subject Folder	
4	Arduino Port	COM8
5	Image Location Inde	0
6	Site	?
7	Site Comment	?
8	Stimulus Location C	?
9	Lesion/Control?	?
10	Fiducial Marker	30mm square
11	fiducial px per mm	?
12	Motor RPM	120
13	Pre Laser Delay (m	1000
14	Laser Pulse Time (r	10000
15	Post Laser Delay (r	10000
16	Shuttoff T (C)	42
17	Laser Wavelength (	405
18	Diffractive Element	de-r 223
19	Center power (mW	5
20	Scan rows	3
21	Scan columns	3
22	Scan spacing	3
23	FLIR Camera	FLIR T650sc
24	Lens	FOL25
25	Focus Distance	0.2
26	Object Emissivity	0.98
27	Relative Humidity	50
28	Reflected Temperat	293.15
29	Reference Tempera	
30	Temperature Units	Celsius
31	Atmospheric Tempe	293.15
32	External Optics Tra	100
33	External Optics Ten	293.15
34	Distance Unit	Meter
35	RGB Camera	?

```
Time:05-Jul-2021 15:52:00 ,Updated current flir camera settin
Time:05-Jul-2021 15:48:40 ,Updated current flir camera settin
Time:05-Jul-2021 15:48:24 ,No Arduino connection. Laser con
Time:05-Jul-2021 15:48:15 ,Handles Initialized
```

Figure 4. 9 Planning to be the main interface of the GUI, built by Leo Shmuylovich.

A new GUI and interaction data processing system will facilitate the work in the laboratory. Besides, it helps non-researchers to understand and effectively use this imaging system. A simulation of this scene is shown in Figure 4. 8. The user operates the GUI, reads his own thermal imaging map in real time, then operates it to segment the suspicious area. The size and average temperature of the area will be displayed. It will be a part of the main interface shown in Figure 4. 9.

At present, the GUI has only been tested by laboratory members. As part of the laboratory work, we are familiar with the data processing pipeline. But in terms of designing a convenient and easy-to-use GUI for other users, we need feedback from users in other areas to update the GUI.

We still have some future work to do.

References

1. Haroche, A., et al., *Brain imaging in catatonia: systematic review and directions for future research.* Psychological Medicine, 2020. **50**(10): p. 1585-1597.
2. Najt, P., H.L. Richards, and D.G. Fortune, *Brain imaging in patients with COVID-19: A systematic review.* Brain, Behavior, & Immunity - Health, 2021. **16**: p. 100290.
3. McCrory, E.J., M.I. Gerin, and E. Viding, *Annual research review: childhood maltreatment, latent vulnerability and the shift to preventative psychiatry–the contribution of functional brain imaging.* Journal of child psychology and psychiatry, 2017. **58**(4): p. 338-357.
4. Peters, L. and B. De Smedt, *Arithmetic in the developing brain: A review of brain imaging studies.* Developmental Cognitive Neuroscience, 2018. **30**: p. 265-279.
5. Wang, H., et al., *Brain temperature and its fundamental properties: a review for clinical neuroscientists.* Frontiers in Neuroscience, 2014. **8**: p. 307.
6. Metwali, H. and A. Samii, *Seed-Based Connectivity Analysis of Resting-State fMRI in Patients with Brain Tumors: A Feasibility Study.* World Neurosurgery, 2019. **128**: p. e165-e176.
7. Voss, H.U., et al., *A vascular-task response dependency and its application in functional imaging of brain tumors.* Journal of Neuroscience Methods, 2019. **322**: p. 10-22.
8. Yahyavi-Firouz-Abadi, N., et al., *Presurgical Brain Mapping of the Ventral Somatomotor Network in Patients with Brain Tumors Using Resting-State fMRI.* American Journal of Neuroradiology, 2017. **38**(5): p. 1006.
9. Fullana, M.A., et al., *Fear extinction in the human brain: A meta-analysis of fMRI studies in healthy participants.* Neuroscience & Biobehavioral Reviews, 2018. **88**: p. 16-25.
10. Frangos, E. and B.R. Komisaruk, *Access to Vagal Projections via Cutaneous Electrical Stimulation of the Neck: fMRI Evidence in Healthy Humans.* Brain Stimulation, 2017. **10**(1): p. 19-27.
11. Schmid, J., et al., *Placebo analgesia in patients with functional and organic abdominal pain: a fMRI study in IBS, UC and healthy volunteers.* Gut, 2015. **64**(3): p. 418.
12. Salehi, A., et al., *Therapeutic enhancement of blood–brain and blood–tumor barriers permeability by laser interstitial thermal therapy.* Neuro-Oncology Advances, 2020. **2**(1).

Chapter 5 Cancer viewing goggle system optimization

5.1 Abstract

This part describes my work on the cancer viewing goggle system, includes system description, signal enhancement, and work on registration. The collaborators in this section include Suman Mondal, Christine O’Brien, Leo Shmuylovich, Siddharth Kurkure, . Alexander Seidel, and Hanru Zhang. I wrote the chapter, conducted some experiments with collaborators, designed some experiments, analyzed the data from goggles, and worked in collaboration on the code.

5.2 Introduction

Medical imaging tools have been widely used in the fields of tumor diagnosis, treatment planning and postoperative detection. During surgery, medical images are used to track the location and size of the tumor. At the same time, after the operation, it is necessary to check the effect of the operation and whether the tumor tissue has been successfully removed. This prompted the development of image-guided tumor surgery. The ideal imaging method are expected to have high sensitivity, specificity, and can detect tumor status in real time during surgery. In addition, if it displays information in a way that surgeons can easily understand and provide feedback, it will help the clinical promotion of this method.

In the field of intraoperative image-guided surgery, fluorescence imaging uses non-ionizing radiation, the imaging device is relatively simple, and can read and detect microscopic lesions in real time. This makes fluorescence imaging widely used in surgical guidance. Near-infrared (NIR) fluorescence imaging in 700-900nm range has been applied to intraoperative imaging. In this wavelength range, the absorption rate of photoactive biomolecules in the tissue is low, that reduces tissue auto fluorescence. Researchers have developed tumor-targeting NIR contrast agents, including peptides and Nano-particle based agents. NIR Fluorescence Image Guided Surgery (NIR-FIGS) systems have also been developed and used for intraoperative tumor imaging.

In these systems, the head-mounted display (HMD) has unique advantages. Its field of view can be matched with the surgeon, and it does not require the support of other staff and bulky hardware. We have developed a head-mounted NIR imaging system “cancer vision goggles” and carried out several technical iterations [1]. The system can perform lymph node check and tumor edge assessment of tumors without interrupting the operating room process [1, 2]. According to the feedback of clinical data collection and data processing, some parts of the system need to be improved. The strong background noise leads to low signal-to-noise (SNR) ratio of collected data. The camera and the user's eyes need to be registered so that the error of the fluorescent superimposed on the target is smaller. The following chapters have made improvements on system optimization and expansion.

5.3 Methods

The experimental platform is DK-52 HMD system (Lumus, Ness Ziona, Israel). The NIR light source, camera in the system, and hardware setting were the same as the previous setting in [2] and appendix.

The data processed in the experiment includes animal data and human data. All animal work was approved and performed under an approved protocol by Washington University’s Institutional Animal Care and Use Committee (IACUC). The human procedures were carried out in accordance with the approved guidelines by the Institutional Review Board of Washington University. Informed consent was obtained from all patients for this United States Health Insurance Portability and Accountability Act compliant study.

In the process of collecting data, NIR contrasts agents Indocyanine green (ICG, Sigma-Aldrich, St. Louis, MO) and LS301 (a tumor-targeted NIR contrast agent developed in our lab, details in [3] and appendix) were used. Clinical grade ICG for human SLNM was provided by the Siteman Cancer Center (Washington University in St. Louis, MO).

5.4 Results and Disscussion

5.4.1 Signal enhancement

The original image captured by the camera is dark. The fluorescence signal is superimposed on the color image in the form of grayscale, and the signal intensity is weak. Therefore, it is difficult to distinguish the fluorescent signal from the background (Figure 5. 1 (a)). This is caused by the uneven distribution of the gray value of the collected image (Figure 5. 1 (b)).

In order to solve this problem, we analyzed the gray value of the image. The grayscale of the image was almost all below 50. Since the NIR signal in the figure was not a quantitative signal that can be converted to fluorescent agent concentration, changing the grayscale of the NIR signal would not affect the result.

Then, the image was first divided into sub-image blocks, the grayscale value range for each sub-image was adjusted. Then, sub-images were combined to a whole grayscale image. Finally, the overall grayscale of the whole image was adjusted by a linear projection. Also, the weight of NIR channel was increased to 0.7 to generate a brighter superimposed image (Figure 5. 1 (c) (d)). Images were shown in false colors to highlight the contrast of the fluorescent signal, and it is convenient for users to identify.

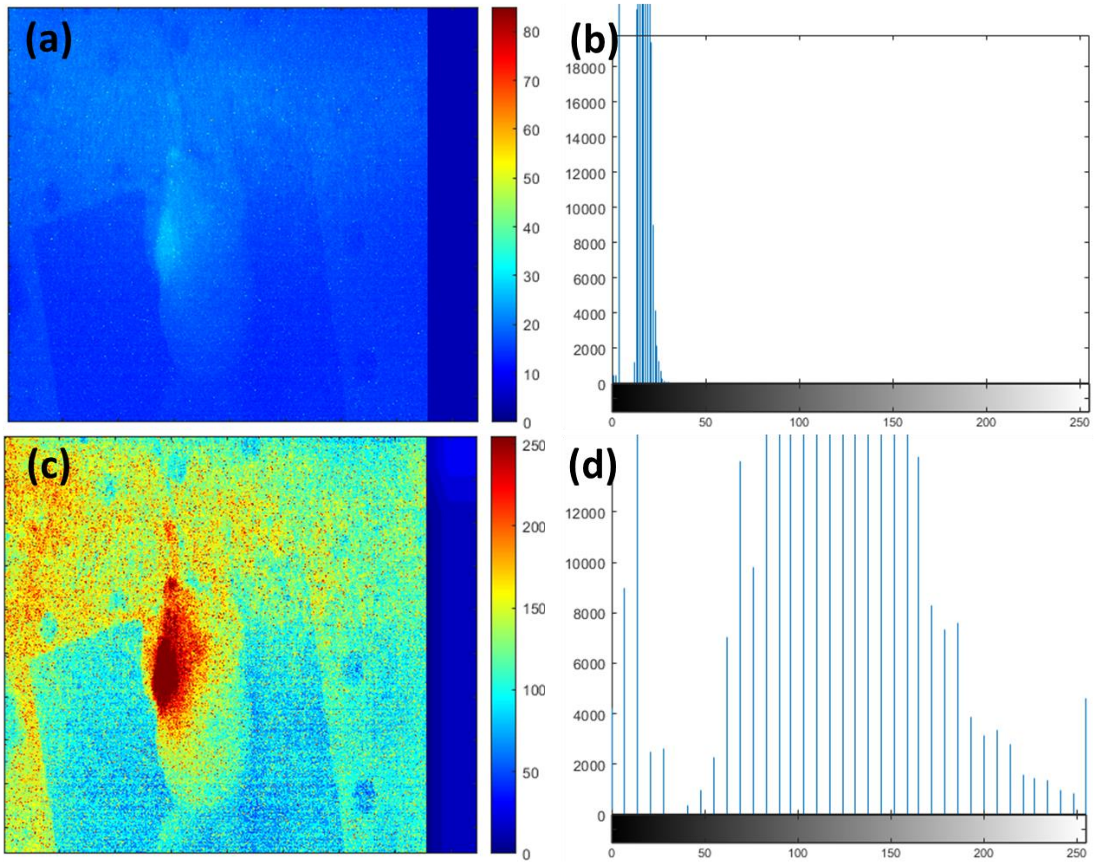

Figure 5. 1 Examples of signal enhancement. (a) Original image, mice with LS301 contrast agent under 780nm laser stimulation. (b) Original image grayscale value distribution. (c) is (a) after NIR signal enhancement and grayscale adjustment, (d) is the grayscale value distribution of (c)

After enhancing the signal, we observed obvious noise on the enhanced figure. That was because we indiscriminately enhanced the noisy NIR signal. In order to reduce the influence of noise and improve the signal-to-noise ratio, we analyzed the noise to select suitable filter for target.

First, we build a model that simulates noise. Set ideal image as I_0. When there is no laser, the image captured by camera is $I_c = (I_0 + n_b + n_c)n_{m1}$, here n_b is background noise, n_c is camera noise, n_{m1} is the multiplicative noise that exists in this state. When there is laser stimulation, the image capture by camera is $I_l = (I_0 + n_b + n_c + I_{NIR} + n_l)n_{m2}$, I_{NIR} is the NIR signal image generated by contrast agent, n_l is the noise related to laser stimulation, and n_{m2} is the multiplicative noise in stimulate state. To simplify the model, suppose $n_{m1} = n_{m2}$, then after subtracting the two images, the remaining part is $I_r = (I_{NIR} + n_l)n_{m1}$. Then filters can be applied to this part. Different filters were tested to reduce the influence of background noise, results were shown in Figure 5. 2.

The enhanced figure without filter is shown in Figure 5. 2 (a), signal is enhanced at the same time as the background noise. Average filter, median filter and wiener filter were used in subfigure (b)~(f). Signal noise and background noise have been suppressed.

In the experiment, we need to enhance the signal contrast of contrast agent on the surface of the isolated tumor, or the surgical area. At the same time, we need to suppress the background noise and reflections in the background. Therefore, we added a dynamic threshold for NIR channel in addition to the filter. According to experimental feedback, the threshold is set to 50% of the peak value of the NIR signal, signals below the threshold will be eliminated. The signal enhancement with threshold is shown in Figure 5. 2 (g)~(l).

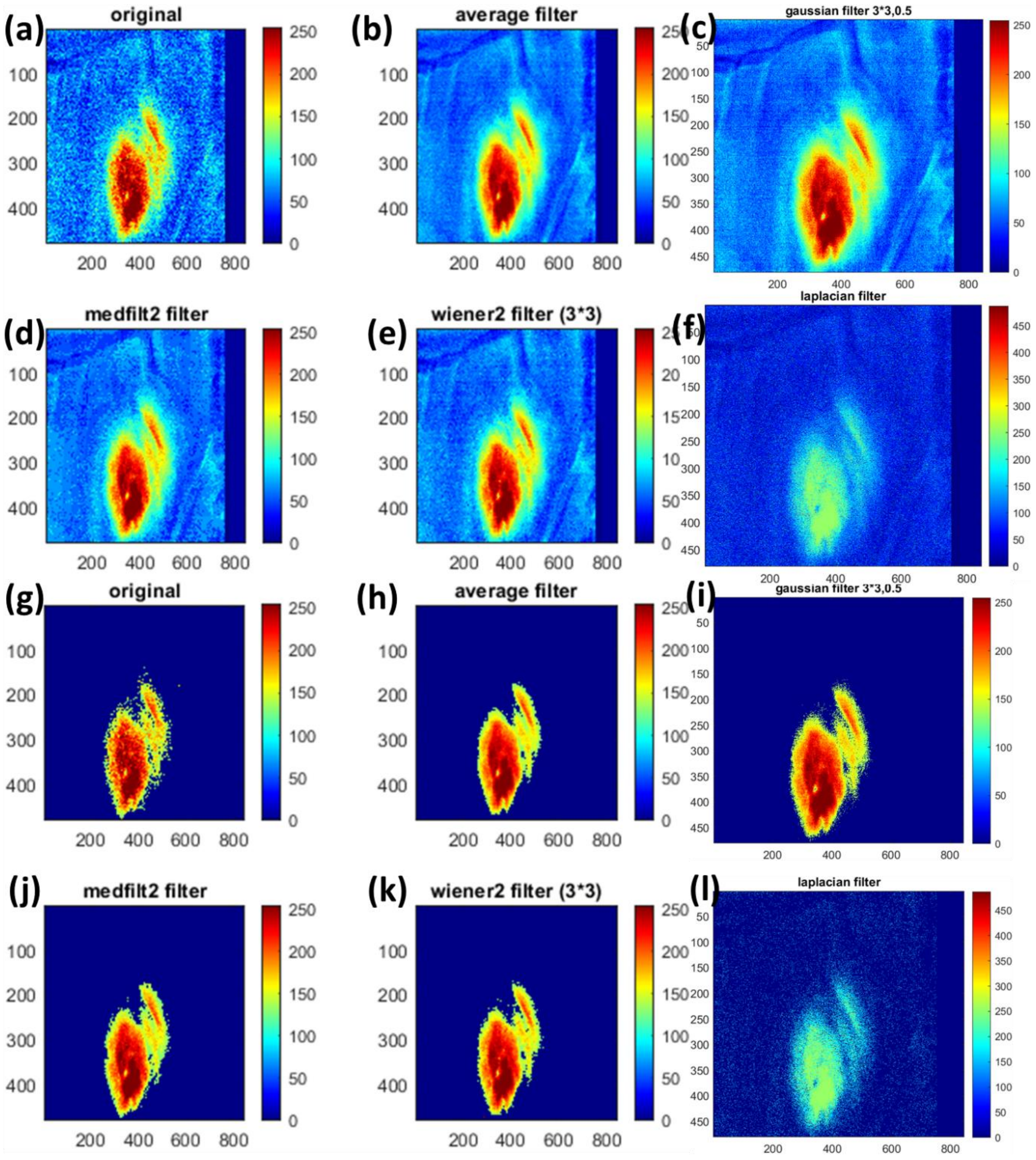

Figure 5. 2. The performance of filters on NIR image. (a) Original NIR image, no filter was added, enhanced by grayscale adjustment. (b) NIR image with average filter. (c) NIR image with Gaussian filter (3*3). (d) NIR image with median filter. (e) Wiener filter, (3*3). (f) Laplacian filter, overlapped on original image for edge enhancement. (g)~(l) are results related to (a)~(f) with auto threshold.

Since there is no clear image as the evaluation standard, the image quality evaluation used the naked eye score. The results of different filters were divided into different groups and given numbers. Group with and without threshold were scored separately. There were 5 images in each group, including images collected from mice, tumors and during surgery. The subjects made a blind evaluation of each group, with 5 points being the best and 1 being the worst.

In no threshold group, average filter and Gaussian filter performed the best (3.8 / 5.0), then the median filter (3.5 / 5.0). In threshold group, average filter and median filter performed the best (4.2/5.0), then the Gaussian filter (4.1/5.0). So, we selected the average filter as the default image processing and enhancement filter. The median and the Gaussian filters were alternatives that can be switched in the software.

Discussion

In the previous content, our work was on NIR image signal enhancement. The NIR signal is effectively enhanced by the way the user scores. However, during the image evaluation process, we observed that sometimes subjects would confuse the results of average filter, Gaussian filter and median filter. This means that when the images are similar in appearance, it is difficult for subjects to distinguish them by evaluation. In addition to the scoring system, quantitative indicators can also be used to evaluate images, and the results will be more discriminative.

When the reference image is unknown, there are some no-reference image quality assessments, such as BRISQUE method [4]. Those indicators help to achieve a better evaluation system.

In addition, in the experiment, we found that the original system has problems such as the dark field of the camera and the mixing of multi-wavelength fluorescent signals. Besides, the camera used in the experiment has a low sensitivity to fluorescence signals. These can be solved by updating the hardware, for example: new NIR camera, and new optical filter.

5.4.2 Image registration

For the registration of color and NIR images, we added offset and zoom in/out to the software. After tested with marker, the NIR image can be registered to color image with sub millimeters accuracy. An example is shown in Figure 5. 3. Subfigure (a) shows the color image of isolated tumor, the surface of the tumor is stained for biopsy, the marker next to tumor shows the direction of the tumor. Subfigure (b) is the registered superimpose image of color and NIR. NIR signal is shown in pseudo-color, the color indicates the signal strength. (c)(d) are color and registered images during surgery. The background noise and reflection NIR signal mentioned before are suppressed by average filter, and grayscales of NIR images are adjusted in both (b) and (d).

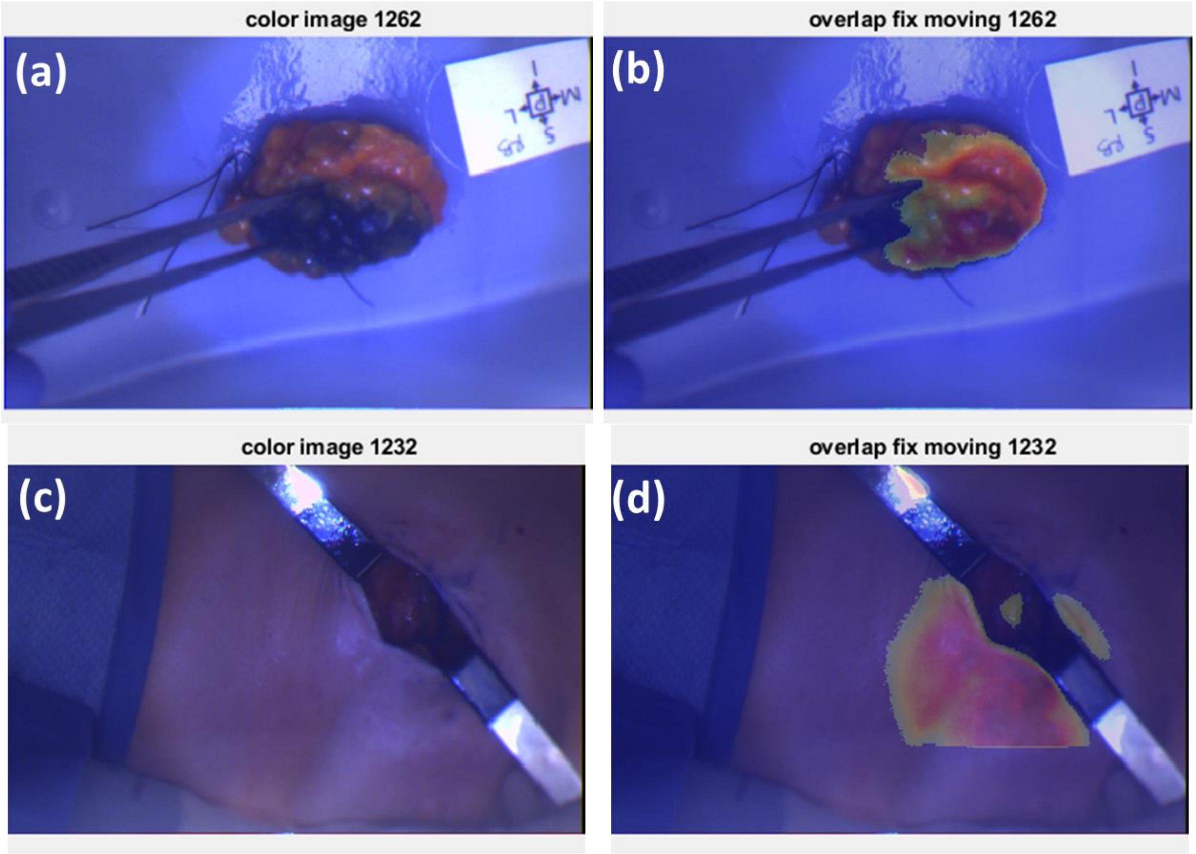

Figure 5. 3. Examples of color and NIR registration. (a) Color image of tumor. (b) Registered image of color and NIR of tumor. (c) Color image during surgery. (d) Registered image of color and NIR during surgery. The NIR signal on (b) and (d) had been enhanced and filtered.

For the registration of camera and the naked eye, we tried IR sensor, ultrasound sensor and depth camera to detect the distance of target, then applied rigid registration for the marker. An extra camera ("eye camera") was placed at the eye position behind goggle to simulate the naked eye. The photos it took were assumed to be the scene seen by the naked eye.

During the registration process, the first step was done by the subject. The target was put 50 cm away from the front side of the goggle. The subject clicked on the screen, and a white cross appeared in the color-NIR camera's view. The subject dragged the white cross to the position corresponding to the eye camera to simulate manual registration. After 4~6 white crosses were registered, the subject clicked a "finish" button, then a bounding box was generated in the view of the color-NIR camera. In the second step, system would generate several sets of registrations for the bounding box with pre-stored matrix templates. These templates were pre-calculated for matching eye camera and color-NIR camera at different distances (40/50/60 cm in experiment). In the pre-calculation step, 2D checker board was put at different distance from eye camera and color-NIR camera, and corner points matching was used for registering. The user would choose the best matching results from them.

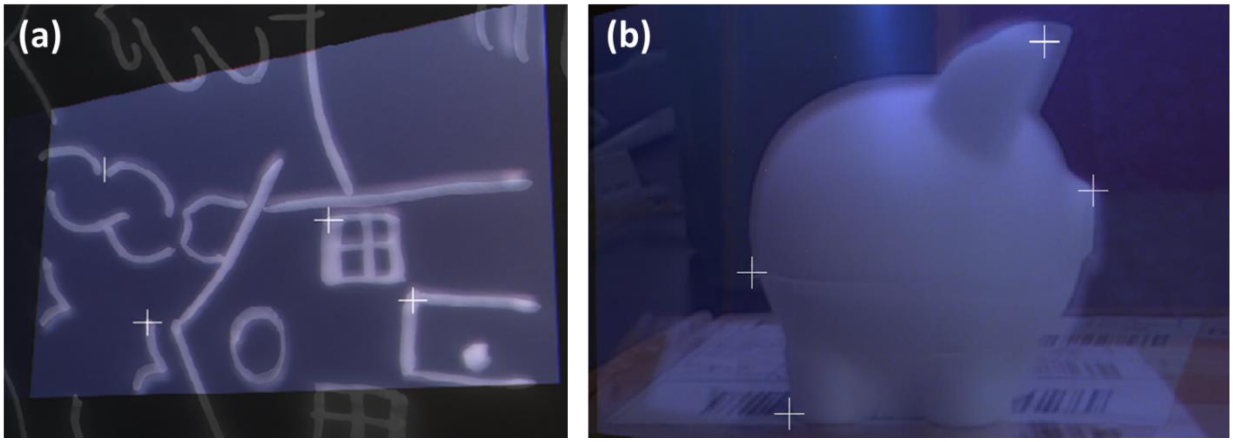

Figure 5. 4. Camera-eye registration results. (a) Registration result of 2D target. The white line is the simulated registration target. The position of the white cross is determined by the user, the bright part is the color-NIR camera view, and the dark background is the eye view (simulated by camera). (b) Registration result of 3D target. The white plastic object in the foreground is the registration target.

The registration results are shown in Figure 5. 4. Subfigure (a) shows the 2D target registration result. Subfigure (b) shows the 3D target registration result. The length and width of the lines in the 2D image were pre-recorded, and we selected the ROI to compare the matching deviation. 25 corner points and points from border detect were extracted from the ROI, and their average distance on the two images was converted into physical distance. The average error is 1.23 mm for 2D target, and 3.58 mm for 3D target.

Discussion

In the experiment, we used a camera to simulate the naked eye, and tested the registration of 2D and 3D targets. However, in the experiment, the camera was fixed on the platform, but in the clinical trial, the user's head was moving, which increased the difficulty of registration. Besides, the eyes of user were also moving.

Ideally, the registration system can accurately identify a special marker from the environment, and then register the system according to the world coordinate system provided by the marker, which is many surgical navigation systems do. But in clinical trials, it is difficult for us to place markers on patients. We tried to test the marker-free registration, which greatly increased the difficulty. Therefore, we need users to perform interactive registration, and used pre-calculated registration matrixes for next step registration. This increases the workload of the subjects. We can solve this problem by pre-storing the registration preferences of subjects. However, the distance change caused by the subject's head movement requires additional correction. The depth sensor we used in the experiment cannot return an accurate depth map in ROI.

In addition, the disadvantage of the camera simulating the human eye is that the subject's eyeballs will also move. Installing an eye tracking camera on the goggle system can solve this problem. However, the subject asked to install as few items as possible on the head. Because during the operation, surgeons need to wear headlights and goggles to block body fluids. The addition of the HMD system has been complained of “too many accessories on the head”. In order to solve this problem, we need to miniaturize and lighten the system, reduce the weight and size of accessories.

The result of registration quality is also difficult to measure. For 2D targets, we can use checkerboard and hand-drawn patterns. However, for 3D targets, the focus of the camera and the error caused by user operation will lead to different errors at different depths. This is because the 2D image generated by the camera needs to be deformed to be suitable for the 3D target. We still need to further explore other registration methods.

References

1. B. Mondal, S., et al., *Binocular Goggle Augmented Imaging and Navigation System provides real-time fluorescence image guidance for tumor resection and sentinel lymph node mapping.* Scientific Reports, 2015. **5**(1): p. 12117.
2. Mondal, S.B., et al., *Optical See-Through Cancer Vision Goggles Enable Direct Patient Visualization and Real-Time Fluorescence-Guided Oncologic Surgery.* Annals of Surgical Oncology, 2017. **24**(7): p. 1897-1903.
3. Shen, D., et al., *Selective imaging of solid tumours via the calcium-dependent high-affinity binding of a cyclic octapeptide to phosphorylated Annexin A2.* Nature Biomedical Engineering, 2020. **4**(3): p. 298-313.
4. Mittal, A., A.K. Moorthy, and A.C. Bovik, *No-reference image quality assessment in the spatial domain.* IEEE Transactions on image processing, 2012. **21**(12): p. 4695-4708.

Appendix